Modelling the optical and electronic transport properties of AlGaAs and AlGaN intersubband devices and optimisation of quantum cascade laser active regions

Andrew Grier

Submitted in accordance with the requirements for the degree of Doctor of Philosophy

The University of Leeds

School of Electronic and Electrical Engineering

August 2015

The candidate confirms that the work submitted is his own, except where work which has formed part of jointly authored publications has been included. The contribution of the candidate and the other authors to this work has been explicitly indicated below. The candidate confirms that appropriate credit has been given within the thesis where reference has been made to the work of others.

A variation of the description of density matrix methods in Chapter 4 of the thesis has been contributed to a textbook submitted to publishers as follows:
Quantum Wells, Wires and Dots
4th edition, Wiley and sons
P. Harrison and A. Valavanis
Candidate has contributed sections outlining the basic principles of density matrices and how they can be used to model THz QCLs. Section was written independently with proof-reading by P. Harrison and A. Valavanis at Sheffield Hallam University and University of Leeds respectively.

Two figures in Chapter 6 of the thesis have been adapted from versions appearing in publication as follows:
Efficient prediction of THz QCL dynamics from steady-state simulations
Applied Physics Letters, vol.106, 161105, 2015.
G. Agnew, A. Grier, T. Taimre, Y.L. Lim, A. Valavanis, J. D. Cooper, P. Dean, S.P. Khanna, M. Lachab, E. H. Linfield, A. G. Davies, P. Harrison, Z. Ikonić, D. Indjin, and A.D. Rakić
Paper led by collaborator at University of Queensland, Australia. Candidate contributed QCL parameters calculated by a full rate equation model developed at Leeds along with A. Valavanis, J. D. Cooper, and L. Lever. Paper was written by G. Agnew however the candidate made significant contributions to the creation of the figures used.

Theoretical results in Chapter 7 of the thesis has appeared in publication as follows:
Comparative study of intersubband absorption in AlGaN/GaN and AlInN/GaN superlattices: Impact of material inhomogeneities
Physical Review B, vol. 88, 23530, pp.1-10. 2013.
C. Edmunds, L. Tang, M. Cervantes, M. Shirazi, J. Shao, A. Grier, A. Valavanis, J. D. Cooper, D. Li, G. Gardner, D.N. Zakharov, Z. Ikonić, D. Indjin, P. Harrison, M.J. Manfra, and O. Malis

Paper led by experimental collaborators at Purdue University, USA. Candidate contributed theoretical modelling and quantification of the contribution of each scattering mechanism with code developed in collaboration with other members of the research group at the University of Leeds.

Theoretical calculations reviewed in Chapter 7 of the thesis has appeared in a conference paper as follows:

A scattering rate approach to the understanding of absorption line broadening in near-infrared AlGaN/GaN quantum wells

A. Grier, J. D. Cooper, L. Lever, A. Valavanis, Z. Ikonić, D. Indjin, P. Harrison, C. Edmunds, J. Shao, L. Tang, G. Gardner, D. Zakharov, M. J. Manfra, and O. Malis

6th Space Agency - MOD Workshop on Wide Bandgap Semiconductors and Components, ESA-ESTEC, Noordwijk, Netherlands, 8–9 October 2012.

Conference paper written by candidate with results obtained using code developed along with colleagues at the University of Leeds. Paper presents nearly all of the calculations (relating to broadening, absorption and many-body effects) used in Chapter 7 along with initial results which formed the basis of the Physical Review B publication above. This conference paper also included comparison to experimental results which were carried out by collaborators at Purdue University, USA.

Acknowledgements

I would like to express my gratitude to my colleagues, friends and family who have supported me throughout the course of this work. Firstly, I thank my supervisors Paul Harrison, Zoran Ikonić and Dragan Indjin who have always been incredibly enthusiastic, supportive and knowledgeable of semiconductor physics. I would also like to thank the Engineering and Physical Sciences Research Council (EPSRC) for the support of a doctoral training grant award.

I am grateful to the students and staff of the quantum electronics group who I have enjoyed sharing an office with over the years: Jonathan Cooper, Andrew Sills, Helen Rafferty, Leon Lever, Osamah Aldaghri, Pavlo Ivanov and Nikola Pradanović. Special thanks are also due to Alex Valavanis who has mentored me and contributed many ideas in interesting discussions over the years. Additionally, a significant proportion of the present work was completed using scattering rate code developed over the years at Leeds which Alex, Jonathan, Pavlo and I have worked together to update.

I would also like to thank many excellent collaborators: Colin Edmunds and Oana Malis at Purdue University, Gary Agnew, Thomas Taimre and Aleks Rakić at the University of Queensland, and David Winge at the University of Lund. It has been a privilege to work together and visit each of these groups during my research.

On a personal note I would like to thank my parents for their love and support, without which I would not have made it this far. Special thanks are also due to

my sister, extended family, and all of my friends who have been understanding, supportive and such good company over the years.

Andrew Grier, August 2015

Abstract

Terahertz quantum cascade lasers (THz QCLs) have many potential applications such as medical and security screening. While their output power has recently exceeded 1 W, their highest operating temperature is currently limited to ≈ 200 K due to mechanisms such as thermal backfilling and non-radiative phonon emission between lasing states. To achieve higher operating temperatures, theoretical models are key to suppressing these degradation mechanisms either through further design optimisation or new material systems.

This work investigates the opto-electronic properties of state-of-the-art inter-subband devices in $Al_xGa_{1-x}As$/GaAs and $Al_xGa_{1-x}N$/GaN material systems as well as the applications of QCLs. A density matrix model is investigated and used to predict the electron distribution, gain and current density in an arbitrary QCL active region. This model is validated with a comparison to rate equation, non-equilibrium Green's function, and experimental data for $Al_xGa_{1-x}As$/GaAs QCLs. Novel designs using tall AlAs barriers to suppress leakage current are modelled, and the effect of long and short range interface roughness is investigated. An increased sensitivity to roughness is shown for tall barrier structures which have a larger conduction band offset discontinuity and thinner epitaxial layers. The model is then used to optimise both AlGaAs and AlGaN QCL structures to propose new designs for a desired emission wavelength.

The use of the density matrix approach to model possible applications is demon-

strated by modelling the origin of the self-mixing (optical feedback) interferometry terminal voltage variations. It is shown that the self-mixing voltage amplitude is highly dependent on the differential resistance of the QCL, and the increased sensitivity of a particular QCL is explained.

The feasibility of nitride QCLs is shown by comparing the calculated and experimental absorption linewidth of near-infrared and THz $Al_xGa_{1-x}N/GaN$ quantum wells grown by molecular beam epitaxy. Finally, a novel adaptation of the density matrix approach is used to investigate the transport properties of nitride resonant tunnelling diodes alongside sequential tunnelling devices. This allows the extent of transport due to bound defect states and interface roughness values to be estimated.

List of publications

The following journal and conference papers were contributed to by the author during the course of the present work. The asterisk (*) denotes first-authorship.

Journal papers

- * **A. Grier**, A. Valavanis, D. Li, L. Tang, C. Edmunds, J. Shao, J. D. Cooper, G. Gardner, M. J. Manfra, O. Malis, D. Indjin, Z. Ikonić, and P. Harrison *Modelling coherent vertical electron transport and interface roughness effects in AlGaN/GaN intersubband devices with an extended density matrix formalism* Accepted by Journal of Applied Physics.

- G. Agnew, **A. Grier**, T. Taimre, Y.L. Lim, A. Valavanis, J. D. Cooper, P. Dean, S.P. Khanna, M. Lachab, E. H. Linfield, A. G. Davies, P. Harrison, Z. Ikonić, D. Indjin, and A.D. Rakić *Efficient prediction of THz QCL dynamics from steady-state simulations* Applied Physics Letters, vol.106, 161105, 2015.

- C. Edmunds, L. Tang, M. Cervantes, M. Shirazi, J. Shao, **A. Grier**, A. Valavanis, J. D. Cooper, D. Li, G. Gardner, D.N. Zakharov, Z. Ikonić, D. Indjin, P. Harrison, M.J. Manfra, and O. Malis *Comparative study of intersubband absorption in AlGaN/GaN and AlInN/GaN superlattices: Impact of material inhomogeneities* Physical Review B, vol. 88, pp.1–10. 2013.

- A. Scheuring, P. Dean, A. Valavanis, A. Stockhausen, P. Thomas, M. Salih, S.P. Khanna, S. Chowdhury, J. D. Cooper, **A. Grier**, S. Wuensch, K. Ilin, E. H. Linfield, A. G. Davies, and M. Siegel *Transient Analysis of THz-QCL Pulses Using NbN and YBCO Superconducting Detectors* IEEE Transactions on Terahertz Science and Technology, vol. 3, pp.172–179. 2013.

Conference papers

- A. Valavanis, **A. Grier**, J. D. Cooper, C. A. Evans, and P. Harrison *Quantum Wells, Wires and Dots (QWWAD): Free and opensource simulation tools for semiconductor nanostructures* The 13^{th} International Conference of Intersubband Transitions in Quantum Wells , Vienna, Austria, 6–11 September 2015.

- G. Agnew, **A. Grier**, T. Taimre, Y.L. Lim, A. Valavanis, J. D. Cooper, P. Dean, S.P. Khanna, M. Lachab, E. H. Linfield, A. G. Davies, P. Harrison, Z. Ikonić, D. Indjin, and A.D. Rakić *A QCL model with integrated thermal and stark rollover mechanisms* Conference on Optoelectronic and Microelectronic Materials & Devices (COMMAD), pp.48–51, 2015.

- * **A. Grier**, A. Valavanis, J. D. Cooper, P. Harrison, Z. Ikonić and D. Indjin *Influence of barrier height on interface roughness scattering and coherent transport in AlGaAs quantum cascade lasers* International Quantum Cascade Lasers School and Workshop, Policoro, Italy, 7–12 September 2014.

- * **A. Grier**, A. Valavanis, J. D. Cooper, P. Harrison, Z. Ikonić and D. Indjin *Extended density matrix model applied to tall barrier quantum cascade lasers* UK Semiconductor, Sheffield, United Kingdom, 9–10 July 2014.

- * **A. Grier**, Z. Ikonić, A. Valavanis, J. D. Cooper, D. Indjin, and P. Harrison

Transport modelling of AlGaN and AlGaAs resonant tunnelling diodes Theory, Modelling, and Computational Methods for Semiconductors, Manchester, United Kingdom, 22–24 January 2014.

- * **A. Grier**, Z. Ikonić, A. Valavanis, J. D. Cooper, D. Indjin, and P. Harrison *Density Matrix Model Applied to GaAs and GaN-based Terahertz Quantum Cascade Lasers* International workshop on computational electronics, Nara, Japan, 4–7 June 2013.

- * **A. Grier**, Z. Ikonić, A. Valavanis, J. D. Cooper, D. Indjin, and P. Harrison *Coherent transport and gain in GaAs and GaN quantum cascade lasers* MPNS COST Action Training School - TERA-MIR Radiation: Materials, Generation, Detection and Applications, Cortona, Italy, 20–24 May 2013.

- C. Edmunds, L. Tang, J. Shao, D. Li, G. Gardner, M. Manfra, O. Malis, **A. Grier**, Z. Ikonić, P. Harrison, and D. Zakharov *Comparative Study on Intersubband Absorption in AlGaN/GaN and AlInN/GaN Heterostructures Grown on Low-Defect Substrates* American Physical Society Meeting, Baltimore, Maryland, 18–22 March 2013.

- * **A. Grier**, J. D. Cooper, L. Lever, A. Valavanis, Z. Ikonić, D. Indjin, P. Harrison, C. Edmunds, J. Shao, L. Tang, G. Gardner, D. Zakharov, M. J. Manfra, and O. Malis *A scattering rate approach to the understanding of absorption line broadening in near-infrared AlGaN/GaN quantum wells* 6th Space Agency - MOD Workshop on Wide Bandgap Semiconductors and Components, ESA-ESTEC, Noordwijk, Netherlands, 8–9 October 2012.

- J. D. Cooper, **A. Grier**, A. Valavanis, L. Lever, Z. Ikonić, P. Harrison and J. E. Cunningham *Modelling surface acoustic wave modulation of the carrier concentration in quantum cascade lasers for broadband tuneability* International

Quantum Cascade Lasers School and Workshop, Bade, Austria, 2–6 September 2012.

List of abbreviations

BTC	Bound-to-continuum
CB	Conduction band
FCC	Face-centred cubic
FWHM	Full-width at half-maximum
LLL/ULL	Lower/upper laser level
LO/LA	Longitudinal optic/acoustic (phonon)
MBE	Molecular beam epitaxy
ML	Monolayer
NEGF	Nonequilibrium Green's function
QCL	Quantum cascade laser
QW	Quantum well
RP	Resonant phonon
RTD	Resonant tunnelling diode
TEM	Transmission electron microscopy
THz	Terahertz
TO/TA	Transverse optic/acoustic (phonon)

List of symbols

Fundamental constants

$c = 3.00{\times}10^{8}\,\mathrm{m/s}$	Speed of light in vacuum
$e = 1.60{\times}10^{-19}\,\mathrm{C}$	Elementary charge
$\varepsilon_0 = 8.85{\times}10^{-12}\,\mathrm{F/m}$	Vacuum permittivity
$\hbar = 1.05{\times}10^{-34}\,\mathrm{J\,s}$	Reduced Planck constant
$k_\mathrm{B} = 1.38{\times}10^{-23}\,\mathrm{J/K}$	Boltzmann constant
$m_e = 9.11{\times}10^{-31}\,\mathrm{kg}$	Rest mass of free electron

Mechanical notation

E	Energy
E_k	Kinetic energy
k	Wavevector
m	Mass
t	Time
ψ, ϕ	Wavefunction
ω	Angular frequency

Thermal properties

T	Lattice temperature
T_e	Electron temperature

Material properties

a	Lattice constant, bowing parameter
E_c	Energy of conduction band edge
E_g	Bandgap energy
ε, ε_r	Permittivity, dielectric constant
k_0	Wavevector of conduction band minimum
m^*	Effective mass at conduction band edge
ρ	Mass density
v_s	Speed of sound

Electronic properties

$z_{i,j}$	Dipole matrix element
E_F	Quasi-Fermi energy
f_{FD}	Fermi-Dirac occupation probability
$\hat{H}$, H	Hamiltonian operator
n	Total electron density
ρ	Charge density
V_F	Potential due to internal/external electric fields

Gain and current density

α_m, α_w	Mirror/waveguide loss
f_{ij}	Oscillator strength
γ_{ij}	Half-width at half maximum (linewidth)
g	Gain coefficient
G	Gain
G_{th}	Threshold gain
Γ	Modal overlap factor
J	Current density
λ	Wavelength
L_{ij}	Lineshape (Lorentzian)
n	Refractive index
R	Facet reflectivity

Scattering parameters

A	Cross-sectional area
Δ, Λ	Interface roughness height, correlation length
ΔV_{ad}	Alloy disorder potential
F_{ij}, B_{if}	Interface roughness scattering matrix element
$\boldsymbol{q} = (q, \theta_q)$	Scattering vector (magnitude, angle)
τ	Lifetime
$\tau_{\|\|}$	Dephasing time
V_{ij}	Perturbation matrix element
W_{ij}, $W_{ij\to fg}$	Scattering rate
Ω	Volume containing single lattice site

Coulombic scattering

$A_{ij \to fg}$	Electron-electron scattering matrix element
I_{if}	Coulombic scattering matrix element
J_{if}	Ionised impurity scattering matrix element
k_F	Fermi wavevector
Π_{ii}	Polarisation factor
q_{TF}	Thomas-Fermi screening vector

Phonon scattering

D_{A}	Acoustic phonon deformation potential
G_{if}	Phonon scattering matrix element
ω_q	Phonon angular frequency

Contents

List of Tables

List of Figures

Chapter 1

Introduction

This work discusses the theory, design and applications of $Al_xGa_{1-x}As/GaAs$ and $Al_xGa_{1-x}N/GaN$ intersubband devices including: quantum wells (QWs), resonant tunnelling diodes (RTDs) and quantum cascade lasers (QCLs). This introduction provides the relevant background material necessary to explain basic operation of these devices, the motivation for developing terahertz (THz) radiation sources and possible applications to be modelled. This chapter also describes the motivation behind the development of GaN-based intersubband devices.

1.1 Intersubband transitions

Intersubband (ISB) transitions refer to electrons (or holes) transitioning between energy states confined in either the conduction band (or valence band) of a heterostructure. Quantum wells formed by a layer of semiconductor material surrounded by layers of a higher bandgap material provide confinement in one dimension (conventionally referred to as the $z-$ plane). These 1D structures cause electrons to take on discrete energy levels inside the well; however since there is no confinement in

the x and y planes, energy levels are given by

$$E = E_n + \frac{\hbar^2|k|^2}{2m^*} \tag{1.1}$$

where n is the energy level, k is the in-plane wavevector, and m^* is the effective mass of the material. Thus, there are a continuous range of allowed energies associated with each energy level referred to as "subbands".

ISB transitions were first observed by Ando *et al.* in 1982 [1] as an optical transition between two closely spaced energy levels formed in a 2D electron gas (2DEG) at a silicon-silicon dioxide interface; ISB absorption in a quantum well was then demonstrated at shorter mid-infrared wavelengths by West and Eglash in 1985 [2] in a GaAs quantum well. These developments laid the groundwork for lasers based on ISB transitions.

1.2 Basic laser principles

Three types of electron-photon interactions exist: spontaneous emission, absorption and stimulated emission. Electrons will emit or absorb photons of energy $\hbar\omega$ if available electron energy level separations are approximately equal to the incident photon energy. An electron in an excited energy level may spontaneously emit a photon and transition to a lower energy level (figure 1.1(a)). However, if an electron lies in a lower energy level, it will absorb the energy of the incident photon and be promoted to the upper energy level (figure 1.1(b)). Stimulated emission (figure 1.1(c)) refers to an electron originally in the upper energy level interacting with a photon, causing it to emit a second photon with the same phase coherence and drop to the lower energy level. Systems in equilibrium (i.e. with no external bias or optical pumping applied) will have a thermal distribution where there are more electrons in the lower level than upper, and this will lead to ISB absorption being dominant. Light amplification through the stimulated emission of radiation (a

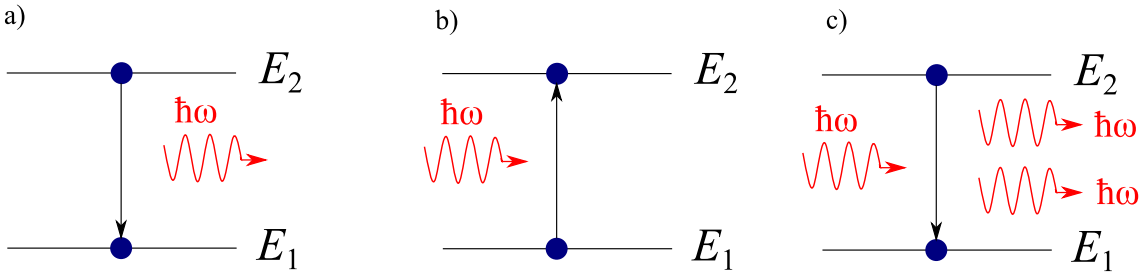

Figure 1.1: (a) Spontaneous emission occurs when an electron in a higher energy state randomly transitions to a lower energy level and emits a photon. (b) Absorption occurs when an electron interacts with a photon (absorbing its energy) and is excited to a higher energy level. (c) Stimulated emission occurs when an electron in a higher energy state interacts with a photon and drops to a lower energy level, emitting a photon with the same phase as the incident photon.

LASER) is achieved by having a non-equilibrium system where more electrons are in the upper laser level; photons then cause more emitted photons each time they interact with an excited electron, causing an intense, coherent and unidirectional light field when in a laser cavity [3].

The energy levels available to electrons in conventional semiconductor diode lasers are determined by the bandgap of the crystal structure, with electrons in the conduction band recombining with holes in the valence band. While a slight variation of the energy difference is possible by strain in some material systems, engineering the transition to be significantly lower than the bandgap energy is not possible [4, 5]. Quantum wells can be used in interband lasers so that transitions are between discrete energy levels in the conduction band to discrete levels in the valence band. While this can be used to increase the frequency as energy separation increases, emission with photon energies below the bandgap is still not possible.

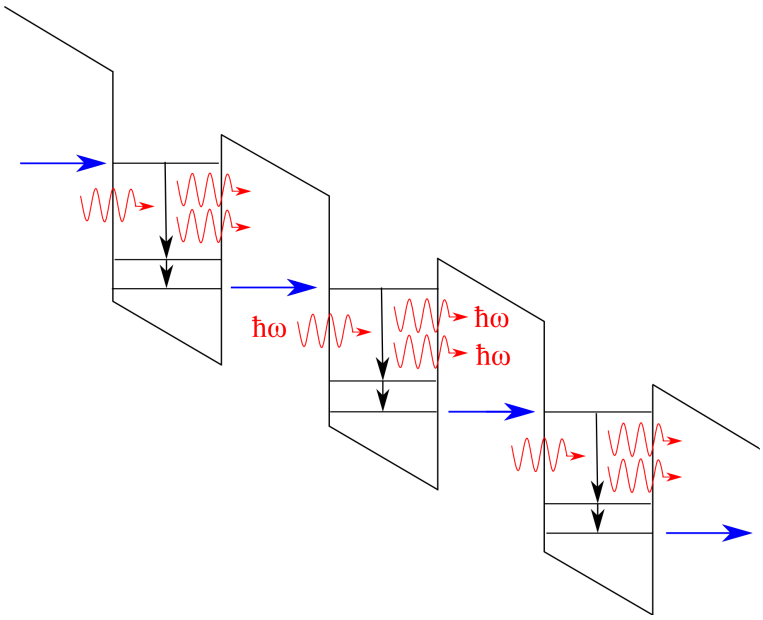

Figure 1.2: Simplified representation of lasing operation in a QCL. Electrons are injected into excited discrete energy levels which then interact with a photon causing stimulated emission. Electrons in the lower lasing level are then extracted to maintain a population inversion before being injected into another period.

1.3 Quantum cascade lasers

Quantum cascade lasers (QCLs) rely on many of the quantum wells described previously coupled close to one another. The discrete energy levels present in these systems are dependent on the thicknesses of the layers which form the wells and barriers. These can be engineered so that the energy levels provide an energy separation equal to a desired emission frequency as well as provide a fast depopulation of the lower lasing level necessary for a population inversion. These processes are between the confined subbands of the system, and as such QCLs are “unipolar” intersubband devices since transport through the devices occurs in one band only. Electrons are transported through many periods of the structure, and are therefore recycled for each photon emission in a “cascading” mechanism, leading to low

threshold currents. Figure 1.2 shows how one electron can cause the emission of many photons via the cascade mechanism.

A mid-IR (λ =4.2 µm) QCL was first demonstrated by Capasso's group at Bell labs in 1994 [6] with the $In_xGa_{1-x}As$/InAlAs material system, and the first THz QCL (λ = 68 µm) in 2002 [7] with the $Al_xGa_{1-x}As$/GaAs material system. The current high temperature record for THz QCLs is 200 K [8] and THz output powers have recently exceeded 1 W [9], both achieved with $Al_xGa_{1-x}As$/GaAs active regions. Mid-IR QCLs have recently reached powers of 190 W at room temperature (RT) [10] and have seen wall plug efficiency increase from 0.15% to greater than 50% [11].

Since QCLs rely on repeated transport of electrons between states, they provide an excellent system in which to study quantum mechanics. The population inversion needed for lasing is achieved by exploiting other mechanisms for electrons to transition between energy levels in a process known as scattering; these scattering processes are critical to both the electronic and optical properties of RTDs, QWs and QCLs.

1.4 $Al_xGa_{1-x}N$/GaN intersubband devices

While work was beginning on QCL structures in other material systems, GaN materials were being developed for interband blue-UV diode and quantum well lasers as well as solid state lighting [12]. ISB experimental work in nitride materials was first demonstrated by Gmachl *et. al.* at Bell Labs in 1999 [13] for λ = 1.75–4.2 µm and absorption at λ=1.55 µm was demonstrated soon after that [14]. $Al_xGa_{1-x}N$/GaN has several significant differences from $Al_xGa_{1-x}As$/GaAs materials: an LO phonon energy of 92 meV rather than 36 meV offers a promising solution to the main mechanisms that cause $Al_xGa_{1-x}As$/GaAs QCLs to stop working below room temperature. Additionally the conduction band offset at an AlN/GaN interface is $\approx$ 2 eV,

which provides a comfortable margin for QCLs designed to emit at 1.55 µm where telecommunication silica optical fibres have an absorption minimum.

Nitride QCLs have not yet been realised due to defects which are caused by growth problems exacerbated by the lattice mismatch of AlN and GaN. Additionally, theoretical models have recently suggested that initial nitride designs significantly overestimated gain by assuming a fixed linewidth [15, 16]. LO phonon scattering is inversely proportional to the static and high-frequency permittivities of the material which are lower in $Al_xGa_{1-x}N/GaN$. Therefore, previous work which assumed a fixed linewidth did not account for the significantly shorter lifetimes in structures relying on longitudinal optical (LO) phonon depopulation of the lower laser level. Design of nitride QCLs is also made significantly more complex due to the presence of large internal electric fields caused by the asymmetric wurzite crystal structure which themselves vary with layer thicknesses.

Work toward AlGaN devices has been intensive over the last decade and recent breakthroughs in molecular beam epitaxy (MBE) have led to the first demonstrations of THz intersubband absorption [17, 18], mid-IR and THz electroluminescence [19, 20] (where spontaneous emission occurs due to a population inversion insufficient to allow lasing) and RTDs [21–23]. These demonstrations indicate that nitride QCLs may soon be realised experimentally and some of the current experimental efforts are analysed theoretically in the present work.

1.5 Resonant tunnelling diodes

Resonant tunnelling diodes (RTDs) consist of a single quantum well with finite barriers near highly doped contact layers. When a field is applied to the RTD, the well structure tilts and the quantised well states come in and out of alignment with electrons present in the “emitter” reservoir of the device as illustrated in figure 1.3. The

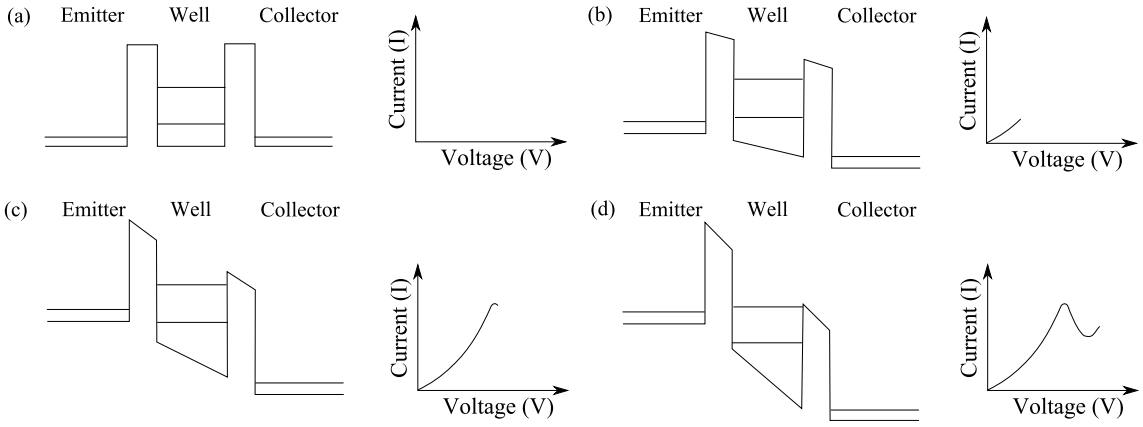

Figure 1.3: Simplified representation of a resonant tunnelling diode: (a) with no applied bias the current is zero. (b) As a bias is applied across the well the states become increasingly aligned (c) with electrons at conduction band edge in emitter. (d) The current peaks when a quantum well state is aligned with the emitter and subsequently decreases after alignment.

resulting current–voltage (I–V) curve features peaks when states are in alignment and valleys when out of alignment. Regions where states are increasingly going out of alignment after a peak are described as regions of negative differential resistance (NDR), and this property has potential applications in bi-stable circuits, differential comparators and oscillators [24]. RTDs have received a great deal of interest since the pioneering work by Esaki and Tsu [25] due to the complex behaviour of their apparent simple structure.

Characterisation of the electron transport properties of these structures is critical for the realisation of nitride QCLs and theoretical models to investigate underlying physics are in great demand. Reliable and repeatable demonstrations of $Al_{0.18}Ga_{0.82}N$/GaN resonant tunnelling diodes have recently been shown for temperatures up to 77 K [23]. Further modelling of these devices is necessary to establish the feasibility of reliable resonant tunnelling at higher temperatures.

1.6 Terahertz radiation

The THz frequency range is typically defined as the frequencies between 300 GHz and 10 THz. A major motivation for the development of THz radiation sources is to exploit its wavelength for security, medical and sensor applications [26, 27]. The energy of THz radiation is resonant with that of inter- and intra- molecular bond lengths for many biological and chemical materials allowing strong absorption in polar materials. This has an additional benefit of relatively small absorption in non-polar materials which are typically used in packaging, allowing non-invasive scanning through them. Terahertz imaging has demonstrated excellent differential ability for many common drugs-of-abuse and explosives [27], and has promising applications in the early diagnosis of skin cancer [28].

However, while there is great demand for THz sources, a THz gap exists in the electromagnetic spectrum due to it lying above the energy level of many electronic sources such as Gunn diodes, and below that of optical sources such as lead-salt or conventional diode lasers which are restricted by the material bandgap [26]. The recent increases in output power and high temperature operation mean that QCLs are a promising THz source and this is a main drive for QCL development.

One promising application of THz QCLs is with self-mixing via optical feedback. By emitting THz radiation onto a target and injecting the reflected light back into the lasing cavity, terminal voltage variations can be measured and used to determine the phase or amplitude of the reflected light. In this way, the QCL can be used as a source and a detector and a cooled bolometer detector is no longer necessary. Imaging through self-mixing with THz QCLs was first demonstrated by Dean *et al.* in 2011 [29] with a bound to continuum (BTC) QCL at 25 K with an emission frequency of 2.60 THz. Research interests in this area lie with 3D imaging [30] and self-mixing with QCLs in pulsed mode allowing their use at their highest operating temperature.

1.7 Thesis structure

The main objective of this thesis is to investigate the physics underlying the optical and electronic transport properties of AlGaAs and AlGaN intersubband devices. A secondary aim is the optimisation of structures for future improvement. Chapter 2 describes the properties of these material systems as well as the origin of internal electric fields which are critical to modelling of nitride devices. This chapter also addresses the computational methods for determining the energy eigenstates for electrons in a superlattice heterostructure. Fermi's golden rule is used in Chapter 3 to outline the incoherent scattering mechanisms relevant in intersubband devices. Both Chapters 2 and 3 are intended to give only the computational and scattering models used and contain little original work. The concept of density matrices and a density matrix (DM) model for QCLs are presented in Chapter 4. This chapter also presents results of DM simulations for the current high temperature record THz QCL structure. These are then compared with rate equation, non-equilibrium Green's function and experimental results shared by collaborators to validate the model.

It is shown in Chapter 5 how the validated DM QCL model can be used to explain recent experimental results with tall-barrier structures designed to suppress leakage current which can affect high temperature performance. Additionally, this chapter shows how active regions can be optimised using a genetic algorithm and new structures are proposed for both GaAs and GaN material systems. Chapter 6 describes how the model can be used to explain the origin of voltage variations in self-mixing applications, and replicate the increased sensitivity of a structure recently grown and characterised by colleagues at the University of Leeds.

These validated models are then used in Chapter 7 to explain the origin of linewidth broadening in AlGaN/GaN near-Infrared intersubband absorption structures grown by collaborators at Purdue University, USA and other state of the art

devices in current literature. This chapter is based on the work in Refs. [31] and [32]. Chapter 8 describes the transport of electrons through AlGaN sequential tunnelling devices and RTDs with a density matrix formalism derived by the present author.

Finally, chapter 9 summarises and concludes the work, outlining ideas for future research that could be based on that within.

Chapter 2

$Al_xGa_{1-x}As$ and $Al_xGa_{1-x}N$ heterostructures

Chapter 1 described how alternating layers of semiconductor crystal can form quantum wells which lead to confinement of electrons. This chapter discusses the bandstructure of $Al_xGa_{1-x}As$/GaAs and $Al_xGa_{1-x}N$/GaN heterostructures as well the internal electric fields caused by uneven charge distributions. Additionally, the internal electric fields caused by the asymmetric crystal structure in $Al_xGa_{1-x}N$/GaN is shown to significantly modify the bandstructure. The Hamiltonian of the system (without scattering terms) along with computational methods for solving both Schrödinger and Poisson equations is presented.

2.1 Schrödinger equation

According to quantum mechanics, an electron in a vacuum acts as a state function in the form of a wave:

$$\psi = e^{i(\mathbf{k}\bullet\mathbf{r}-\omega t)} \tag{2.1}$$

where ω is the angular frequency, t is the time, $\boldsymbol{r}$ is the position vector, and $|\mathbf{k}| = \frac{2\pi}{\lambda}$. This wave with a given wavelength is associated with any particle with a momentum p by the relation [33]:

$$\lambda = \frac{h}{p} \tag{2.2}$$

where h is Planck's constant. Momentum eigenvalues can be found using the momentum operator $\mathbf{p}$ on the electron wavefunction [33]:

$$-i\hbar\nabla\psi = \mathbf{p}\psi \tag{2.3}$$

where

$$\nabla = \frac{\partial}{\partial x}\hat{\mathbf{i}} + \frac{\partial}{\partial y}\hat{\mathbf{j}} + \frac{\partial}{\partial z}\hat{\mathbf{k}} \tag{2.4}$$

In a vacuum where no additional potential exists, the total energy, E, of an electron is given by its kinetic energy and can be found from the particle momentum with the time-independent Schrödinger equation [33]:

$$-\frac{\hbar^2}{2m}\nabla^2\psi = E\psi \tag{2.5}$$

The dispersion relation (which refers to the relationship between energy and momentum of the particle) implies that

$$E = \frac{\hbar^2 k^2}{2m} \tag{2.6}$$

In a crystal structure, the periodic arrangement of atoms introduce an additional interaction for electrons caused by Coulomb interactions. Typically this is very complex, and a simple solution to this is the introduction of an effective mass for a specific material in place of the free electron mass. This changes the time-independent Schrödinger equation and energy eigenvalues to:

$$-\frac{\hbar^2}{2m^*}\nabla^2\psi = E\psi \tag{2.7}$$

and

$$E = \frac{\hbar^2 k^2}{2m^*} \tag{2.8}$$

The periodic structure of the crystal lattice also forbids a range of electron energy levels known as the bandgap, E_g between two distinct energy bands. Covalent bonds binding atoms together in the lattice provide empty states for electrons to transition between in the lower of these bands (known as the valence band).

The conduction (upper) band is typically empty at low temperatures in a semiconductor under equilibrium and thus they are semi-conducting, or conduct only when electrons are excited into it. Introducing dopant atoms to replace certain crystal sites (Al replacing Ga atoms in the present work) introduces different bond lengths and therefore different bandgaps and effective masses to the system. The time-independent Schrödinger equation of each energy band is now modified to include the additional crystal potential $V(z)$ which has a spatial dependence:

$$-\frac{\hbar^2}{2m^*}\frac{\partial^2}{\partial z^2}\psi(z) + V(z)\psi(z) = E\psi(z) \tag{2.9}$$

In a semiconductor heterostructure made up of alternating wells and barriers, there are an equivalent number of heterojunctions where the material parameters change abruptly; however the wavefunction of particles should remain continuous across the boundary. For a bandstructure where particles are confined in the $z-$ direction, Eq. (2.9) discretises the total potential $V(z)$ at each spatial point.

To solve this equation computationally, the numerical approximations for first and second derivatives are used. The first derivative of the wavefunction that could be used in Eq. (2.9) is given by [33]:

$$\psi'(x) \approx \frac{\psi_i - \psi_{i-1}}{\delta z} \tag{2.10}$$

where i is the index of the ith spatial layer and δz is the spatial step size between two adjacent indexes. Applying this to itself to get the second derivative gives:

$$\psi_i'' \approx \frac{\psi_{i+1} - 2\psi_i + \psi_{i-1}}{\delta z^2}, \tag{2.11}$$

Substituting this into the Schrödinger equation (Eq. (2.9)) gives it in its discretised form:

$$-\frac{\hbar^2}{2m^*}\left[\frac{\psi_{i+1}-2\psi_i+\psi_{i-1}}{\delta z^2}\right]+V_i\psi_i=E\psi_i. \tag{2.12}$$

Solving this numerically to obtain the energy levels and wavefunctions of the band-structure can be achieved by techniques such as the shooting method or matrix methods. Throughout the present work, matrix methods were chosen for their reliability in finding states lying close together in energy: a requirement for equilibrium coupled well structures and THz QCLs with small energy separations. In the matrix method approach, Eq. (2.9) can be solved as a number of simultaneous equations of the form [34]:

$$a_i\psi_{i-1}+b_i\psi_i+c_i\psi_{i+1}=E\psi_i, \tag{2.13}$$

where the a, b and c coefficients assuming a constant effective mass are defined as [34]:

$$\begin{aligned} a_{i+1}=c_i &= -\frac{\hbar^2}{2m^*\delta z^2} \\ b_i &= \frac{\hbar^2}{m^*\delta z^2}+V_i. \end{aligned} \tag{2.14}$$

All solutions for the Schrödinger equation require the wavefunctions to be defined at their initial and final spatial points: for structures such as the QWs and QCLs considered in this work the confining potential is periodic. Wavefunctions will therefore spread over a few hundred nanometres of the device before decaying exponentially to zero. A box which contains all the wavefunction can be introduced by setting the initial and final wavefunction points to be zero, so that the matrix to be solved

is [34]:

$$\underbrace{\begin{pmatrix} b_0 & c_0 & 0 & \cdots & 0 \\ a_1 & b_1 & c_1 & \cdots & 0 \\ 0 & \ddots & \ddots & \ddots & 0 \\ 0 & \cdots & a_{N-2} & b_{N-2} & c_{N-2} \\ 0 & \cdots & 0 & a_N & b_{N-1} \end{pmatrix}}_{\mathsf{H}} \underbrace{\begin{pmatrix} \psi_0 \\ \psi_1 \\ \vdots \\ \psi_{N-2} \\ \psi_{N-1} \end{pmatrix}}_{\boldsymbol{\psi}} = E \underbrace{\begin{pmatrix} \psi_0 \\ \psi_1 \\ \vdots \\ \psi_{N-2} \\ \psi_{N-1} \end{pmatrix}}_{\boldsymbol{\psi}} \tag{2.15}$$

The LAPACK [35] package for C++ is a suitable library for numerical solution of this equation and was used in this work.[1] To account for a varying effective mass it can be shown that the coefficients in Eq. 2.15 become [36]:

$$\begin{aligned} a_{i+1} = c_i &= -\frac{\hbar^2}{2m^*_{i+\frac{1}{2}}\delta z^2} \\ b_i &= \frac{\hbar^2}{\delta z^2}\left(\frac{1}{m^*_{i+\frac{1}{2}}} + \frac{1}{m^*_{i-\frac{1}{2}}}\right) + V_i. \end{aligned} \tag{2.16}$$

where the intermediate mass values $m_{i-\frac{1}{2}}$ and $m_{i+\frac{1}{2}}$ are calculated as the mean of neighbouring points at z_i and $z \pm \delta z$. Additionally, matrix methods allow for the inclusion of "non-parabolicity" effects where the electron effective mass is also dependent on energy according to:

$$m^*(z, E) = m^*_{z,0}(1 + \alpha E) \tag{2.17}$$

where α is the nonparabolicity coefficient given by $(1/E_g)$. This affects the energy levels and dispersion curves of the subbands, and is important in devices with states lying far above the band edge. For devices where this could be important the approach used in Ref. [37] is used.[1]

[1] Using code written by A. Valavanis and J. D. Cooper at the University of Leeds.

2.2 Electric fields

In optical and electronic applications the bandstructure has an external bias applied to the device to induce current flow. This affects the conduction band potential so that it now becomes:

$$V_F(z) = V(0) - zF \tag{2.18}$$

where F is the applied field typically given in kV/cm. In addition to the externally applied bias, the carriers and ionised dopants create an internal electric field due to a charge distribution given by:

$$\rho(z) = e(N_d^+(z) - n(z)) \tag{2.19}$$

where N_d^+ is the spatial distribution of ionised donors and $n(z)$ is the spatial distribution of electrons spread across the structure wavefunctions. The potential due to these charges, V_{P} is found by solving Poisson's equation

$$\frac{\mathrm{d}^2 V_{\mathrm{P}}(z)}{\mathrm{d}z^2} = -\frac{e}{\epsilon_0 \epsilon_r}\left[N_d^+(z) - n(z)\right] \tag{2.20}$$

by a finite difference method similar to that for the Schrödinger equation. The matrix to be solved is [38]:

$$\begin{pmatrix} -2 & 1 & 0 & \cdots & 0 \\ 1 & -2 & 1 & \cdots & 0 \\ 0 & \ddots & \ddots & \ddots & 0 \\ 0 & \cdots & 1 & -2 & 1 \\ 0 & \cdots & 0 & 1 & -2 \end{pmatrix} \begin{pmatrix} V_{\mathrm{P},1} \\ V_{\mathrm{P},2} \\ \vdots \\ V_{\mathrm{P},N-1} \\ V_{\mathrm{P},N} \end{pmatrix} = -\frac{e\delta z^2}{\epsilon_0 \epsilon_r} \begin{pmatrix} \rho_1 \\ \rho_2 \\ \vdots \\ \rho_{N-2} \\ \rho_N \end{pmatrix} \tag{2.21}$$

where ρ_i is the charge density at position index i and N is the total number of points in the system. The charge density used is given by Eq. (2.19).

An improved approach is to calculate the effect of the applied field and charge density together by solving the Poisson equation with boundary conditions that

force V_F at the start of the period to be 0, and force V_F at the end of the period with length L_p to be $-FL_p$. Simulations completed in this work use this approach which is presented in Ref. [34].[1]

To find the static bandstructure of the device, the Schrödinger and Poisson equations must be solved iteratively since the confinement potential used to find the state wavefunctions depends on the charge distribution which itself relies on the wavefunctions. In QCL simulations (described in Chapter 4) convergence is typically achieved after four Schrödinger–Poisson (S–P) iterations, however an exception to this is found in Chapter 7 when damping is required.

2.3 Charge distribution

The charge distribution is determined by both the donor atom profile as well as the electron charge density. In QCL devices all donors are assumed to be ionised due to the availability of states for donated electrons to occupy. An exception exists for heavily doped structures or those with no bias applied. For a donor atom to contribute an electron to the device, some energy E_{D} must be supplied to ionise it from the lattice. This "activation" energy is 6 meV and 20 meV for Si donors in GaAs [39] and GaN materials [40] respectively.

For a structure where the Fermi energy is known the density of ionised donors in Eq. 2.20 is given by [40]:

$$N_{\mathrm{D}^+}(z) = N_D(z) f_{\mathrm{d}}^+(z) \tag{2.22}$$

where $N_D(z)$ is the dopant density and $f_{\mathrm{d}}^+(z)$ is the probability that an impurity with a degeneracy of 2 is ionised [40]:

$$f_D^+(z) = 1 - \frac{1}{1 + \frac{1}{2}\exp\left[\dfrac{E_D(z) - Ef}{k_{\mathrm{B}}T}\right]}. \tag{2.23}$$

[1] Using code written by A. Valavanis and J. D. Cooper at the University of Leeds.

where E_{F} is the Fermi energy for the device.

Alternatively in structures where all dopants are assumed to be ionised so that:

$$N_{\mathrm{D}^+}(z) = N_D(z) \tag{2.24}$$

the Fermi energy, E_{F}, can be found iteratively using:

$$N_{\mathrm{total}} = \sum_{i=1}^{n} \frac{m^* k_{\mathrm{B}} T}{\pi \hbar^2} \ln\left(1 + \exp\left[-(E_i - E_{\mathrm{F}})\right]\right) \tag{2.25}$$

where N_{total} is the total ionised sheet density and E are the energies of the set of subbands. Note that this is still the case of an equilibrium structure since only one Fermi energy is present.

However, QCL structures are not in equilibrium with an applied bias and their populations are determined by the scattering and tunnelling processes discussed in later chapters. Within each subband the electron distribution is assumed to be a Fermi–Dirac distribution given by:

$$f_{\mathrm{FD},i}(E_k, T_{e,i}) = \frac{1}{\exp\left[\frac{E_k - E_{F,i}(T_{e,i})}{k_B T_{e,i}}\right] + 1}. \tag{2.26}$$

where E_k is the wavevector energy and $E_{\mathrm{F},i}$ and $T_{e,i}$ are now the quasi Fermi-energy of the ith subband and the electron temperature respectively. This approximation is justified by considering fast electron–electron scattering causing thermalisation of electrons [41]. Since the subband populations will be known later by the density matrix approach, the quasi Fermi energies of each subband can be found by an iterative solution of:

$$n_i = \frac{m_d k_B T_e}{\pi \hbar^2} \left\{ \frac{E_{F,i}(T_e)}{k_B T_e} + \ln\left[1 + \mathrm{e}^{\frac{E_{F,i}(T_e)}{k_B T_e}}\right] \right\}. \tag{2.27}$$

to find the quasi Fermi energy which returns the subband population. The spatial electron density due to electrons confined in subband i is given by:

$$n_i(z) = n_i |\psi_i(z)|^2 \tag{2.28}$$

and the total electron charge density at z is given by summing over all subbands for use in Eq. (2.19).

2.4 Material Properties

GaAs is a III-V direct bandgap semiconductor with a zinc blende structure which is face centred cubic (fcc). Quantum well barriers are formed by replacing Ga atoms with Al to form a $Al_xGa_{1-x}As$/GaAs alloy where $0 < x < 1$. With the introduction of Al content, the bandgap increases from 1.42 eV (GaAs) to 2.16 eV (AlAs). At a AlAs/GaAs heterojunction, the CB and VB alignment is such that 33 per cent of the total discontinuity is in the valence band [33]. Therefore the conduction band discontinuity $\Delta V_{\mathrm{CB}} = 0.67 E_{\mathrm{g}}$ [33]. At around $x = 0.45$ $Al_xGa_{1-x}As$/GaAs becomes an indirect semiconductor with the lowest conduction band energy at the X-valley. The majority of the present work involves low Al concentrations ($x < 0.25$), however in cases where pure AlAs barriers are used, the indirect valley is assumed not to have a significant effect as electrons are confined mainly to the GaAs well layers. It should also be noted that the change in lattice constant with increasing alloy content is negligible, and as a result of this defects due to lattice mismatch are not significant in AlGaAs materials, leading to very high growth quality. The relevant material parameters for $Al_xGa_{1-x}As$/GaAs materials is given in Table 2.1.

Constant	GaAs	AlAs	Unit
Bandgap (direct), E_g	1.426[1]	2.673[1]	eV
Effective mass, m^*	0.067[2]	0.15 [2]	m_e
Lattice constant, a_0	5.65[2]	5.66[2]	Å
Static dielectric constant, ϵ_s	13.18[3]	10.06[3]	ϵ
High frequency dielectric constant, ϵ_{inf}	10.89[3]	8.16[3]	ϵ
Longitudinal Optical (LO) phonon energy E_{LO}	36[1]		meV
Material density, ρ	5320.0[4]		kg m^{-3}
Deformation potential, D_A	7.0[1]		eV
Electron mobility, μ	9400[5]	400[5]	cm^2 / Vs

Table 2.1: Material parameters for GaAs and AlAs. Where no AlAs values are present the GaAs value is used.

2.5 AlGaN/GaN properties

$Al_xGa_{1-x}N$/GaN preferentially forms in the wurtzite crystal structure shown in figure 2.1(a). In wurtzite structures, the center of the spatial charge distribution (barycenter) from the group III and group V atoms does not coincide along the c-axis [0001] [47] and therefore exhibits a spontaneous (also known as pyro-electric) polarisation. This is calculated using Vergard's law with a bowing factor ($C = 0.021$) included as [48]:

$$P_{\text{sp}} = xP_{\text{sp}}^{\text{AlN}} + (1-x)P_{\text{sp}}^{\text{GaN}} - Cx(1-x) \tag{2.29}$$

[1]Reference [33].
[2]Reference [42].
[3]Reference [43].
[4]Reference [44].
[5]Reference [45].

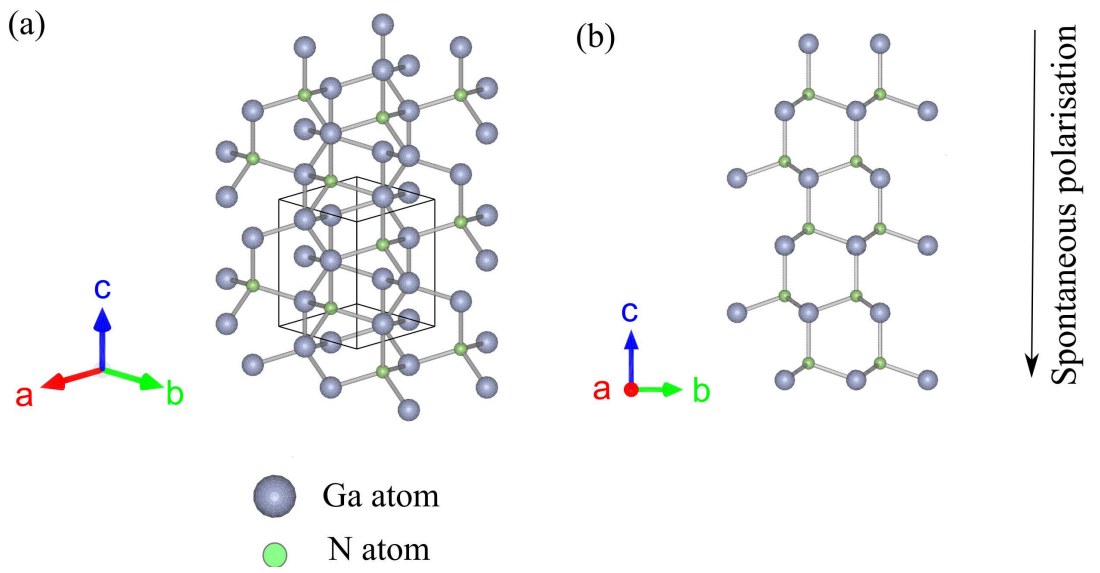

Figure 2.1: (a) Isometric and (b) side view of the hexagonal wurtzite crystal structure for GaN grown in the $c-$ axis as Ga- or N- face. Ga- face GaN refers to GaN where the direction is positive parallel to the outgoing surface, and vice-versa for N-face. Crystal structures plotted with VESTA [46].

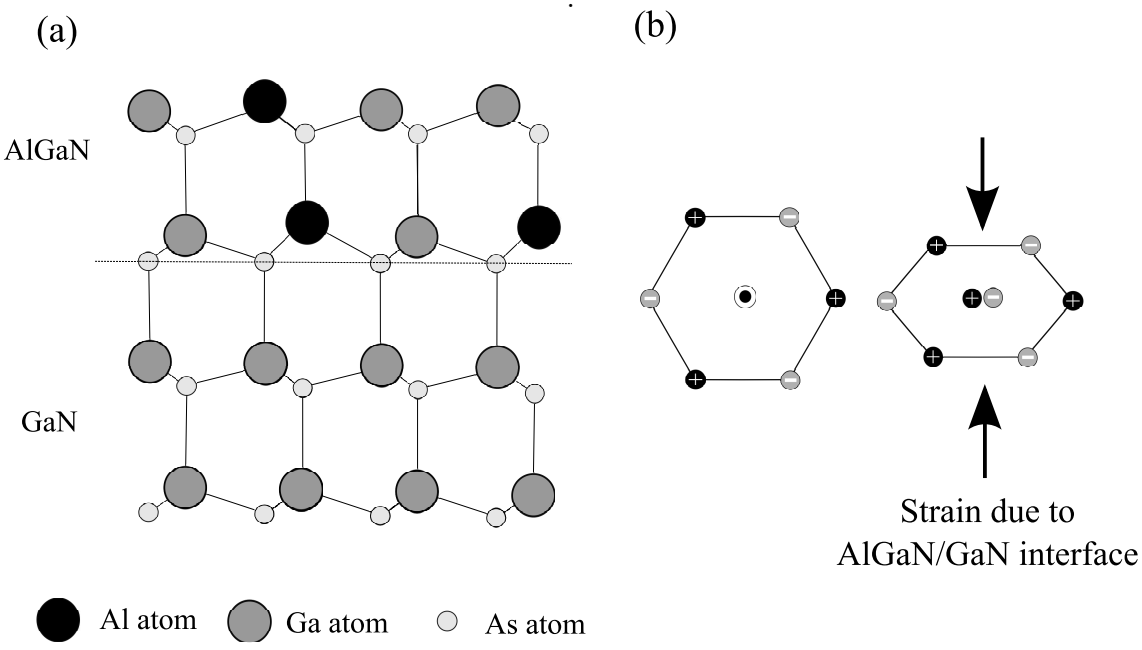

Figure 2.2: (a) Interface of an AlGaN and GaN layer causes a rearrangement of lattice atoms that (b) induces a piezoelectric polarisation contribution due to the piezeo electric effect.

where x is the molar content of AlN in the layer. The spontaneous polarisation material parameters are given in Table 2.2.

Another contribution to the polarisation arises from the piezoelectric effect caused by an $Al_xGa_{1-x}N$/GaN interface (figure 2.2(a)) which is commonly observed in other materials such as quartz. The mismatch of lattice constants between GaN and AlGaN introduce a stress that separates charges along the interface and breaks local electrostatic neutrality (figure 2.2(b)). The piezoelectric polarisation is calculated as [38]:

$$P_{\mathrm{pz},k} = 2\frac{a - a_k}{a_k}\left(e_{31} - e_{33}\frac{C_{13}}{C_{33}}\right) \tag{2.30}$$

where C_{ij} are the elastic constants, e_{ij} are the piezoelectric constants, a_k is the lattice constant of the kth layer, and a is the lattice constant of the substrate (always GaN in the present work). The total polarisation of a layer is given by the sum of individual spontaneous and piezoelectric polarisations and at $Al_xGa_{1-x}N$/GaN interfaces this property changes abruptly. The discontinuity induces a bound sheet charge according to $\sigma = \mathbf{(P1 - P2)} \cdot \hat{\mathbf{n}}$, where n̂ is the unit vector normal to the heterointerface. The polarisation fields, **(P1, P2)** are those across the junction [49].

As a result of the positive and negative bound charges an internal electric field as high as 10 MeV/cm [47] can be induced with opposite polarities in the wells and barriers causing a saw-tooth shape conduction band profile. This field can be calculated either by adding the sheet charge to the charge density used in Poisson's equation, or alternatively the field in the i^{th} layer can be calculated as [48]:

$$F_i = \frac{\sum_{k=1}^{N}\left(P_k - P_i\right)\frac{L_k}{\epsilon_k}}{\epsilon_i \sum_{k=1}^{N}\frac{L_k}{\epsilon_k}} \tag{2.31}$$

where P_i is the polarisation, L_i is the length and ϵ_i is the permittivity of the i^{th} layer. Figure 2.3(a) shows a quantum well calculated with the $Al_xGa_{1-x}N$/GaN material parameters without including internal electric fields; for a 4 nm well the energy separation is calculated to be 147 meV. With the inclusion of the internal electric fields,

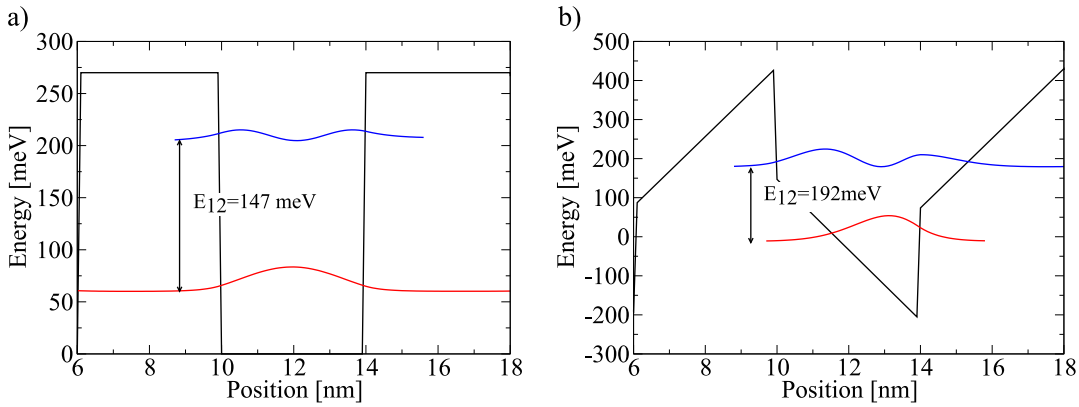

Figure 2.3: (a) Bandstructure and wavefunction plot of a 4 nm GaN well surrounded by 4 nm $Al_{0.15}Ga_{0.85}N$ barriers. Calculated with $Al_xGa_{1-x}N$/GaN material parameters but excluding internal electric fields due to spontaneous and piezoelectric polarisations. (b) Same QW with internal electric fields included. Energy separation of ground and first excited states are increased due to the triangular well potential.

the energy separation increases to 192 meV for the same well width as shown in figure 2.3(b). This can make design of a structure with a resonant phonon energy transition challenging [50] since the triangular well adds additional confinement. Another consequence of the triangular potential is that it breaks wavefunction symmetry of the ground and second excited states allowing transitions between them.

Constant	GaN	AlN	Unit
Bandgap (direct), E_g	3.51[1]	6.25[1]	eV
Effective mass, m^*	0.18[2]	0.3 [2]	m_e
Lattice constant, a_0	3.112[1]	3.189[1]	Å
Static dielectric constant, ϵ_s	10.28[3]		ϵ
High frequency dielectric constant, ϵ_{inf}	5.35[3]		ϵ
Longitudinal Optical (LO) phonon energy E_{LO}	91.3[3]		meV
Material density, ρ	6150.0[3]	3230.0[3]	kg m^{-3}
Deformation potential, D_A	8.3[3]		eV
Spontaneous polarisation, P_{SP}	-0.034[1]	-0.090[1]	C/m^2
Elastic constants			
C_{11}	390.0[1]	396.0[1]	GPa
C_{12}	145.0[1]	137.0[1]	GPa
C_{13}	106.0[1]	108.0[1]	GPa
C_{33}	398.0[1]	373.0[1]	GPa
Piezoelectric constants			
ϵ_{13}	-0.49[4]	-0.60[4]	C/m^2
ϵ_{33}	0.73[4]	1.46[4]	C/m^2
Electron mobility, μ	400[5]		cm^2 / Vs

Table 2.2: Material parameters for GaN and AlN. Where no AlN values are present the GaN value is used.

2.6 Growth of III-Nitrides

The growth of any semiconductor device will significantly affect its operation; any scattering and tunnelling transport will be influenced by defects such as dislocations, carrier traps, and interface roughness. Since $Al_xGa_{1-x}N$/GaN is not a lattice

[1]Reference [51].
[2]Reference [52].
[3]Reference [53].
[4]Reference [54].
[5]Reference [44].

matched alloy, increasing alloy content increases the strain at interfaces and therefore the likely number of defects such as threading dislocations. Two general growth methods are used for the growth of $Al_xGa_{1-x}N$/GaN intersubband devices:

- Molecular Beam Epitaxy (MBE) - Pure element sources are heated and the incident flux of the material is controlled with computer controlled shutters. Molecules then condense onto a rotating heated substrate [55] so that the devices are built up layer by layer.

- Metal Organic Chemical Vapour Deposition (MOCVD) - Elements that are to be deposited are combined with complex organic molecules. Upon arrival at the heated substrate, thermal energy breaks the molecular bond between element and organic molecule [56]. This growth technique has much faster growth rates and is widely used in industrial production of semiconductor devices.

There are many examples of MBE growth in early GaN experimental work such as that by Gmachl *et al.* [14] but in recent years there has been an increase in MOCVD growth research [57] due to its advantages of shorter growth times and lower growth temperatures. Additionally, variations of MBE growth such as plasma assisted MBE (PAMBE) and radio frequency MBE (RFMBE) have shown promising results recently [20, 58].

A major development toward GaN intersubband devices is the first demonstration of electroluminesence in 2011 which was attributed to improvements in substrate quality [20]. To investigate the effect of dislocation density Terashima *et al.* [20] switched from MOCVD growth on sapphire substrate with GaN templates to the rf-MBE approach directly onto high quality GaN substrates; the threading dislocations of these base layers is specified as 1×10^9 to 1×10^6 cm^{-2}. This work indicates that minimisation of carrier capture by dislocations is critical.

2.7 Conclusion

In this chapter the important concepts needed to calculate the steady-state band-structure and wavefunctions was presented. It was shown that electron confinement in 1D structures leads to subbands, and the confinement is affected by the confinement potential. Furthermore the significant differences between $Al_xGa_{1-x}As$/GaAs and $Al_xGa_{1-x}N$/GaN devices was described and the importance of accounting for nitride internal electric fields shown.

Chapter 3

Scattering mechanisms and transport

In order to investigate the optical and electronic properties of intersubband devices, an understanding of the transfer mechanisms between quantised states is required. This scattering can be caused by mechanisms such as interaction with structural defects, other charged particles, alloy disorder or interaction with lattice vibrations. The concepts and calculations for each scattering mechanism are presented in this chapter.[1]

[1]None of the calculations presented here were derived by the author. However, the work in the following chapters is heavily based on these scattering models and they are included as background information. Existing code written by colleagues in the quantum electronics group at the University of Leeds was updated along with A. Valavanis, J. D Cooper and P. Ivanov during the course of the present work to allow (among other things) convenient specification of the material system being investigated.

3.1 Effect on optical and electronic properties

The scattering between quantised electron states in intersubband devices determines the optical linewidth of their gain/absorption spectrum and provides different mechanisms for electrons to travel through devices. Each transition is considered to be instantaneous since the time taken for the transition is much shorter than the time between transitions. The scattering rate in and out of states can be used to determine the typical lifetime of an electron in a given state before scattering out of it. From this, linewidths are obtained using the lifetime uncertainty

$$\Delta E \Delta t \approx \frac{\hbar}{2} \tag{3.1}$$

which is known as Heisenberg's uncertainty principle. It follows from this that states with very fast scattering to another state (for example if an energy spacing is equal to the LO phonon energy of the material) then the state lifetime will be very short, and an electron undergoing an absorption transition will have a large energy broadening, ΔE, given by:

$$\Delta E \approx \frac{\hbar}{2\Delta\tau} \tag{3.2}$$

where τ is the lifetime of the state. Scattering between states in QCLs is also exploited to create a population inversion for lasing, and scattering between states leads to current flow.

3.2 Fermi's Golden rule

Scattering is the process of an electron (or holes in the valence band) changing state due to some perturbation. *Fermi's Golden Rule* states that an electron interacting with a time-dependent Hamiltonian, $\tilde{\mathcal{H}}$, will have a scattering rate given by [33]:

$$W_{\mathrm{if}} = \frac{2\pi}{\hbar} \sum_{\mathrm{f}} \left| \langle \mathrm{i} | \, \tilde{\mathcal{H}} \, | \mathrm{j} \rangle \right|^2 \delta(E_{\mathrm{f}} - E_{\mathrm{i}}) \tag{3.3}$$

where i and f are the initial and final states of the electron of energies E. The Dirac delta function, δ, ensures energy conservation and has important consequences on the nature of elastic and inelastic scattering processes. The derivation of all scattering rate calculations begin with the substitution of the relevant perturbation potentials into Eq. (3.3). In intersubband devices, several scattering mechanisms coexist: longitudinal-optical (LO) phonons, longitudinal-acoustic (LA) phonons, interface roughness (IFR), ionised impurities, electron–electron and alloy disorder scattering.

3.3 Electron-LO phonon scattering

A phonon is a periodic crystal vibration where atoms in the lattice oscillate and propagate energy. The wavefunction of a phonon in a bulk crystal can be given by [33, 59]:

$$\phi = C(\mathbf{K})\mathrm{e}^{-i\mathbf{K}_\bullet\mathbf{r}} \tag{3.4}$$

where C is a normalisation weighting coefficient and $\mathbf{K}$ is the 3D wavevector. This wavefunction describes the oscillating lattice structure and therefore potential as charged ions oscillate; the induced electric field is given by its derivative:

$$\mathbf{E} = \nabla\phi = -i\mathbf{K}\phi \tag{3.5}$$

where

$$\nabla = \frac{\partial}{\partial x} + \frac{\partial}{\partial y} + \frac{\partial}{\partial z} \tag{3.6}$$

This oscillating potential for bulk polar semiconductors can be shown to have the scattering Hamiltonian [33]:

$$\tilde{\mathcal{H}} = e\sum_{\mathbf{K}}\left(\frac{\hbar\omega P}{2|\mathbf{K}|^2}\right)^{\frac{1}{2}}\frac{\mathrm{e}^{-i\mathbf{K}_\bullet\mathbf{r}}}{\Omega^{\frac{1}{2}}} \tag{3.7}$$

where Ω is the volume of a single lattice site, ω is the material dispersionless phonon frequency and P is calculated as:

$$P = \frac{1}{\epsilon_\infty} - \frac{1}{\epsilon_s} \tag{3.8}$$

where ϵ_∞ is the high frequency permittivity and ϵ_s is the low-frequency permittivity of the material. However, this interaction term uses the bulk phonon wavevector term $\mathbf{K}$ which can be split into growth and (x–y) plane components for two dimensional carriers [33]:

$$\tilde{\mathcal{H}} = e \sum_{\mathbf{K}_{xy}} \sum_{K_z} \left(\frac{\hbar\omega P}{2\left(|\mathbf{K}_{xy}|^2 + |K_z|^2\right)} \right)^{\frac{1}{2}} \frac{\mathrm{e}^{-i\mathbf{K}_{xy}\bullet\mathbf{r}_{xy}}}{A^{\frac{1}{2}}} \frac{\mathrm{e}^{-iK_z z}}{L^{\frac{1}{2}}} \tag{3.9}$$

The phonon and quantised carrier eigenfunctions are substituted in Fermi's Golden rule (Eq. (3.3)) and after a lengthy derivation the two dimensional scattering rate due to electron-longitudinal optical phonons is calculated as [33]:

$$W_{\mathrm{if}}(k_{\mathrm{i}}) = \frac{\Upsilon''}{2} \Theta\left(k_{\mathrm{i}}^2 - \frac{2m^*\Delta}{\hbar^2}\right) \int_{-\infty}^{+\infty} \frac{\pi |G_{\mathrm{if}}(K_z)|^2}{\sqrt{K_z^4 + 2K_z^2\left(2k_{\mathrm{i}}^2 - \frac{2m^*\Delta}{\hbar^2}\right) + \left(\frac{2m^*\Delta}{\hbar^2}\right)^2}} \, \mathrm{d}K_z \tag{3.10}$$

where

$$G_{\mathrm{if}}(K_z) = \int \psi_{\mathrm{f}}^*(z) \mathrm{e}^{-iK_z z} \psi_{\mathrm{i}}(z) \, \mathrm{d}z \tag{3.11}$$

is the form factor for the transition, $\Delta = E_{\mathrm{f}} - E_{\mathrm{i}} - \hbar\omega$ for absorption and $\Delta = E_{\mathrm{f}} - E_{\mathrm{i}} + \hbar\omega$ for emission processes. The prefactor, Υ'', contains material properties including the effective mass, phonon energy and permittivities [33]:

$$\Upsilon'' = \frac{2m^* e^2 \omega P'}{(2\pi)^2 \hbar^2} \tag{3.12}$$

where

$$P' = \left(\frac{1}{\epsilon_\infty} - \frac{1}{\epsilon_s}\right)\left(N_0 + \frac{1}{2} \mp \frac{1}{2}\right) \tag{3.13}$$

N_0 is the number of phonons per unit volume determined by the Bose-Einstein factor for bosons [33]:

$$N_0 = \frac{1}{\exp(\hbar\omega/kT) - 1} \tag{3.14}$$

where T is the lattice temperature. The absorption processes where the phonon population decreases is calculated with the upper (minus) symbol in Eq. (3.13) and vice versa for emission processes. The heaviside step function in Eq. (3.10) ensures that emission only happens when the energy emission wavevector for its associated subband is at least $\hbar\omega$ above the final state. For absorption processes, an energy state must lie at least the phonon energy above the initial state. Scattering due to electron-LO phonon scattering is therefore highly dependent on the energy level separations, temperature and level of occupation of the subbands.

The oscillating crystal potential that is interacting with an electron will also be affected by other local charges locally. This reduces the scattering rate and is accounted for by altering the scattering vector with a screening length:

$$K_z^2 \longrightarrow K_z^2 \left(1 + \frac{\lambda_s^2}{K_z^2}\right)^2 \tag{3.15}$$

where λ_s is the inverse screening length. There are several possible screening models such as Park and Debye approaches [33].[1] For Park screening the inverse screening length is given by [60]:

$$\lambda_{\text{Park}}^2 = \frac{e^2}{\pi\hbar^2\epsilon_s} \sum_{\text{i}} \left\{ \frac{\sqrt{2m^* E_{\text{i}}} m^* f^{\text{FD}}(E_{\text{i}})}{\pi\hbar} \right\} \tag{3.16}$$

while the Debye screening length is given by [44]:

$$\lambda_{\text{Debeye}}^2 = \sqrt{\frac{\epsilon k_{\text{B}} T}{e^2 N_{\text{d}}}} \tag{3.17}$$

where N_{d} is the sheet dopant density.

3.4 Average scattering rate

Equation (3.10) gives the scattering rate between an initial and final wavevector associated with either the same or a different energy state. The actual scattering

[1] Debye screening used in this work as default.

rate out of a particular wavevector will depend on its probability of occupation, and the probability that its destination state is already full. Electrons in subbands have a distribution given by the Fermi-Dirac function:

$$f_{\mathrm{FD}} = \frac{1}{e^{(E_i - E_{\mathrm{f}})/kT} + 1} \tag{3.18}$$

where E_{f} is the quasi Fermi energy of the subband. The average scattering rate accounting for both states occupation probability is given by [33, 34, 61]:

$$W_{\mathrm{if}} = \frac{\int W_{\mathrm{if}}(k_{\mathrm{i}}) f_{\mathrm{i}}^{\mathrm{FD}}(k_{\mathrm{i}})[1 - f_{\mathrm{f}}^{\mathrm{FD}}(k_{\mathrm{f}})]\ k_{\mathrm{i}}\ \mathrm{d}k_{\mathrm{i}}}{\pi N_{\mathrm{i}}} \tag{3.19}$$

During the scattering rate calculations a grid in wavevector space is created from the subband minimum to $5\,k_{\mathrm{B}}T_e$ above it for THz QCLs and $100\,k_{\mathrm{B}}T_e$ for the near-IR structures in Chapter 7. This allows the upper limit of integration to increase with temperature and account for increasing electron kinetic energies. Scattering rates between initial and final subbands are calculated before averaging according to Eq. (3.19) for LO phonon and all following scattering mechanisms.

3.5 Acoustic phonon scattering

While optical phonon scattering refers to neighbouring atom vibrations being in opposite phase, acoustic phonons are in phase. The potential necessary to induce a lattice displacement, or deformation potential, is given by D_A. The electron-phonon interaction is also dependent on the material density, ρ, and the material speed of sound, v_s and the scattering rate is given by [33, 62]:

$$\begin{aligned} W_{\mathrm{if}}(k_{\mathrm{i}}) = {} & \frac{D_A^2 m^*}{\rho v_s (2\pi)^2 \hbar^2} \left(N_0 + \frac{1}{2} \mp \frac{1}{2}\right) \int_0^{\infty} \int_0^{2\pi} \left(G_{\mathrm{if}}(K_z)\right)^2 \\ & \times \left(\frac{\Theta(\alpha_1)\alpha_1 \sqrt{\alpha_1^2 + K_z^2} + \Theta(\alpha_2)\alpha_2 \sqrt{\alpha_2^2 + K_z^2}}{\alpha_1 - \alpha_2} \right) \ \mathrm{d}\phi\ \mathrm{d}K_z \end{aligned} \tag{3.20}$$

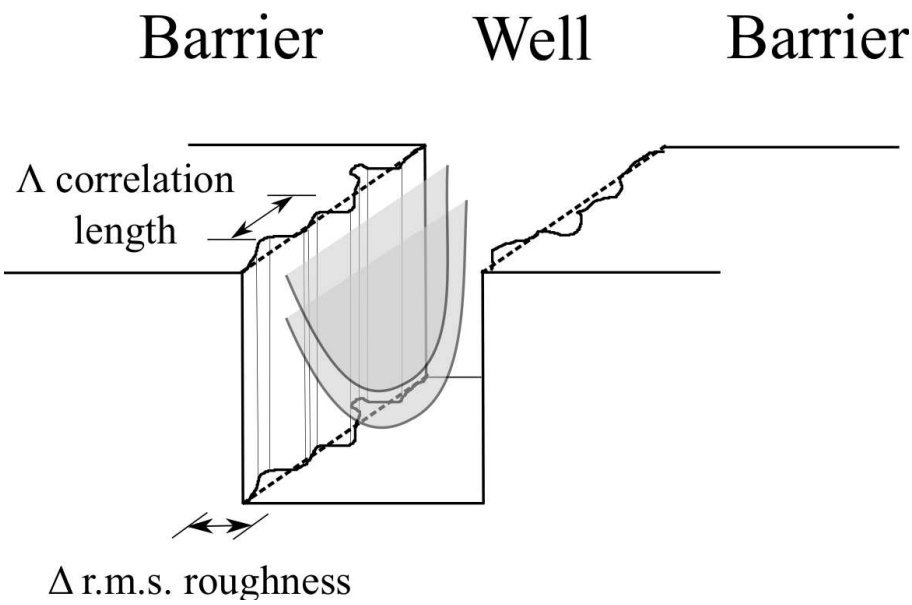

Figure 3.1: Schematic of interface roughness scattering where small fluctuations in the interface position cause a perturbing potential.

where

$$\alpha_{1,2} = -k_{\mathrm{i}} \cos\phi \pm \sqrt{k_{\mathrm{i}}^2 \cos^2\phi - \frac{2m^*\Delta E}{\hbar^2}} \tag{3.21}$$

Acoustic phonon scattering is typically slower than LO phonon scattering, and the absorption of phonons is much slower than that of emission. Elastic phonon scattering along with carrier–carrier scattering contributes to the thermalisation of subbands.

3.6 Interface roughness scattering

The fluctuations are usually assumed to have a Gaussian Fourier transform $\Delta_z(\boldsymbol{r})$ with height Δ and correlation length Λ as shown in figure 3.1 [63]. This fluctuation in the confinement potential causes a perturbation that scatters electrons. Typically models assume a step-like potential such as that in Ref. 64, however the model used

in the present work is given in Ref. 65. While diffuse interfaces are not investigated here, this model is capable of being applied to arbitrary interface profiles. The scattering rate between initial and final wavevectors caused by an interface, I, can be calculated as [65]:

$$W_{\mathrm{if}}(k_{\mathrm{i}}) = \frac{\pi m^*(\Delta\Lambda)^2}{\hbar^3}\beta(k_{\mathrm{i}})\sum_I \left(F_{\mathrm{if},I}\right)^2 \tag{3.22}$$

where

$$\beta(k_{\mathrm{i}}) = \mathrm{e}^{-(k_{\mathrm{i}}^2+k_{\mathrm{f}}^2)\Lambda^2/4} I_0\left(\frac{k_{\mathrm{i}}k_{\mathrm{f}}\Lambda^2}{2}\right)\Theta(k_{\mathrm{f}}^2) \tag{3.23}$$

where I_0 is the zeroth order Bessel function, and

$$F_{\mathrm{if},I} = \psi_f^*(z_I)V_0\psi_i(z_I) \tag{3.24}$$

The $F_{\mathrm{if},I}$ term in Eq. (3.22) intuitively explains that the greater the probability of electrons at the interface, the larger the scattering rate becomes. Additionally, the scattering rate will increase with the square of the height of the initial barrier, V_0, and it is important that this limitation is accounted for in devices with high alloy barriers or material systems with a high offset like $\mathrm{Al}_x\mathrm{Ga}_{1-x}\mathrm{N}/\mathrm{GaN}$. The roughness parameters Δ and Λ are typically treated as tuning parameters to match the current density and gain observed in an experimental device. It is difficult to predict the interface roughness parameters of a device before growing and this introduces an element of uncertainty in modelling. In the present work, initial values of $\Delta = 2.8\,\text{Å}$ and $\Lambda = 100\,\text{Å}$ were used (unless otherwise stated) for device optimisation as they are similar to those used by other modelling groups [66] and are shown to give good agreement in Chapter 4.

3.7 Alloy disorder scattering

In Chapter 2 the high barrier material (either AlGaAs or AlGaN) was shown to confine electrons in the conduction band. The envelope function used to approximate

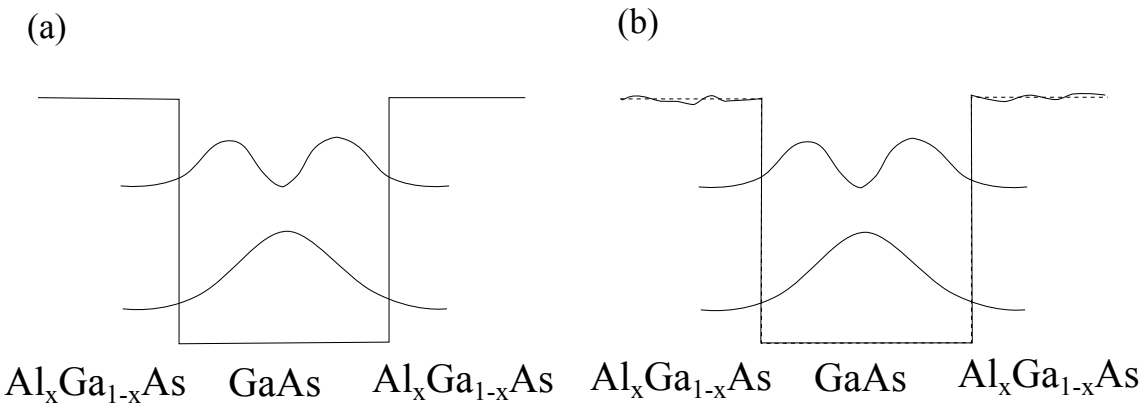

Figure 3.2: (a) The bandstructure of a quantum well assuming no alloy disorder. (b) The random placement of dopant atoms introduces a random disorder which perturbs electrons.

the crystal lattice typically gives good agreement for the electron energy levels. However, the Al atoms randomly replace the Ga atom sites in the barrier material and also introduce a random barrier potential that perturbs the electrons as seen in figure 3.2. The scattering rate due to alloy disorder can be shown to be [34, 64]:

$$W_{\mathrm{if}}(k_{\mathrm{i}}) = \frac{m^*\Omega\Delta V_{\mathrm{ad}}^2}{\hbar^3}\Theta\left(k_{\mathrm{f}}^2\right)\int |\psi_{\mathrm{f}}(z)|^2 x(z)[1-x(z)]|\psi_{\mathrm{i}}(z)|^2 \mathrm{d}z \tag{3.25}$$

where x is the barrier alloy content, $\Omega = a^3/4$, and ΔV_{ad} is the offset of barrier and well materials. The scattering rate due to alloy disorder is mainly dependent on the overlap of the electron wavefunctions with the barrier material, and the alloy content. Since the Ga $\rightarrow$ Al substitution is completely random, the probability of scattering occurring increases from 0 with low Al content, peaking at x=50 % and decreasing to zero with AlAs or AlN barriers.

3.8 Ionised impurity scattering

In QCLs and other intersubband devices, the electrons confined and involved in optoelectronic properties originate from dopant donor atoms. As electrons become ionized and free of their initial atoms, the remaining atom has an uncompensated charge. While the many-body effect of the ionized dopants are included via the Schrödinger-Poisson equation, electrons are also scattered by interacting with the positive atomic charge. The perturbation Hamiltonian due to one such ionised atom is given by [34]:

$$\tilde{\mathcal{H}}_{\text{imp}}(\boldsymbol{r}-\boldsymbol{r_0}, z-z_0) = -\frac{e^2}{4\pi\epsilon\sqrt{|\boldsymbol{r}-\boldsymbol{r_0}|^2+(z-z_0)^2}}, \tag{3.26}$$

where $(z, \boldsymbol{r})$ and $(z_0, \boldsymbol{r_0})$ are the confined carrier and impurity positions respectively. Substituting this into Eq. (3.3), the scattering rate due to the ionised doping profile can be calculated as [34, 64]:

$$W_{\text{if}}(k_{\text{i}}) = \frac{m^* e^4}{4\pi\hbar^3\epsilon^2}\Theta\left(k_{\text{f}}^2\right)\int_0^{\pi}\frac{J_{\text{if}}(q)}{q^2}\,\mathrm{d}\theta \tag{3.27}$$

where

$$J_{\text{if}}(q) = \int d(z_0)\left|I(q,z_0)\right|^2\,\mathrm{d}z_0 \tag{3.28}$$

is the scattering matrix element. The integral of the initial and final wavefunctions with the doping profile is given by [34]:

$$I(q,z_0) = \int \psi_{\text{f}}^*(z)\psi_{\text{i}}(z)\;\mathrm{e}^{-q|z-z_0|}\,\mathrm{d}z \tag{3.29}$$

and the scattering wavevector $\mathbf{q} = k_{\text{i}} - k_{\mathbf{f}}$. Ionised impurity scattering is also a polar interaction like LO-phonon scattering and therefore is also screened by other local electrons. Impurity scattering is commonly screened with the Thomas-Fermi inverse scattering length (Eq. (3.17)) by substituting the scattering vector as:

$$q \to q + \frac{m^* e^2}{2\pi\epsilon\hbar^2} \tag{3.30}$$

which is denoted q_{TF}. While it may seem counter intuitive that this screening correction is independent of the sheet density, it is noted that the carrier sheet density and the doping volume density are linear. Ionised impurity scattering is relatively insensitive to increasing temperature, and highly dependent on the overlap of initial and final wavefunctions. For this reason ionised impurity scattering can be employed to induce scattering between states if desired, and doping is usually kept spatially away from optical transitions due to its effect on the optical linewidth.

3.9 Electron–electron scattering

Typical subband electron densities are on the order of $1 \times 10^{10}\,\mathrm{cm}^{-2}$ in THz QCLs [8] and these electrons interact with each other via electrostatic repulsion. The Hamiltonian for two interacting electrons is given by [33]:

$$\tilde{\mathcal{H}} = \frac{e^2}{4\pi\epsilon r} \tag{3.31}$$

where ϵ is the permittivity of the material and r is the distance between the electrons. While previous scattering mechanisms described one electron interacting with a perturbation and ending up in either the same, or a different subband, electron–electron scattering involves two electrons. The initial and final positions of both electrons must be considered for each interaction. The initial and final scattering rates for the first and second electrons are given by i, j and k, g respectively.

The scattering rate is calculated as [33, 67]:

$$W_{\mathrm{ijfg}}(k_{\mathrm{i}}) = \frac{m^* e^4}{4\pi\hbar^3(4\pi\epsilon)^2} \int\int_0^{2\pi}\int_0^{2\pi} \frac{|A_{\mathrm{ijfg}}(q_{xy})|^2}{q_{xy}^2}\, P_{\mathrm{j}}(\mathbf{k}_{\mathrm{j}})\ \mathrm{d}\theta\ \mathrm{d}\alpha\ k_{\mathrm{j}}\ \mathrm{d}k_{\mathrm{j}} \tag{3.32}$$

where

$$A_{\mathrm{ijfg}} = \int_{-\infty}^{+\infty}\int_{-\infty}^{+\infty} \psi_{\mathrm{i}}(z)\psi_{\mathrm{j}}(z')\psi_{\mathrm{f}}^*(z)\psi_{\mathrm{g}}^*(z')\ \mathrm{e}^{-q_{xy}|z-z'|}\ \mathrm{d}z'\ \mathrm{d}z, \tag{3.33}$$

$$(2q_{xy})^2 = 2k_{\mathrm{ij}}^2 + \Delta k_0^2 - 2k_{\mathrm{ij}}\sqrt{k_{\mathrm{ij}}^2 + \Delta k_0^2}\cos\theta, \tag{3.34}$$

$$k_{\mathrm{ij}}^2 = k_{\mathrm{i}}^2 + k_{\mathrm{j}}^2 - 2k_{\mathrm{i}}k_{\mathrm{j}}\cos\alpha. \tag{3.35}$$

The probability of scattering is reduced when the screening effect of other electrons is accounted for. Screening can be introduced in a simple approach by altering the dielectric constant (in Eq. 3.32) to be dependent on wave vector as in the work of Smet *et al.* [67]. It is shown in Refs. 33 and 67 that the dielectric constant becomes $\epsilon = \epsilon_r\epsilon_0\epsilon_{\mathrm{sc}}$, where ϵ_{sc} is the screening contribution given by:

$$\epsilon_{\mathrm{sc}} = 1 + \frac{2\pi e^2}{(4\pi\epsilon)q_{xy}}\Pi_{\mathrm{ii}}(q_{xy}, T)A_{\mathrm{iiii}}(q_{xy}) \tag{3.36}$$

The polarization factor for subband i at absolute zero temperature is given by:

$$\Pi_{\mathrm{ii}}(q_{xy}, T=0) = \frac{m^*}{\pi\hbar^2}\left[1 - \Theta(q_{xy} - 2k_{\mathrm{F}})\sqrt{1 - \left(\frac{2k_{\mathrm{F}}}{q_{xy}}\right)^2}\right] \tag{3.37}$$

where the Fermi wavevector defined at $T = 0$ is:

$$k_{\mathrm{F}} = \sqrt{2\pi N_{\mathrm{i}}} \tag{3.38}$$

Eq. 3.37 can be generalised to be applicable at any temperature following the approach in Ref. [68]:

$$\Pi_{\mathrm{ii}}(q_{xy}, T) = \int_0^\infty \frac{\Pi_{\mathrm{ii}}(q_{xy}, T=0)}{4kT\cosh^2\left((E_{\mathrm{F}} - E)/(2kT)\right)}\ \mathrm{d}E \tag{3.39}$$

where E_{F} is the subband quasi-Fermi energy. Screening effects become larger as the subband carrier density increases.

Electron–electron scattering is an elastic process and therefore intrasubband events generally are much faster than intersubband scattering unless the energy levels are close together. The fast intrasubband scattering mechanism is assumed to be important in the thermalisation of electron distributions in subbands [41] however it is occasionally neglected in the present work due to its computational burden.

3.10 Conclusion

In this chapter a review of the calculations necessary for electron scattering was presented. Both elastic and inelastic processes contribute to the optoelectronic properties of devices. The semi-classical scattering rates were shown to depend on material parameters, design and lattice temperatures. These calculations are the basis upon which the following investigation on optical and electronic properties of $Al_xGa_{1-x}N/GaN$ and $Al_xGa_{1-x}As/GaAs$ intersubband devices are based.

Chapter 4

Coherent modelling of QCLs

In this chapter the principles of density matrix (DM) modelling of QCLs are presented. These use the semi-classical scattering rates presented in Chapter 3 along with a "tight-binding" Hamiltonian for the QCL to account for time taken to tunnel through the injector barrier in QCL structures. The DM approach presented is capable of modelling QCL structures with an arbitrary number of states per period since transport between all states is included across the tunnelling barrier, in contrast to typical DM approaches which include only a few coherences. While this model has been presented previously with SiGe QCL structures, it has not been compared to other approaches or experimental results for experimentally realised $Al_xGa_{1-x}As$/GaAs QCLs. It is shown that predicted current densities and emission power of a typical QCL structure agree well with state-of-the-art QCL devices recently demonstrated. Additionally, the decreasing performance of THz QCLs is analysed with the model which faithfully replicates the varying threshold current and emission power observed in experimental devices with varying temperature.

4.1 Motivation for coherent transport modelling

Initial models for the transport in QCLs [7, 69, 70] included only incoherent scattering between states in the QCL structure. Conventionally, wavefunctions of states were calculated with several periods of the QCL bandstructure. Under certain conditions such as an applied field which causes a pair of states to align, wavefunctions are allowed to spread over the entire structure. It was shown in Chapter 3 that the scattering rate is highly sensitive to overlap of the wavefunctions; since scattering transport is assumed to be an instantaneous event, the rate equation approach allows carriers to be transported instantly between spatially separated points. This leads to unphysical resonances in populations, gain and most significantly, current density. In reality, carriers propagate over time, and it takes some finite time for carriers to tunnel across barriers in the QCL structure. Figure 4.1(a) illustrates how states calculated with an extended basis can form a symmetric doublet with splitting $\Delta E = 2\hbar\Omega$ when aligned. Since the scattering rate and therefore rate-equation current is dependent on the overlap of states, the current will be independent of barrier thickness. In cases such as terahertz QCLs where energy states are closer together, current is often over estimated when state alignments occur. In reality, thick barriers can trap carriers for an appreciable time and modify their transport through the device. It is more realistic to assume that incoherent scattering only occurs between the quasi-steady states within a single module, and to consider transport between the modules as a coherent tunnelling process.

4.1.1 Density matrices

A number of methods exist for modelling coherent quantum transport in semiconductor heterostructures including the density matrix and non-equilibrium Greens function (NEGF) [71] approaches. The density matrix approach refers to the use

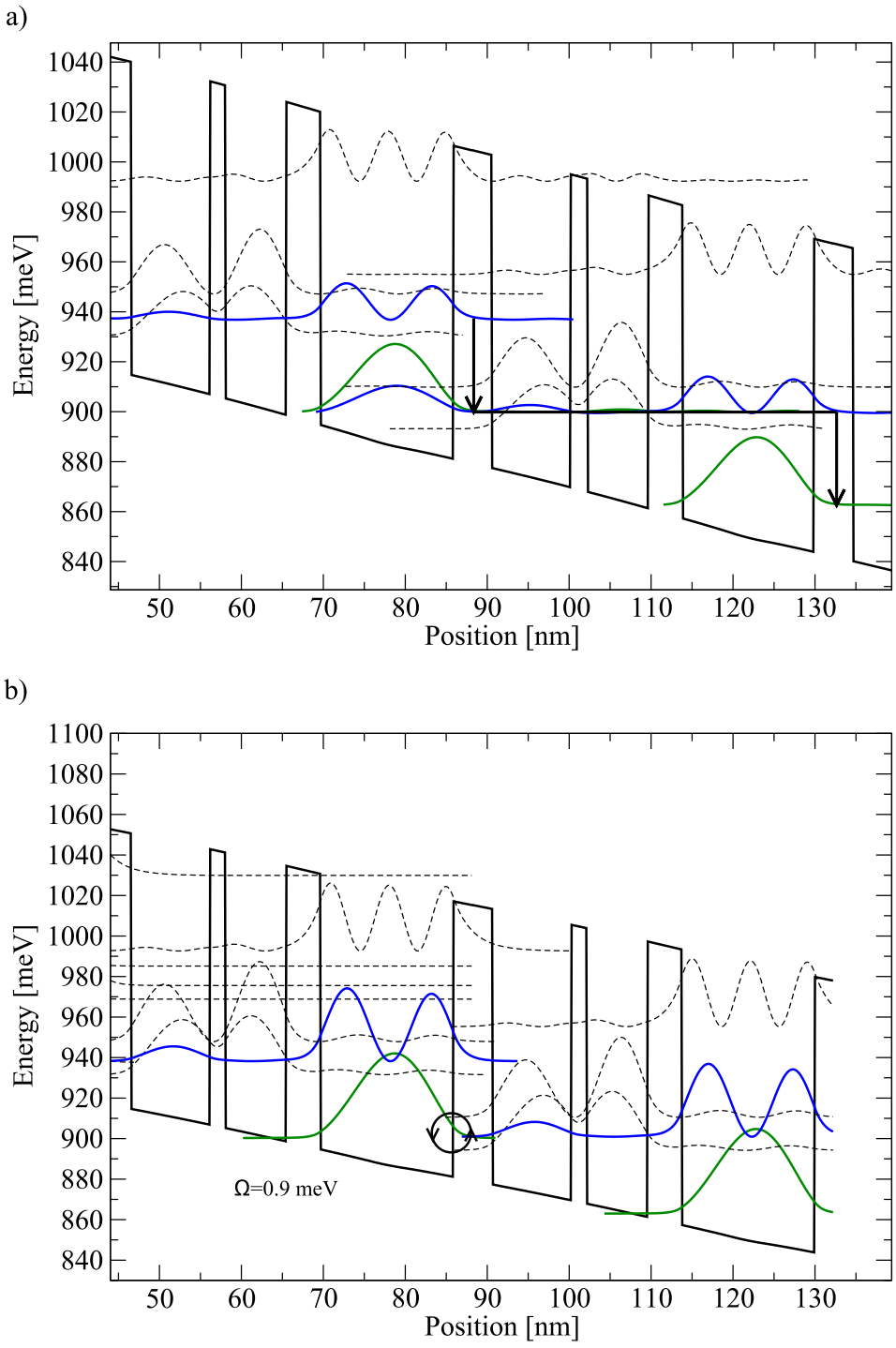

Figure 4.1: Bandstructure and wavefunction plot of the three-well THz QCL in Ref. 8 at F=8.5 kV/cm. (a) Extended wavefunctions allow carriers to be transported almost instantaneously through the device via the path shown with an arrow. (b) Wavefunctions calculated with a tight-binding Hamiltonian have a residual coupling strength that accounts for tunnelling time.

of a matrix to contain all possible information about a quantum mechanical system in a compact manner. The following descriptions of density matrix properties are very general and are based on more complete treatments in Ref. [72]. This density matrix approach can deal with two types of uncertainty: the probabilistic interpretation of the wave function described in Chapter 2, and the uncertainty regarding which state the quantum system is in at a given time. The latter can be represented by treating the system as a statistical ensemble of carriers; the state of the system can be represented at any given time as a weighted summation over a number of basis states $|\phi_i\rangle$. The state of the system $|\psi(t)\rangle$ at any given time is then:

$$|\psi(t)\rangle = \sum_i c_i(t)\,|\phi_i\rangle \tag{4.1}$$

where c_i is the complex amplitude coefficient (or weighting) of the i^{th} state at time t. The squared amplitudes of each basis state must add to one at any given time such that:

$$\langle\psi(t)|\psi(t)\rangle = \sum_j c_j^*(t)c_j(t) = \sum_j |c_j(t)|^2 = 1. \tag{4.2}$$

The expectation value (i.e. average) of an observable property A is obtained by using the operator $\mathcal{A}$:

$$\langle A\rangle = \langle\psi|\mathcal{A}|\psi\rangle \tag{4.3}$$

If the state is resolved into its set of basis states, it is more convenient to consider the operator in its matrix form, with its elements defined as:

$$A_{ij} = \langle\phi_i|\mathcal{A}|\phi_j\rangle \tag{4.4}$$

Substituting Eq. (4.1) into Eq. (4.3) gives:

$$\begin{aligned}\langle A(t)\rangle &= \sum_i c_i^*(t)\langle\phi_i|\mathcal{A}\sum_j c_j(t)|\psi_j\rangle \\ &= \sum_i\sum_j c_i^*(t)c_j(t)\langle\phi_i|\mathcal{A}|\phi_j\rangle\end{aligned} \tag{4.5}$$

$$= \sum_i \sum_j c_i^*(t) c_j(t) A_{ij}$$

Therefore, it is possible to determine the expectation value of an observable at any given time, provided that the weightings of each state are known at that time. By substituting $c_i = \langle \phi_i | \psi \rangle$, the expectation value in Eq. (4.6) is given by:

$$\langle A(t) \rangle = \sum_i \sum_j \langle \phi_j | \psi(t) \rangle \langle \psi(t) | \phi_i \rangle A_{ij} \tag{4.6}$$

This expression may be simplified by introducing the density operator:

$$\rho(t) = |\psi(t)\rangle\langle\psi(t)| \tag{4.7}$$

which describes the probability distribution of the quantum system.

The diagonal elements of the density matrix, ρ_{ii}, represent the probability that a carrier will be found in state i and must satisfy the density conservation law $\mathrm{Tr}(\rho) = 1$. Off-diagonal terms, ρ_{ij}, represent the coherence (or polarisation) between the states:

$$\rho_{ij}(t) = \langle \phi_i | \rho(t) | \phi_j \rangle = c_i(t) c_j^*(t) \tag{4.8}$$

i.e. the coherent superpositions. In a system where carriers can be in several states (such as the discrete energy levels in a QCL), the density matrix will describe the populations of the states as well as the interaction between them.

Substituting the density operator into Eq. (4.6) gives:

$$\langle A(t) \rangle = \sum_i \sum_j \langle \phi_j | \rho(t) | \phi_i \rangle A_{ij} = \sum_i \sum_j \rho_{ji}(t) A_{ij} \tag{4.9}$$

which can be simplified to:

$$\langle A(t) \rangle = \sum_j \left[\rho(t) \mathsf{A} \right]_{jj} = \mathrm{Tr} \left[\rho(t) \mathsf{A} \right] \tag{4.10}$$

i.e. the expectation value is the trace (i.e. sum of diagonal elements) of the density matrix multiplied by the matrix operator for the observable.

4.1.2 Time evolution of the density matrix

The statistical distribution of the ensemble of particles will evolve over time: either as a response to an external input such as the applied bias field, cavity light field or intrinsic oscillations of the system, e.g. Rabi oscillations. Substituting the density operator (Eq. 4.7) into the Schrödinger equation gives:

$$\begin{aligned}\frac{\mathrm{d}}{\mathrm{d}t}\rho(t) &= \frac{\partial}{\partial t}\left[|\psi(t)\rangle\langle\psi(t)|\right] \\ &= \frac{i}{\hbar}\left(\mathcal{H}|\psi(t)\rangle\langle\psi(t)|\right) - \frac{i}{\hbar}\left(|\psi(t)\rangle\langle\psi(t)|\mathcal{H}\right) \\ &= \frac{i}{\hbar}\left[\mathcal{H}, \rho(t)\right]\end{aligned} \tag{4.11}$$

which is the von Neumann/Liouville equation and describes the time evolution of the state with the unperturbed Hamiltonian. Therefore, the values of the density matrix elements can be found at any given time, and Eq. (4.10) can be solved to find the expectation value of any observable property.

4.2 Density matrix modelling of terahertz QCLs

Several density matrix formalisms have been applied to QCLs such as those in Refs. [73–75]. These typically assume a 'tight-binding' approach where wave functions for a period are calculated with the structure embedded in barrier material as shown in figure 4.1(b). States in neighbouring periods then interact with the residual coupling strength, Ω, that corresponds to Rabi oscillations across the barrier.

In the present work, the approach in Ref. 73 is followed and built upon, which is a general model that does not need *a priori* knowledge of the states present in the system. As the QCL is periodic, the density matrix calculation only needs to consider the terms for a single period of the structure and the coherence terms

between periods. The density matrix takes the form [73]:

$$\rho = \begin{pmatrix} \rho_{\mathrm{CC}} & \rho_{\mathrm{CU}} & \rho_{\mathrm{CD}} \\ \rho_{\mathrm{UC}} & \rho_{\mathrm{UU}} & \rho_{\mathrm{UD}} \\ \rho_{\mathrm{DC}} & \rho_{\mathrm{DU}} & \rho_{\mathrm{DD}} \end{pmatrix} \tag{4.12}$$

where CC, UU and DD refer to the central, upstream and downstream periods of three periods of the structure under consideration. Each of these blocks is itself an $N \times N$ matrix (where N is the number of subbands in each period), which represents the coherences between all pairs of states within the same period (e.g. CC, UU etc.) or in two different periods (e.g., CU, UC, etc).

The calculation can be simplified by considering the translational invariance of states in a QCL. As such, the coherences between equivalent pairs of states within any period is identical and therefore $\rho_{\mathrm{CC}} = \rho_{\mathrm{UU}} = \rho_{\mathrm{DD}}$ [73]. The same applies for equivalent interactions between any two periods, and so $\rho_{\mathrm{CD}} = \rho_{\mathrm{UC}}$ and $\rho_{\mathrm{DC}} = \rho_{\mathrm{CU}}$. Complexity is reduced further by noting that the upstream and downstream periods are very widely separated, and as such the direct interactions between these pairs of states are extremely weak. Therefore, $\rho_{\mathrm{UD}} = \rho_{\mathrm{DU}} = 0$. The final density matrix then takes the form [73]:

$$\rho = \begin{pmatrix} \rho_{\mathrm{CC}} & \rho_{\mathrm{CU}} & \rho_{\mathrm{UC}} \\ \rho_{\mathrm{UC}} & \rho_{\mathrm{CC}} & 0 \\ \rho_{\mathrm{CU}} & 0 & \rho_{\mathrm{CC}} \end{pmatrix} \tag{4.13}$$

The Hamiltonian matrix for the system takes the form [73]:

$$\mathsf{H} = \begin{pmatrix} H_{\mathrm{CC}} & H_{\mathrm{CU}} & H_{\mathrm{UC}} \\ H_{\mathrm{UC}} & H_{\mathrm{UU}} & 0 \\ H_{\mathrm{CU}} & 0 & H_{\mathrm{DD}} \end{pmatrix} \tag{4.14}$$

with diagonal terms containing the state energies calculated using the tight-binding Hamiltonian and inter-period terms consisting of Rabi oscillation strengths calcu-

lated as [75]:

$$\hbar\Omega_{ij} \approx \langle i| \, \mathrm{H_{ext}} - \mathrm{H_{TB}} \, |j\rangle \tag{4.15}$$

where $\mathrm{H_{ext}}$ and $\mathrm{H_{TB}}$ refer to the Hamiltonians (potentials) of the extended structure and of the 'tight-binding' sections, respectively. To achieve tight-binding Hamiltonians, some amount of padding material (10 nm in the present work) is added either side of one period of the QCL to allow the wavefunctions to exponentially decay to zero. Barriers in nitride structures can have a positive field in the opposite direction to the external electric field; this causes the middle of the injection barrier to be at a lower energy than at the end of it. In these cases, the input file is set so that the periodic structure begins with a thin (1 Å) barrier and ends with the rest of the barrier width to calculate confinement correctly.

Note that as in the density matrix in Eq. (4.13), these off-diagonal blocks are identical between any two periods, and hence the substitutions $H_{\mathrm{UC}} = H_{\mathrm{CD}}$ and $H_{\mathrm{DC}} = H_{\mathrm{CU}}$ have been made. However, the diagonal (UU, DD, CC) blocks of the Hamiltonian matrix are different from each other, since the applied electric field shifts the states in each period downward in energy. Typically QCL simulations account for some interaction with the light field present in the cavity; this can be included in the density matrix Hamiltonian with off-diagonal intra-period terms given by [73]:

$$H_{ij} = z_{ij} A_0 \mathrm{e}^{i\omega t} \tag{4.16}$$

where z_{ij} is the dipole matrix element for the transition, A_0 is the strength of the incident light field and ω is the radiation frequency.

In the equation of motion given by Eq. (4.11), scattering and dephasing caused by interaction with perturbations such as those described in Chapter 3 will add extra relaxation terms to the diagonal and off-diagonal elements of the density matrix.

Equation (4.11) then becomes [73]:

$$\frac{\mathrm{d}\rho}{\mathrm{d}t} = -\frac{i}{\hbar}\left[H(t), \rho(t)\right] - \left(\frac{\rho}{\tau}\right)_{relax} \tag{4.17}$$

where the final term is the relaxation matrix that describes the damping of the system which can also symbolically be written as $\frac{\varrho}{\tau}$. The diagonal terms of this matrix describe the change in population over time caused by scattering between states, and are given by:

$$\left(\frac{\rho}{\tau}\right)_{ii} = -\frac{\rho_{ii}}{\tau_i} + \sum_{j \neq i} \frac{\rho_{jj}}{\tau_{ji}} \tag{4.18}$$

i.e. the difference between the density of carriers scattering into the state and those scattering out. The off-diagonal elements reflect that every scattering event involving either state i or j will affect the coherence of that state with every other state, and are given by:

$$\left(\frac{\rho}{\tau}\right)_{ij} = \frac{\rho_{ij}}{\tau_{\parallel,ij}} \tag{4.19}$$

where $\tau_{\parallel,ij}$ is the dephasing time. Several proposals have been made for their calculation and the present work uses a combination of the approaches described in Refs. 75 and 76:

$$\frac{1}{\tau_{\parallel,ij}} = \frac{1}{2\tau_i} + \frac{1}{2\tau_j} + \frac{1}{\tau_{ii}} + \frac{1}{\tau_{jj}} - \frac{2}{\sqrt{\tau_{ii}^{IFR}\tau_{jj}^{IFR}}} \tag{4.20}$$

where τ_{ii} is the intrasubband scattering lifetime (due to mechanisms other than IFR scattering) in state i, and τ_{ii}^{IFR} is the intrasubband scattering lifetime due to interface roughness in state i. Ref. 76 does not include the state lifetime contribution to dephasing, however the coherence between states also determines the gain linewidth (in addition to its effect on tunnelling processes). This is commonly accepted to be heavily influenced by the intersubband scattering lifetime [64, 77, 78]. A significant advantage of the extended density matrix approach described here is that it can be used to simulate devices with any number of states without prior knowledge of

the lasing states. It is therefore not reasonable to introduce a situation where the coherence of some states is calculated without intersubband scattering contributions.

Moreover, some existing models do not include the contribution of intrasubband scattering on the intersubband absorption/gain linewidth [78]. This approximation is based on correlations of the intrasubband scattering potentials affecting both states similarly [79]. The last term in Eq. 4.20 accounts for carriers experiencing scattering from correlated interface roughness so that dephasing overall is reduced for $i \neq j$, and is zero for $i = j$. This then allows other intrasubband scattering contributions to be included in the linewidth calculation similar to Refs. 64, 75, 77 and 80. Electron-electron scattering is typically included in QCL simulations which do not assume a subband electron temperature such as NEGF or Monte-Carlo modelling as subband thermalisation is required. However this scattering is neglected here due to its computational burden; this is not expected to affect results significantly since it is thought intrasubband electron–electron scattering does not contribute to linewidth broadening due to it being a second order effect [32, 81].

4.3 Electron temperature

The scattering rates described in Chapter 3 show how perturbations can cause inter- and intra- subband scattering. Intersubband scattering leads to the transfer of kinetic energy between subbands; the total energy of a subband can increase or decrease depending on an electron with kinetic energy $E_{k,i}$ scattering in or out of it respectively and this affects the subband electron temperature. By considering the transfer of only electrons for elastic processes, and electron and phonon energies for inelastic processes, the energy transfer rate to the lattice can be calculated as [34, 61]:

$$\frac{\mathrm{d}E_k}{\mathrm{d}t} = \sum_f \sum_i n_i E_{if} \overline{W}_{if}. \tag{4.21}$$

where i and f are all subbands that are summed over. For systems which have achieved a steady state condition, $\frac{\mathrm{d}E_k}{\mathrm{d}t} = 0$ must be obeyed to conserve energy. Since QCLs are non-equilibrium devices, the average scattering rates are strongly dependant on the electron temperature which describes their electron distribution. An electron temperature which gives this condition is therefore found iteratively as part of QCL simulations. In these simulations the electron temperature is assumed to be constant for all subbands; this is an approximation which has been shown to give good experimental agreement [82].

4.4 Current and gain

It is a desirable feature that QCL models include the effect of the cavity light field on the active region. Typical DM models use a rotating-wave approach (RWA) where each coherence is assumed to have only a single frequency harmonic corresponding to the cavity light frequency. Typically the steady-state coherences depend on whether the pair of states is optically active (i.e. their energy separation is close to the lasing frequency). The approach used in the present work instead uses a "non-RWA" formalism [73] where each density matrix element is assumed to have three harmonic terms such that:

$$\rho_{i,j} = \rho^{+}_{i,j}\exp(\mathrm{i}\omega_0 t) + \rho^{\mathrm{DC}}_{i,j} + \rho^{-}_{i,j}\exp(-\mathrm{i}\omega_0 t) \tag{4.22}$$

The steady state solution can be obtained by setting $\frac{\mathrm{d}\rho}{\mathrm{d}t} = 0$ for ρ^{DC} values and $\frac{\mathrm{d}\rho}{\mathrm{d}t} = -i\omega$ for ρ^{AC} values and subsequently solving with the known scattering rates to find the coherence values. The time-dependent behaviour of the QCL can also be calculated with standard time integration approaches to partial differential equations e.g. Runge–Kutta methods. However, this can be time consuming and it is typically the steady-state condition of the QCL that is of interest.

Physical quantities such as current density for the QCL can be extracted from the solved density matrix as $j = \mathrm{Tr}(\rho J)/2$, with the current matrix derived from the average drift velocity:

$$J = e\frac{i}{\hbar}\,[\mathrm{H,z}] \tag{4.23}$$

The gain of the QCL can also be extracted from J by considering the harmonic (AC) response of density matrix terms to a light field. The complex permittivity $\tilde{\epsilon}$ of the electron gas is calculated from:

$$\tilde{\epsilon} = \frac{j_{\mathrm{ac}}}{\frac{\mathrm{d}}{\mathrm{d}t}\left(A_0 \exp i\omega t\right)} \tag{4.24}$$

and the gain follows as $g = \omega \cdot \mathrm{Im}(\tilde{\epsilon})/3n_r c$ where n_r is the refractive index of the structure.

Improved agreement of QCL current densities can be achieved by considering that current in weakly bound states found with the "tight-binding" Hamiltonian are in fact continuum states [83]. Thus, the current density J can be separated into two components: the scattering and tunnelling current between states that are bound (j) and the drift current associated with the continuum electrons mobility. This is calculated as [83]:

$$J = |e|\left(j + n_{\mathrm{3D}}^{\mathrm{cont}}\mu_d|\mathbf{E}|\right) \tag{4.25}$$

where $n_{\mathrm{3D}}^{\mathrm{cont}}$ is the 3D density of electrons in the continuum, μ_d is the electron drift mobility (9400 and $400\,\mathrm{cm^2V^{-1}s^{-1}}$ for GaAs and GaN respectively) and $|\mathbf{E}|$ is the applied electric field. To obtain the separate current components the density matrix is calculated with as many states as required first, and then the Hamiltonian and density matrices are truncated so that they contain the elements only for the bound states. The bound current j is then found with Eq. (4.23) and the population of continuum states is taken from the original density matrix and substituted into Eq. (4.25).

4.5 Threshold gain and output power

For lasing to occur, stimulated emission must be induced in a cavity which contains the optical field known as a waveguide. These are typically processed ridges of the QCL active region which have metal deposited on either one, or both sides to confine the optical light field as a surface plasmon. The modal overlap Γ is the fraction of photons confined to the active region where gain occurs. For maximum stimulated emission and peak output powers this implies that Γ should be close to 1. Absorption of radiation by free carriers and other cavity losses are attributed to a waveguide loss α_w. Lasers are used to produce radiation and therefore another source of loss is emission through the cavity facets. The mirror losses α_m are typically assumed to be over the entire cavity round-trip and calculated as:

$$\alpha_m = \frac{1}{2L_w} \ln\left(\frac{1}{R_1 R_2}\right) \tag{4.26}$$

where R_1 and R_2 are the reflectivities of the facets that can be calculated in a simple approach as:

$$R_1 = R_2 = \left(\frac{n-1}{n+1}\right)^2 \tag{4.27}$$

where n is the cavity refractive index for a bare facet and air on the other side. The sum of waveguide and mirror losses are used with the modal overlap to find the threshold gain. This is the minimum gain required for lasing:

$$G_{th} = \frac{\alpha_w + \alpha_m}{\Gamma} \tag{4.28}$$

Typical GaAs waveguide losses are 20–30 cm^{-1} for single metal waveguides [7] and 10–20 cm^{-1} for double metal [8]. Low values of losses (15 cm^{-1} for a single metal waveguide) are also predicted for GaN THz QCLs [15].

At applied biases where a population inversion is present, spontaneous emission of photons will lead to cascading stimulated emission. The cavity field strength will increase until the point where stimulated emission reduces the population inversion

until gain is equal to the cavity loss. Total emitted power P from one facet is then calculated as:

$$P = \frac{c\epsilon_0 nWH}{2}|A_0|^2 \tag{4.29}$$

where W and H are the width and the height of the QCL ridge respectively.

4.6 Simulation procedure

Figure 4.2 shows the simulation procedure in its entirety. Applied bias, lattice temperature and cavity loss are input to the model; these are then used to set up the device bandstructure (according to Sections 2.1 and 2.2) and make an initial guess for the electron temperature. The Schrödinger-Poisson loop iteratively finds the effect of the charge distribution (Section 2.3) on the wavefunctions. Scattering rates (Chapter 3) are then calculated for the transport between these states. After convergence of this loop, a new T_E is chosen depending on whether energy is being given or taken from the lattice (Section 4.3). After convergence of this loop, a steady-state solution of the QCL structure is obtained. The gain and current density are both calculated by the density matrix formalism (Section 4.4) and stored. For a simulation where the QCL is "on" the light field intensity is varied iteratively until peak gain is equal to the input losses (Section 4.5). The presence of the light intensity iteration outside of the Schrödinger-Poisson and electron temperature loops is justified by the small effect of stimulated emission on the spatial charge distribution. Additionally, this improves stability and simulation time required.

4.7 Simulation of a resonant phonon QCL

The first demonstration of a QCL using resonant-phonon depopulation was in 2003 by Williams *et al.* [84] which operated in pulsed mode up to heat-sink tempera-

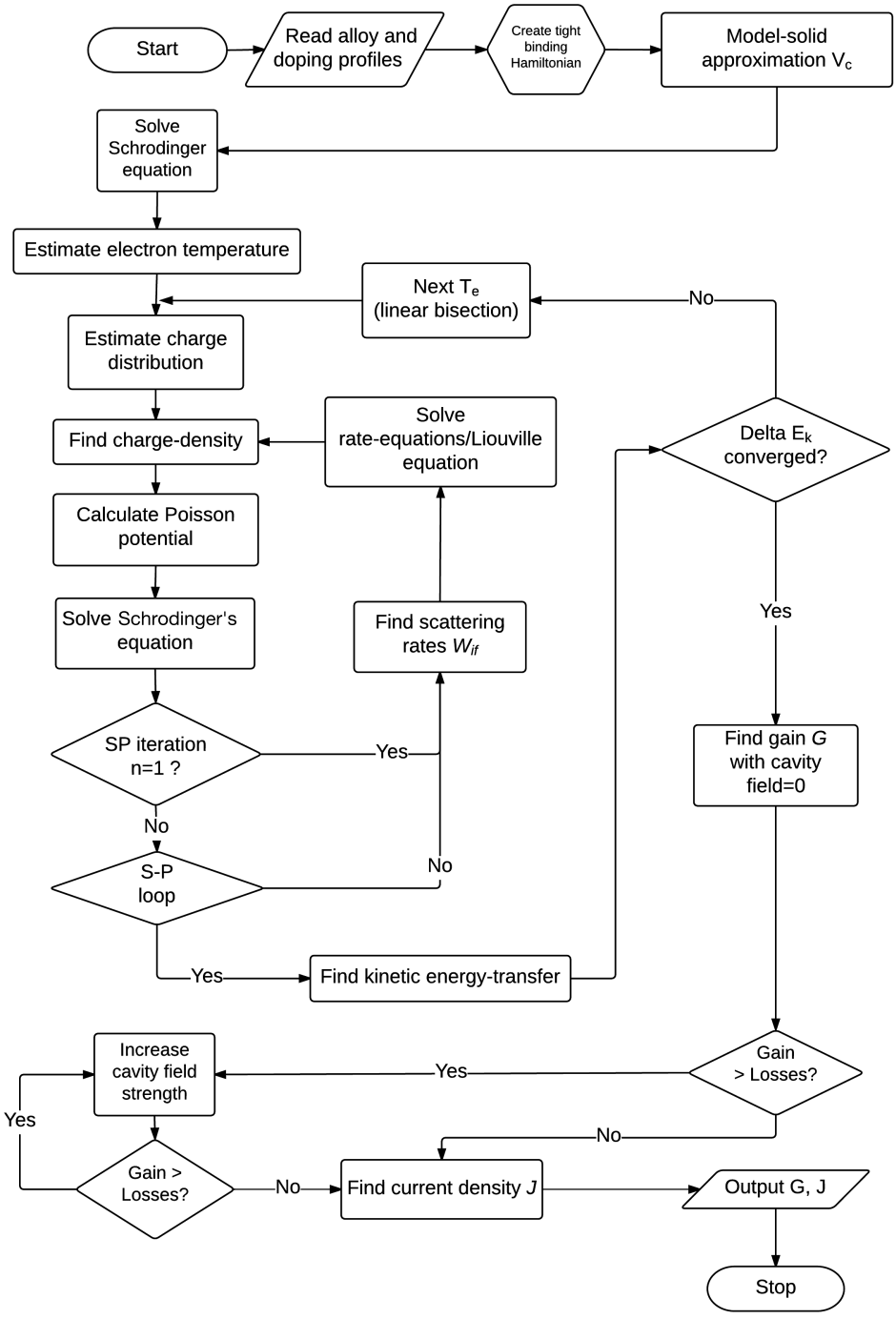

Figure 4.2: Flowchart for a fully self-consistent density matrix simulation of a QCL.

tures of 65 K. Subsequent iterations of this design [85] have increased the operating temperature to the current record of 200 K at 3.22 THz. The bandstructure of this device (herein referred to as the reference device) is shown in figure 4.3. Electrons are injected from state 1' in the upstream period to the ULL (state 4)[1] via selective tunnelling across the injection barrier and then emit a photon, dropping to the LLL (state 2). This LLL is coupled with the first excited state of the wide well (the extractor) which lies approximately 36 meV above the injector state allowing fast depopulation via LO phonon scattering. This structure was chosen for comparative modelling due to its potential for further improvements of its operating temperature by design optimisation. IFR values of $\Delta = 2.8$ Å and $\Lambda = 100$ Å were used for the simulations in this chapter [66, 86].

Figure 4.4 shows the calculated current and gain versus applied field for the structure at temperatures of 50, 100 and 200 K with the density matrix approach with the QCL in an "off" state. It can be seen that increasing temperature causes an increase in current density as electron distributions and LO phonon scattering increase. Gain decreases with increasing temperature due to both the population inversion decreasing and increasing broadening of the gain. Figure 4.5 shows the peak gain value as a function of applied field and frequency at 50 K. The frequency sweep is completed for the range of 2–4 THz where most QCL designs operate. It can be seen that increasing the applied field from 5 kV/cm to 12.2 kV/cm causes the structure to change from an absorption regime to providing a peak gain value of 55 cm^{-1} at 3.2 THz in good agreement with the results presented in Ref. 8.

The effect of changing lattice temperature on the electron temperature is shown in figure 4.6(a). This shows that the T_e that provides kinetic energy balance for the system has two distinct regions. Above ∼70 K the electron temperature increases linearly with lattice temperature. Below this value the electron temperature

[1]States in the upstream period are denoted n'.

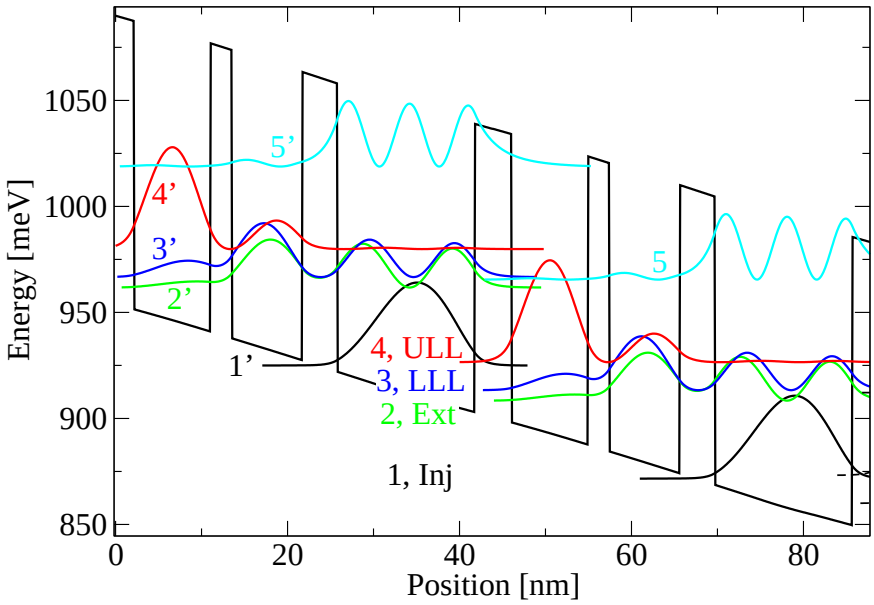

Figure 4.3: Bandstructure and wavefunction plot for the current high temperature record structure demonstrated in Ref. [8]. ULL, upper lasing level; LLL, lower lasing level; Ext, extractor; Inj, injector.

is relatively insensitive to changing lattice temperature. This is due both to elastic scattering at low lattice temperatures remaining small at low temperatures and an increasing contribution from LO-phonon scattering at higher temperatures. Figure 4.6(b) shows the effect of the changing lattice temperature on the total scattering rate and LO phonon scattering rate for the $4 \rightarrow 3$ and $2 \rightarrow 3$ transitions present in the 4-level laser system (i.e level 4 is the ULL, 3 is the LLL, and 2 is the collector/extractor state). This shows that the contributions from other scattering mechanisms for $4 \rightarrow 3$ remain relatively constant and it is scattering due to LO phonon emission that increases non-radiative transfer between these states, decreasing the population inversion. Increasing the lattice temperature also increases the

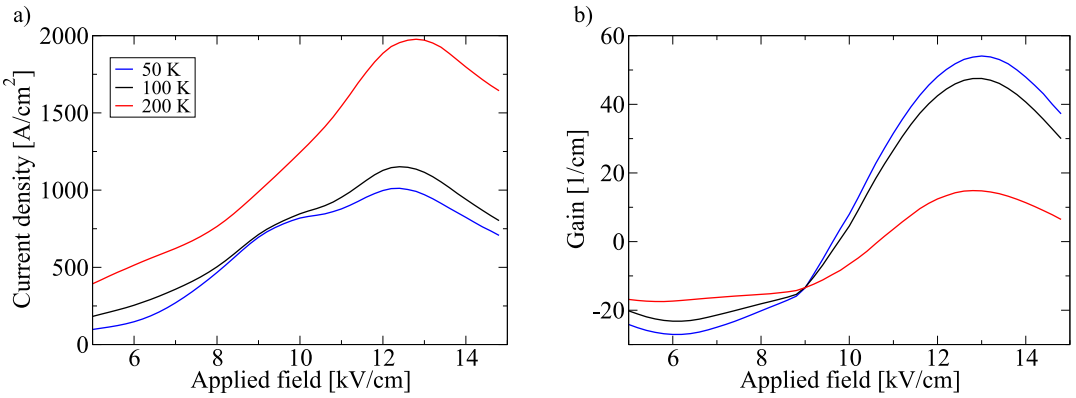

Figure 4.4: Calculated current and gain at different temperatures for the 200 K record structure. With increasing temperature current density increases and peak gain of the active region decreases.

scattering from the extractor states into the LLL in a process known as "back-filling" which further reduces the population inversion. These processes are illustrated in figure 4.7.

Figure 4.8 shows the effect of calculating the current density with and without

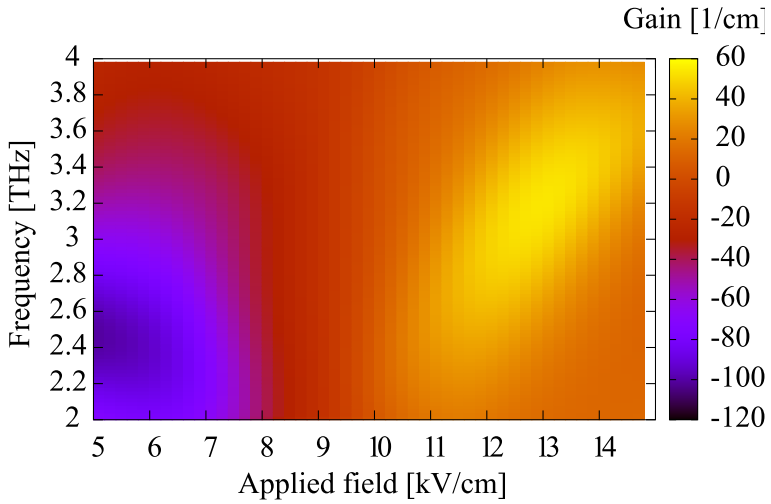

Figure 4.5: Unclamped spectral gain versus applied field calculated at 50 K.

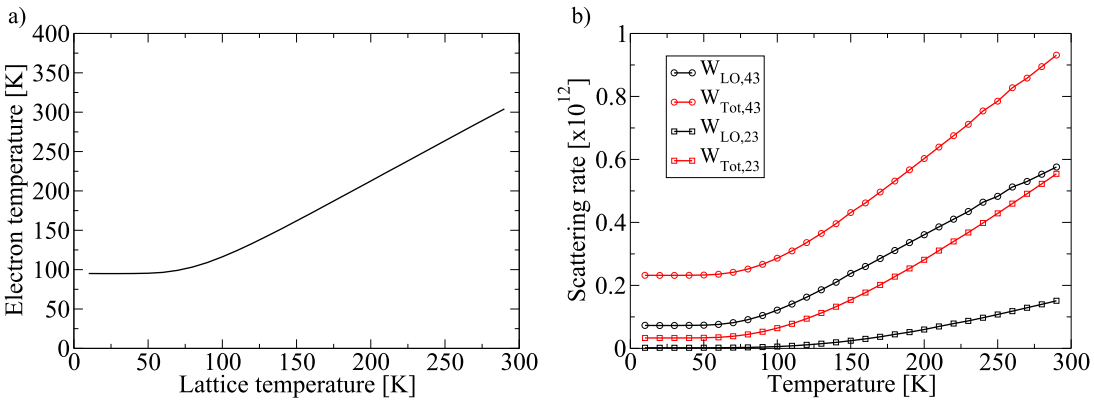

Figure 4.6: (a) Effect of increasing lattice temperature on electron temperature for the device held at 12.2 kV/cm. (b) Scattering rate between specified subbands versus lattice temperature.

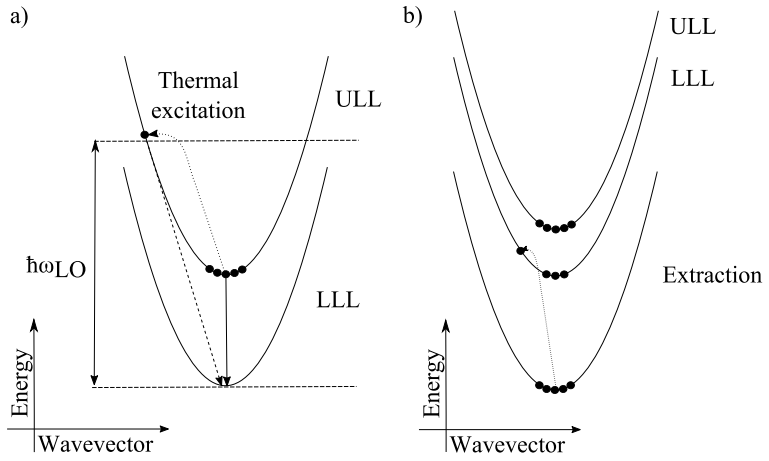

Figure 4.7: (a) Non-radiative emission via LO-phonon scattering increases with temperature as electrons gain enough thermal energy to emit a phonon, reducing population inversion. (b) Thermal backfilling occurs as the lower lasing level is repopulated with carriers that gain thermal energy in extraction states also reducing the population inversion.

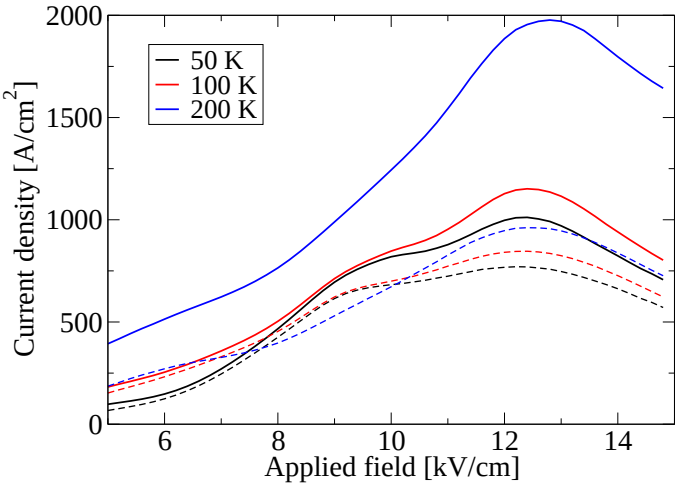

Figure 4.8: As calculated DM current (dashed) and current calculated with the drift mobility model for continuum states described in Section 4.4.

the contribution of continuum leakage current. Simulations for the leakage current assume that states 1–4 are bound while the population of state 5 (light blue in figure 4.3) is a continuum state. It can be seen that this improves the agreement of the magnitude of the current density: at 11 kV/cm the standard DM current is $\sim$700 A/cm^2 while with leakage included this is $\sim$1000 A/cm^2, in line with the experimental results in Ref. 8. It is noted that the inclusion of further states should converge to a stable current density value; however this is not found here. This is attributed to the excessive overlap of wavefunctions lying above the "tight-binding" conduction band edge with states in the neighbouring period. These states then typically lie above the barrier material intended to isolate the bound wavefunctions and are confined by the hard-wall conditions of the Schrödinger solver. Coupling strengths are overestimated due to this, and give unphysical population densities for continuum states which are not quasi-bound, despite their detuning from confined states. Fortunately, this is justified for the range of fields applied here since state 5

is the main parasitic state for tunnelling and scattering processes.

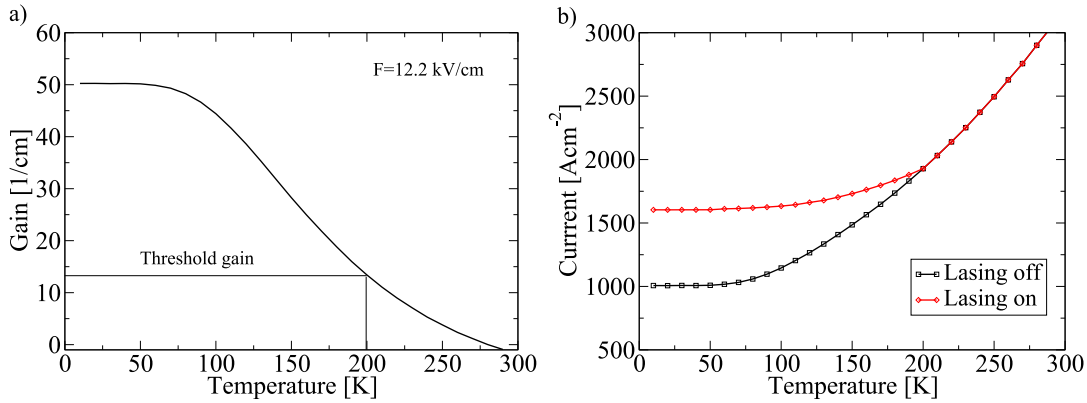

Figure 4.9: (a) Peak gain versus lattice temperature for the record 200 K QCL structure. (b) Current density versus lattice temperature for the same structure in both "on and "off" states.

Figure 4.9 shows the effect of the changing lattice and electron temperatures on the calculated gain and current. In figure 4.9(a) it can be seen that the gain decreases from 50 cm^{-1} at 10 K to 13.5 cm^{-1} at 200 K. This value is in reasonable agreement with the value of 19.6 cm found by Monte-Carlo simulations in Ref. 8 however, the DM model is not susceptible to unphysical spikes due to hybridisation. The current density at 12.2 kV/cm is predicted to increase with increasing temperature which is also found experimentally. Figure 4.9(b) also shows the effect of including the photon driven transport when the QCL is "on". In simulations which include the cavity light field interaction, the field intensity is increased until gain is clamped to the losses. At low temperatures the unsaturated gain is much larger than losses at this applied field, and a large light field is needed for the gain to be saturated. This results in a much larger current since electrons undergo stimulated emission and are moved coherently from the ULL to the LLL. At higher temperatures the excess gain decreases and the on and off currents converge when the laser turns off at 200 K

(simulations done with a fitted loss value of 13.5 cm^{-1}).

The calculated power and applied field versus current density are shown in figure 4.10. Voltage characteristics, output powers, and threshold current densities agree well with those measured experimentally in Ref. 8. For example, at 10 K a threshold current of 980 $\mathrm{A/cm}^2$ is predicted by the model and 1000 $\mathrm{A/cm}^2$ is measured experimentally. Above 100 K the discrepancy between these values increases and is attributed to experimental phenomenon such as non-linear contact drops and changing cavity losses. The unusual form of the light-current (L–I) curve is explained by the NDR predicted by the DM model where the ULL is moving out of alignment but lasing still occurs. This causes the L–I to fall back on itself with an unphysical appearance. This is not observed experimentally since the QCLs are driven by a current source. With a drive current the QCL adapts a bias point where the tunnelling, intersubband scattering and photon driven transport yield the current density supplied to the device. In structures where an NDR exist, two voltage values may give the desired driving current. Unstable oscillations between these states cause lasing to cease as soon as this current density is reached. The L–I curves predicted by the DM model also appear to be linear while experimentally the rate at which power increases with increasing current reduces. This is attributed to the increased current causing more self-heating of the device which reduces available gain.

4.8 Comparison to rate equation and NEGF models

A comparison of the DM model results (with the QCL in an off state) are shown in figure 4.11 for the reference record QCL at different temperatures. It can be seen that the rate equation approach [82] predicts a large current spike at 9.8 kV/cm

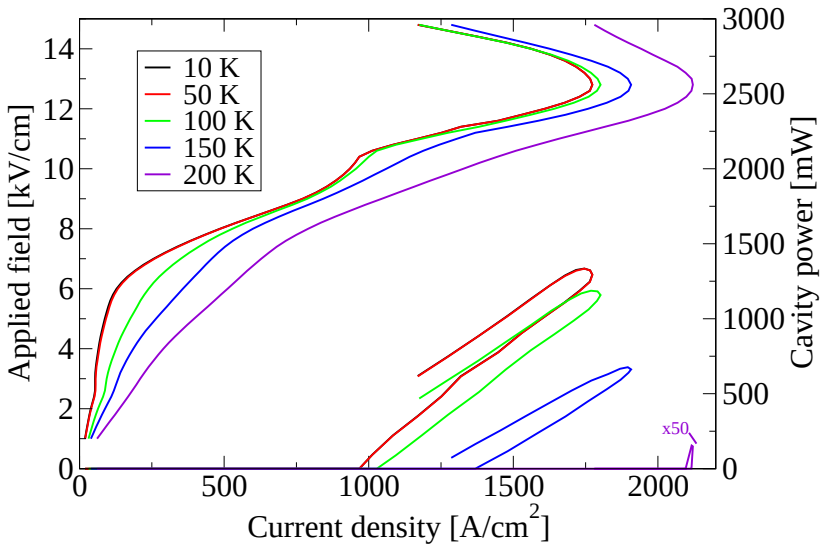

Figure 4.10: Calculated field and emitted power as a function of current density at different lattice temperatures. A ridge area of 10 µm×200 µm and losses of 13.5 cm^{-1} were assumed.

while only a shoulder of the main peak is observed with the DM model. This is due to the limitations presented in Section 4.1 where the rate equation approach was explained to allow instantaneous transport of electrons when wavefunctions spread over several periods of the device. It is therefore shown to be important that the time taken to tunnel across barriers such as the injection barrier be taken into account.

In regions where this unphysical hybridisation of the wavefunctions does not occur, the gain and current predicted by the devices are similar. The rate equation approach is shown to also capture the decreasing peak gain with a rate of decay similar to that predicted by the DM method. However at 200 K the rate equation approach predicts substantially higher gain of 24 cm^{-1} compared with 13.5 cm^{-1} predicted by the DM model. The rate equation approach used for these simulations does not account for cavity light field interaction and no comparisons were possible

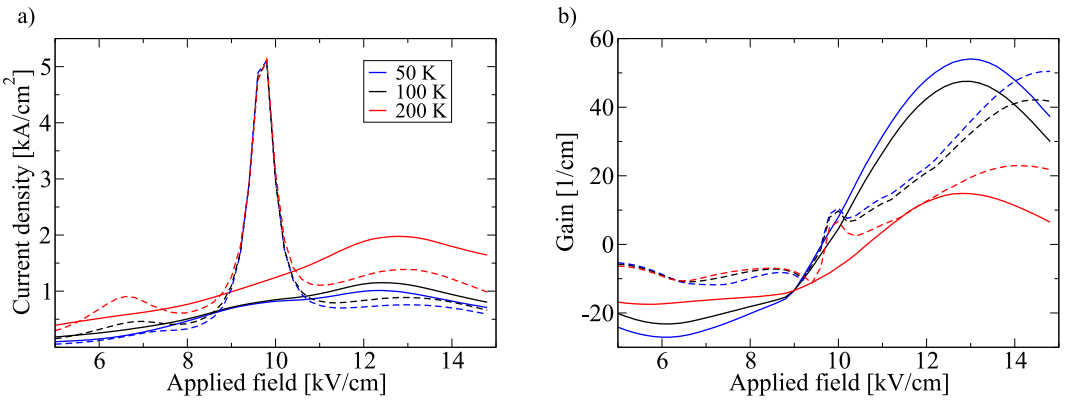

Figure 4.11: Comparison of rate equation (dashed) and density matrix (solid) models applied to the reference QCL at different temperatures.

for the QCL in an on state.

A recent investigation has shown that a similar (simplified) density matrix approach is sufficient to obtain good agreement with experimental and NEGF results for mid-infrared QCLs [87]. In recent collaborations between the present author and D. Winge and A. Wacker at the University of Lund, a comparison of the NEGF [71] and DM approaches for THz designs was completed. These structures are significantly different from mid-IR structures since their energy spacings and therefore scattering rates are significantly different. Figure 4.12 shows the current density for on and off simulations with these two approaches. Good agreement of the current density until the shoulder at 11 kV/cm is achieved. Beyond this, the NEGF model predicts an NDR region. In this model, the energy of the subband states is affected strongly by its scattering interaction with other states. Under the main alignment where the DM model predicts a peak at 12.2 kV/cm, the NEGF model predicts a strong scattering rate due to alignment of subband levels. This shifts the energy of the ULL and LLL states in energy and decreases the overall current. While the current is changed due to this scattering, the population inversion required for lasing

is still achieved in the NEGF model at the correct applied field. This is evident by the QCL turning on and off at 11 kV/cm and 14.5 kV/cm respectively.

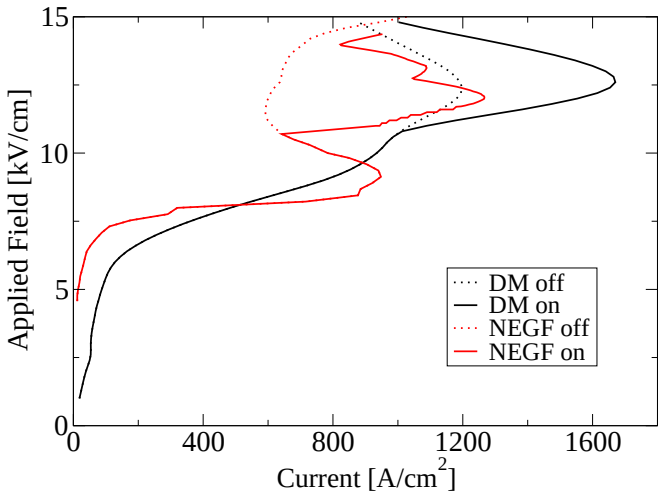

Figure 4.12: Comparison of DM model presented in this chapter and NEGF model described in Ref. 71. Good agreement below threshold is achieved for the shape and magnitude of the current density.

The confined subband states used in the DM model do not change significantly with the scattering rate (only the amount found by the iterative Schrödinger-Poisson calculation) and therefore this valley where the QCL is lasing is not predicted. This may indicate an overestimation of scattering on the self-energy calculated by the NEGF approach. Good agreement in the magnitude of photon-driven current (the difference between current in on and off states at a fixed applied field) is achieved. At peak output power, the difference is calculated as 500 A/cm^2 for the DM model and 580 A/cm^2 for the NEGF model. These results suggest that the DM model is capable of obtaining good agreement with experimental QCLs without the need for computationally intensive NEGF modelling. It is noted that the DM approach takes around 20 s to complete a simulation for a single bias and temperature point

to obtain a full gain spectrum on a standard desktop computer. Similar simulations with the NEGF approach take significantly longer to obtain gain measurements at each frequency sweep point.

4.9 Series resistance in experimental QCLs

Simulated QCL characteristics such as current and power versus current density may differ from experimental measurements for many reasons. These include the IFR values, waveguide losses, series resistances, and contact voltage drop effects amongst other things. While IFR values and waveguide losses affect current densities and output power directly, the position of these with respect to voltage may also change. The heterostructure wafer with the active region is typically fabricated into ridges, with metal deposited on top and either directly below the active region or onto highly doped substrate material alongside it. These form contacts (as well as provide confinement for the optical mode) which wire bonds are then attached to so that current can be supplied to the structure. These contacts can induce a voltage drop and/or a series resistance R_{s}, in series with the device that shifts the physical I–V curve. To estimate the magnitude of the series resistance, the R_{S} is found as [88]:

$$R_{\mathrm{s}} = \frac{(V^* - V)}{I_A(V)} \tag{4.30}$$

where V is the simulated voltage drop across the QCL at its main peak, V^* is the resonant experimental voltage (including contacts) and I_A is the resonant current (theoretical or experimental as these should agree).

Several groups have regrown the 200 K reference structure since its demonstration in 2012 [89] in order to improve upon its design, however its peak operating temperature has not yet been matched. One study presented in Ref. 89 attempted to use tall AlAs barriers to suppress continuum leakage current. The reference structure from Ref. [8] was regrown and current densities were shown to be similar

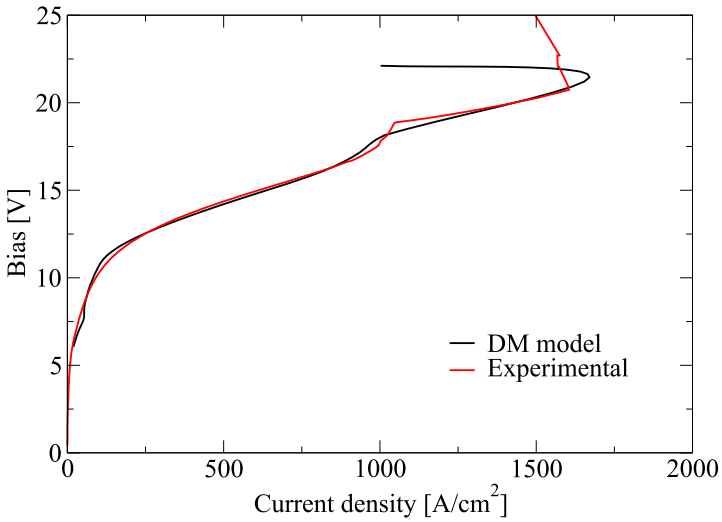

Figure 4.13: Fitted DM results with experimental results presented by Chan *et al.* in Ref. 89 at 50 K. DM results have a constant voltage drop of 5 V and contact resistance of 0.8 Ω applied.

however the voltages were much higher. Figure 4.13 shows the experimental and simulated current density for the device at 25 K. Values of contact drop and series resistance were found by trial-and-error until the DM model results had the closest match with experimental presented by Chan *et al.* in Ref. 89. Excellent agreement is obtained with a constant voltage drop of 5 V and contact resistance of 0.8 Ω.

4.10 Conclusion

A method for the simulation of QCL operation using an extended density matrix simulation has been described. It includes some coherent effects such as the time taken for electrons to tunnel through the injection barrier and is capable of including the cavity light field interaction. It has been used to explain the decreasing gain and therefore decreasing output power performance with increasing lattice temperature. Increasing temperature leads to increased scattering and reduces the population

inversion by non-radiative emission where electrons travel up the ULL subband to emit LO phonons and also the thermal-backfilling of the LLL. This model has been validated by comparing directly to rate equations and NEGF simulations of the current 200 K reference structure and being shown to have similar predictions for electron transport.

The density matrix results have also been compared with regrowths of the current high T structure [89] and it was found that fitting with a series resistance and contact voltage drop are necessary for agreement. This model has been used with all the material parameters and scattering rate calculations presented in Chapters 2 and 3 for AlGaAs/GaAs QCLs however it may also be used with direct substitution of parameters for AlGaN/GaN QCLs. The model is used in Chapter 5 to propose $Al_xGa_{1-x}N$/GaN structures which provide gain. The feasibility of their realisation are confirmed with investigations in Chapters 7 and 8 on intersubband absorption and transport.

Chapter 5

QCL active region design

This chapter discusses the design of THz QCL active regions. The DM model investigated in Chapter 4 is used to investigate various parameters such as doping level and barrier height that affect QCL gain. A genetic optimisation algorithm is presented and applied to the current highest temperature $Al_xGa_{1-x}As/GaAs$ design and it is shown that the diagonality of the lasing transition varies depending on the operating temperature that the structure is designed for. A previously proposed $Al_xGa_{1-x}N/GaN$ QCL design is modelled and it is shown that gain broadening due to fast LO phonon scattering and interface roughness scattering lead to insufficient gain at any temperature. Solutions to these performance degradation mechanisms are used to optimise a structure, and an output design with emission at 3.25 THz at room temperature is analysed.

5.1 Introduction

QCLs have undergone intensive research over the last two decades with mid-IR devices achieving high temperature continuous wave operation of over 5 W [90]. Terahertz devices have seen much slower progress, and the development of high

power, room temperature THz devices is highly sought after. The first THz QCL used a bound-to-continuum (BTC) active region [7], however it has been shown that resonant phonon designs are required for high temperature operation. The last three record temperature QCLS (178 K in 2008 [91], 186 K in 2009 [92] and 200 K in 2012 [8]) used the RP mechanism and these had small changes in layer thicknesses with small improvements achieved by lowering cavity losses. Gain cannot be increased indefinitely with increased doping, and this is shown in Section 5.2.

Alternative techniques must be employed for further progress in THz QCLs. All of the previous record devices employed barriers with alloy contents of 15 %, however recent investigations [89, 93] have freed this parameter. In Ref. 93 variable height barriers were used to optimise the current record temperature design and a predicted increase of 31 K was achieved. Attempts to realise these structures experimentally [94] found that maximum lasing temperatures obtained were lower than that of the reference design; nevertheless this indicates the viability of structures with different barrier heights. The designs used in Refs. [93] and [94] used two alloy contents for the $Al_xGa_{1-x}As$ barriers which adds additional complexity for MBE growers who typically calibrate the flux of the Al cell to achieve a desired alloy concentration. In contrast, Ref. 89 demonstrates the selective replacement of $Al_xGa_{1-x}As$ barriers with AlAs barriers for which the growth rate does not need additional calibration, a situation which may be preferred for some growth teams. A theoretical analysis of these structures is given in Section 5.3.

Automatic optimisation of QCLs could be a promising tool to search a large parameter space of possible active region designs and this is investigated in Section 5.4. The effect of thermal activation on electron distributions within subbands was shown in Chapter 4 to reduce population inversion and gain. $Al_xGa_{1-x}N/GaN$ is regarded as a promising alternative material due to its larger phonon energy reducing non-radiative emission. Optimisation is then used in Section 5.4 to obtain a

high temperature design with this material system.

5.2 Effect of doping on gain and dephasing

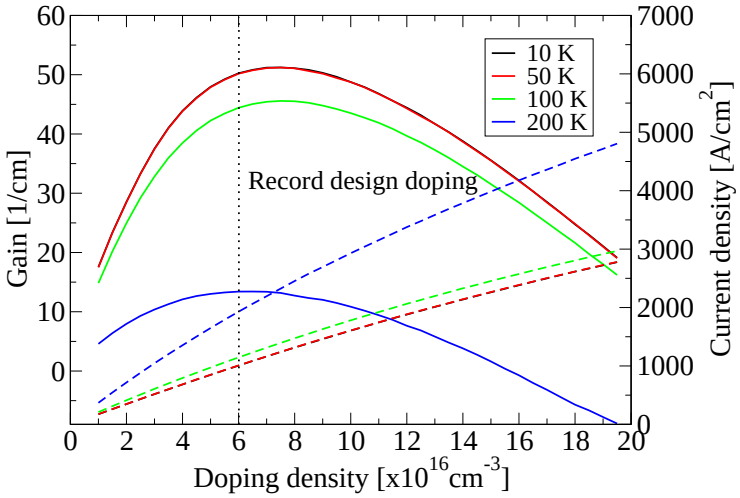

Figure 5.1: Gain (solid lines) and current density (dashed lines) calculated for the current record temperature structure at 12.2 kV/cm versus volume doping density of the central 5 nm section of the extractor well. The vertical dashed line indicates the doping level present in Ref. 8.

Equation 4.23 in Chapter 4 suggests that the overall gain of a structure with a fractional population inversion is proportional to its sheet doping density. Figure 5.1 shows the effect of increased doping on the unsaturated gain and current density at different temperatures. It can be seen that for low temperatures the peak volume doping density for the central 5 nm of the extractor well is $7.5 \times 10^{16}\,\mathrm{cm}^{-3}$. At 200 K this peak gain is achieved earliest at $6 \times 10^{16}\,\mathrm{cm}^{-3}$ which is the doping density of the experimental record structure at 12.2 kV/cm. The current density is calculated to increase with doping density as expected, however this increase is sub-linear.

Current does not increase linearly as scattering due to ionised impurities decreases the dephasing time for transport from the injector state into the ULL of the QCL. This is also evident in the gain–doping characteristics where an increasing inversion occurs until dephasing processes take over at high levels of doping. These results suggest that for any QCL structure an optimum doping level exists and simply increasing doping of a device with gain will not offer a route to higher temperature THz QCL operation.

5.3 Tall-barrier designs

5.3.1 Gain suppression by interface roughness

As described in Section 5.1, changing the barrier heights of $Al_xGa_{1-x}As$/GaAs QCLs gives a new degree of freedom to achieve gain at high temperatures. While some recent investigations have focussed on optimising the optically active states, Ref. 89 uses AlAs barriers to suppress leakage current to continuum states above the maximum conduction band edge. By replacing the injector barrier with AlAs as shown in figure 5.2, thermally activated carriers in parasitic state $n = 5$ experience more confinement. In the experimental results presented in Ref. 89, this device has a lower threshold current density at temperatures above 150 K, indicating reduction of the thermally activated leakage current. Another device is also presented in Ref. 89 where all barriers were replaced with AlAs, however no lasing was observed and this was conjectured to be due to excessive interface roughness broadening. Ref. 89 did not confirm these results theoretically, and no simulations to date have shown the suppression of gain in THz QCL designs due to AlAs barriers.

Figure 5.3 shows the calculated gain versus applied field for each of the structures in Ref. 89. Similar values of gain are predicted for the reference and structure with an AlAs injection barrier. However, the design with all AlAs barriers has a peak gain of

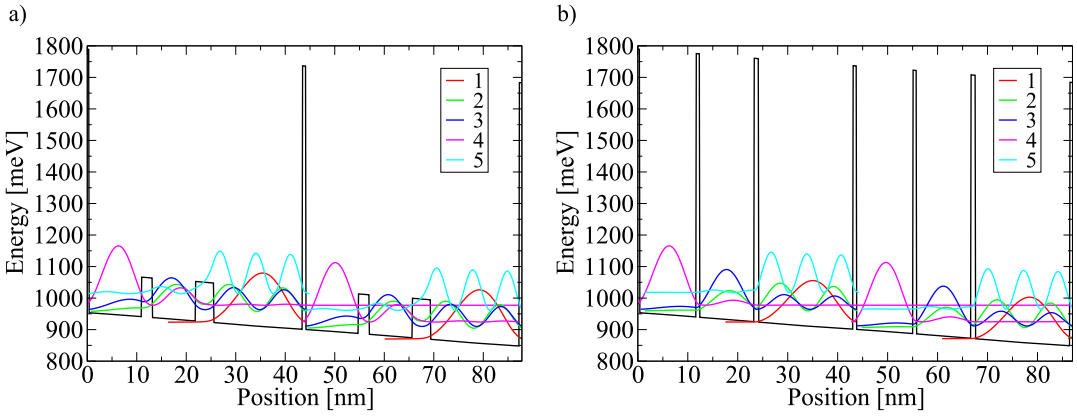

Figure 5.2: (a) Bandstructure and wavefunction plot of sample 'NRC-V775C' in Ref. 89 at 12.2 kV/cm with an AlAs injection barrier. (b) Same for sample 'OWI230T' in Ref. 89 where all barriers have been replaced with AlAs to reduce leakage current.

7 cm^{-1}, despite a low simulated lattice temperature of 10 K. This is consistent with the experimental observations of this device. To confirm that interface roughness broadening is the main cause of gain suppression in these structures, the interface roughness height (Δ) was lowered to 1.0 Å. Figure 5.4 shows how gain recovers to a peak value of 30 cm^{-1}. The sensitivity of the gain in THz QCLs to the barrier offset is because the interface roughness scattering rate is proportional to the square of the interface potential. Therefore an increase from 15 % alloy barrier to a 100 % alloy barrier represents a factor of 36 increase. To avoid this, barrier heights should be kept low, or the overlap of the wavefunctions with the interface should be minimised. Alternatively, AlAs could be sandwiched between $Al_{0.15}Ga_{0.85}As$ barriers so that the overlap with the tall barrier is spatially separated from where the wavefunctions are largest; this technique has been applied successfully to mid-IR QCLs [95].

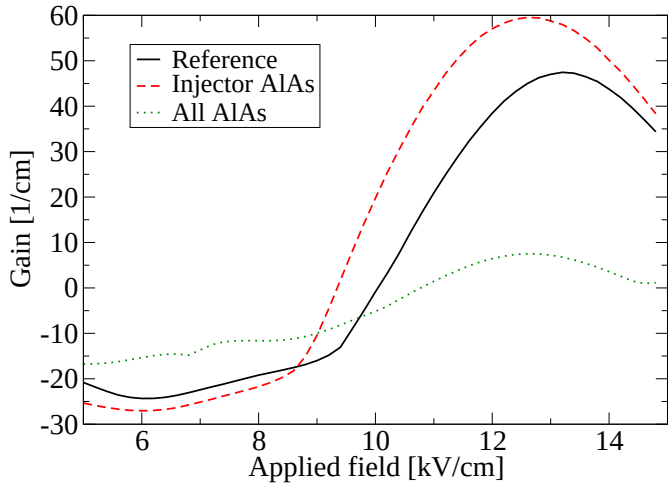

Figure 5.3: Gain–bias plot for the reference design and those in Ref. 89. The reference design and injector AlAs design have similar gain values at 10 K however design with all AlAs barriers is not expected to lase due to insufficient gain due to IFR broadening.

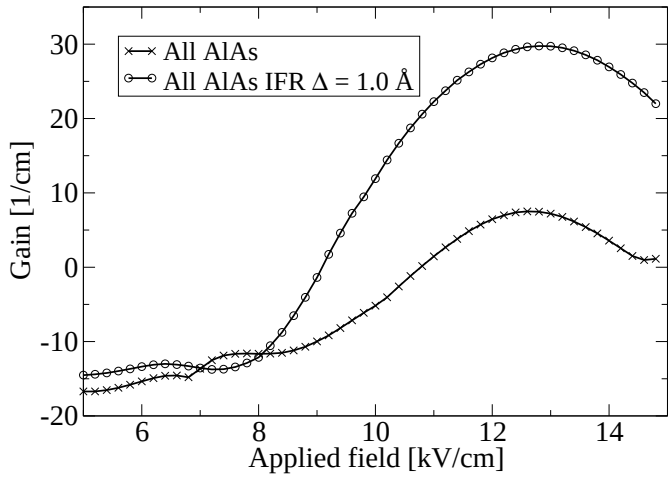

Figure 5.4: Gain–bias characteristics for the all AlAs design at 10 K with standard and reduced IFR parameters. Standard parameters: $\Delta = 2.8$ Å, $\Lambda = 100$ Å. Reduced parameters: $\Delta = 1.0$ Å, $\Lambda = 100$ Å.

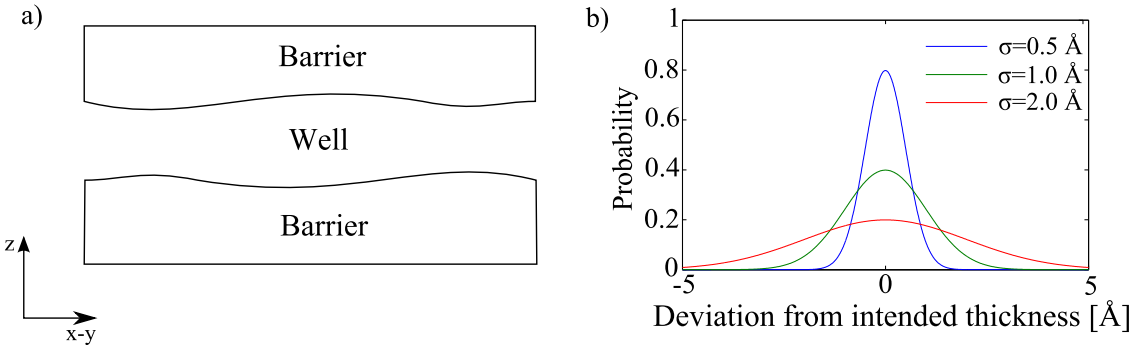

Figure 5.5: (a) Schematic of long range variations in layer widths in the x–y plane which cause variations in subband separations and alignments. (b) Normal distribution of layer widths for various standard deviation values.

5.3.2 Long-range thickness variations

It is also conjectured in Ref. 89 that the design with all AlAs barriers is more susceptible to long range fluctuations in barrier width. While short range roughness creates a perturbation that affects the states calculated with a perfect crystal potential, long range thickness variations change the confinement of the carriers and their energy separations. While other growth issues such as material inter-diffusion have been studied in QCLs [96], this long range fluctuation has not been investigated. Figure 5.5(a) shows how uncorrelated variations in the barrier and well materials change the thickness of the well in the x–y plane. A normal distribution is assumed for the variation of the layer thicknesses around the intended (nominal) thickness. Estimates of the standard deviation for typical QCL samples were obtained from a transmission electron microscopy (TEM) image of an $Al_xGa_{1-x}As$/GaAs QCL [97]. The standard deviation of the layer thicknesses were then averaged for the state lifetime for a carrier in a typical subband. Values of 1 Å were obtained for a typical QCL structure. Figure 5.6 shows the calculated gain–bias sweeps for the three structures with various values of standard deviation. For each simulation, layer thicknesses

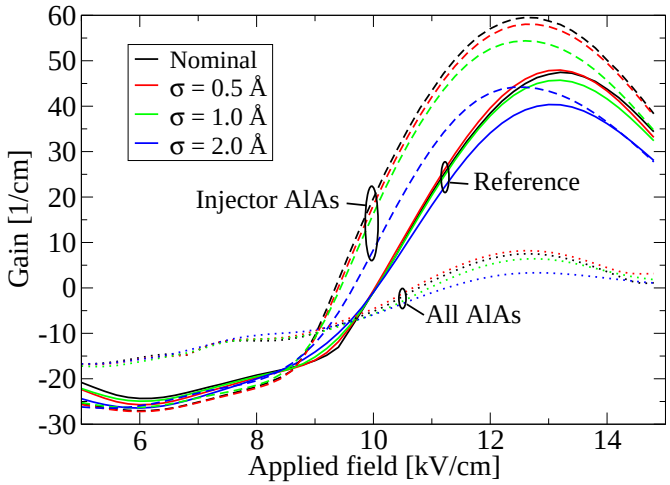

Figure 5.6: Simulated gain–bias characteristics for the reference design and those in Ref. 89 with standard deviation values.

were randomly generated on a normal distribution with a mean value corresponding to the intended width and standard deviations of 0.5, 1 and 2 Å. Gain and current density data calculated from full self-consistent bias sweeps were averaged over 100 random variations of the structure.

The peak gain of the "reference" structure decreases 13 % from 47 cm^{-1} to 40 cm^{-1} between the structure calculated with nominal layer widths and with the inclusion of long range fluctuations with a standard deviation of 2 Å. For the "injector AlAs" structure the decrease is 25 % from 60 cm^{-1} to 44 cm^{-1}, and for the "all AlAs" structure the decrease is 61 % from 8.2 cm^{-1} to 3.2 cm^{-1}. The enhanced sensitivity of the injector and all AlAs structures is attributed to the narrower injection barrier; as it is small to begin with, small variations in thickness cause more significant variations in the coupling strength and injection alignment. Figure 5.7 shows the gain spectrum versus bias for each value of standard deviation. The gain spectrum is affected by both a reduction in gain for samples of the structure where

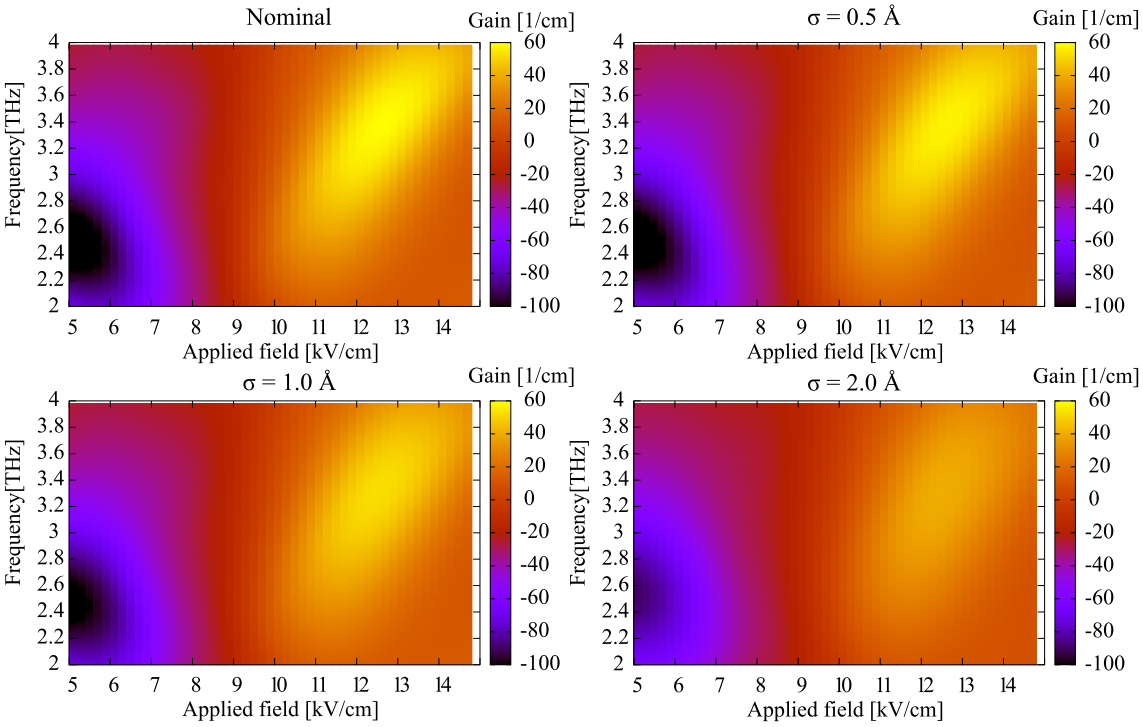

Figure 5.7: Calculated gain versus frequency and applied field for different long range roughness standard deviations for the structure with an AlAs injection barrier.

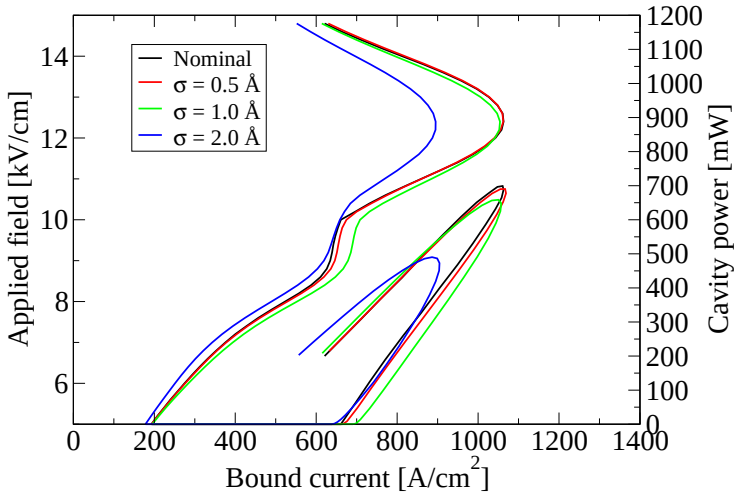

Figure 5.8: Current–voltage and light–current characteristics for the injector AlAs QCL at 10 K for various long-range roughness standard deviations.

carrier injection is not efficient, and a broadening effect due to the varying subband separation of the optical transition. Figure 5.8 shows the calculated I–V and L–I characteristics for the injector AlAs structure. The reduction in gain leads to a significant reduction of emitted output power. From these results it is concluded that long-range interface roughness can significantly affect the optical properties of QCL structures, and this sensitivity must be accounted for to design robust structures that are engineered for a particular problem such as tall barriers for leakage current.

5.4 Genetic optimisation of QCLs

QCL active region design is a complicated task to complete manually; changing the layer thickness of one well to improve alignment or localisation often affects other states in a non-linear manner. Often a trial-and-error approach is adapted, and this can lead to only a narrow range of the parameter space being investi-

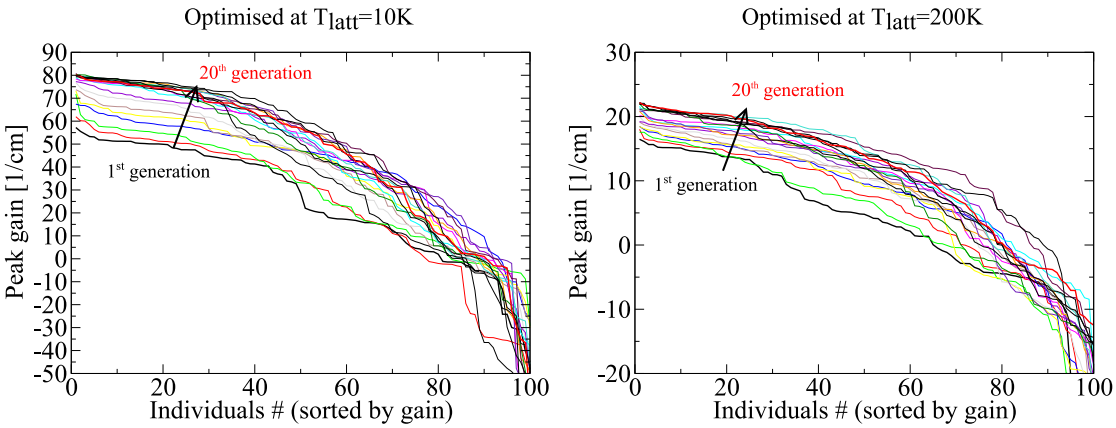

Figure 5.9: Genetic optimisation of a THz QCL based on the current high temperature design in Ref. 8. All individuals are sorted by descending gain after each generation and the top structures are used to generate further random generations.

gated. Automated design techniques have been applied to QCLs previously, such as the simulated annealing technique [98] and genetic algorithms [99, 100]. Currently, no genetic optimisation has been applied to the further improvement of the current highest temperature design in Ref. 8 and this is described in the present section. Genetic algorithms imitate the process of natural selection by generating individuals with random variations. The subsequent generation then uses the best structures (evaluated by some figure of merit) for the basis upon which to perform more mutations. When applied to QCL structures, these mutations can be to the layer thicknesses, doping profile, barrier height or applied bias. The most significant QCL figure of merit is typically its unsaturated gain, which determines the lasing power of a structure.

While Section 5.3 discussed the possible benefits of variable height barriers, allowing a genetic algorithm this degree of freedom will likely result in a significant variation in barrier alloy contents which may be a non-trivial issue for growers. Therefore, in the following optimisations, the barrier alloy fraction is fixed to 15 %.

Additionally, the sheet doping density per period was also restricted to be the same as the initial structure. Only the QCL layer thicknesses were varied, allowing a random layer thickness change between ±20 %. For each structure, a full density matrix simulation is completed and the gain evaluated for a narrow frequency range where emission is desired. 100 individuals per generation are generated, and their gain value calculated and sorted. The top ten structures of the previous generation are then used as a basis to generate ten structures each. Over the course of 20 generations, 2000 QCL structures are evaluated and the top structure is then characterised with bias and temperature sweeps. While a fixed electron temperature is assumed (based off Figure 4.6) during the optimisation procedure, the characterisation sweeps are completed with thermal balance included in the simulation. Other input parameters are the applied field and the lattice temperature that the layer thicknesses are optimised for. Figure 5.9 shows the evolution graphs for optimisations completed at lattice temperatures of 10 K and 200 K. These show that increases between subsequent generations become increasingly smaller after the eighth generation, indicating some convergence on the maximum value possible. The structure optimised at a low temperature of 10 K shows a 45 % peak gain increase from 55 cm^{-1} to 80 cm^{-1} for individual 1 in the first and twentieth generations respectively while the high temperature 200 K optimisation increases the predicted gain from 13 cm^{-1} to 23 cm^{-1}. The layer widths for the 10 K structure are **42**/95/**19.4**/81.5/**28**/52/<u>48.5</u>/69 Å where the $Al_{0.15}Ga_{0.85}As$ barriers are in bold, the GaAs wells are in regular text, and the underlined well section is n-doped with Si at 6.2×10^{16} cm^{-3}. The layer widths for the 200 K optimised structure are **32**/93.5/**26**/80/**31**/59/<u>59.5</u>/48 Å where the underlined well section is n-doped at 5.06×10^{16} cm^{-3}.

Figure 5.10(a) shows the evolution of the injector coupling strength (1'→4) sorted by descending gain in each generation. This indicates this value remains around 1.2 meV and variations from this lead to reduced gain; it is also noted that this

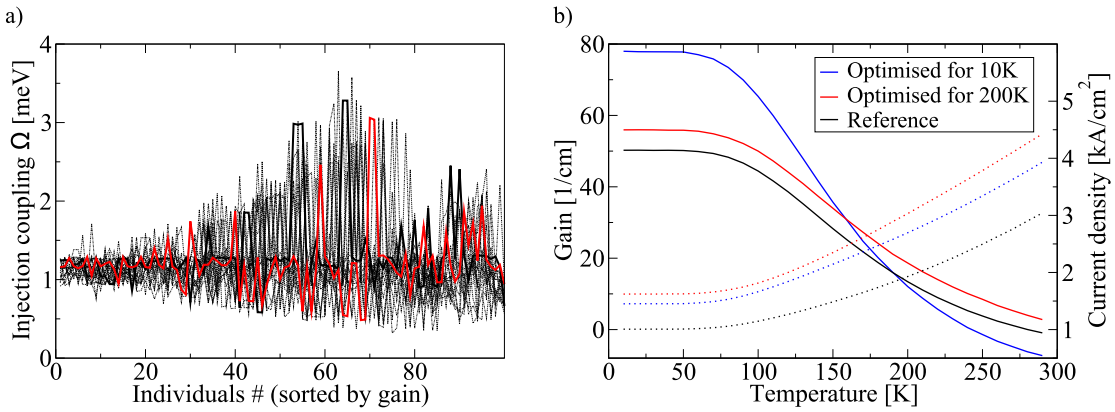

Figure 5.10: (a) Coupling strength for every simulated device sorted as in figure 5.9 for the 10 K genetic optimisation. Solid blue and red lines indicate the first and twentieth generations respectively. (b) Gain and current density versus lattice temperature for the structures optimised at different temperatures.

value is similar for optimisations at both temperatures (not shown). The gain and current characteristics versus lattice temperature for each structure are shown in figure 5.10(b). The structure optimised at a low temperature has a large unsaturated gain at low temperatures however is very sensitive to increasing temperature. On the contrary, the structure optimised for high temperature operation has a lower gain at low temperature but is significantly less sensitive to temperature increases. The current densities for the optimised structures are predicted to be ∼50 % higher than the reference structure in Ref. 8. This will lead to larger self-heating of the device, however pulsed operation may still be feasible.

Figure 5.11 shows the bandstructure for both designs. At low temperatures the optical transition evolves to have a larger dipole matrix element, however at high temperatures it is necessary for this transition to become more diagonal to reduce non-radiative emission processes. z_{43} reduces from 6.44 nm for the 10 K optimised structure at 12.2 kV/cm to 5.9 nm for the 200 K optimised structure. At 200 K the

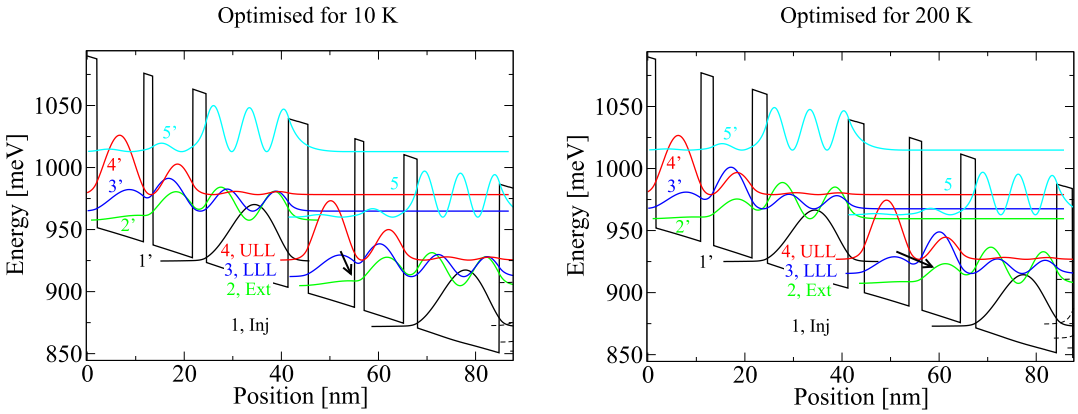

Figure 5.11: Bandstructure and wavefunction plots of the top structures after genetic optimisation at 10 K and 200 K. The arrow indicates an exaggerated change in the diagonality of the optical transition.

LO phonon scattering rate from state 4 into state 2 is reduced from $4.62\times10^{12}\,\mathrm{s}^{-1}$ to $2.66\times10^{12}\,\mathrm{s}^{-1}$ between the two designs. These results confirm experimental results demonstrated in literature that high temperature designs require increasingly diagonal transitions [101].

5.5 $Al_xGa_{1-x}N/GaN$ QCL design

5.5.1 Previous designs

Shortly after the first demonstrations of intersubband absorption in $Al_xGa_{1-x}N/GaN$ structures, this material was proposed for QCL active regions [15, 50]. It was shown that the LO phonon energy of 92 meV significantly reduces the thermal degradation methods such as non-radiative phonon emission between the ULL and LLL. Additionally, a design was proposed to exploit the larger conduction band offset between AlN and GaN of 2 eV which can comfortably confine subband separations required for emission at 1.55 µm [50]. Several THz nitride

QCLs have been proposed [15, 80, 102–104], however it was shown in Ref. 16 that these typically underestimate gain broadening due to fast broadening. The models used for these initial designs took the linewidth typical for $Al_xGa_{1-x}As$/GaAs QCLs which is around 2 meV [15]. The Frölich coupling constant used in the LO phonon scattering calculation (Eq. 3.10) depends on the low- and high-frequency dielectric constants. These values are 10.28 and 5.3 for GaN and 12.9 and 10.89 for GaAs; indicating a Frölich constant 15 times larger than that for $Al_xGa_{1-x}As$/GaAs QCLs. It was shown in Ref. 80 that $In_yAl_xGa_{1-x}N$/GaN systems could be engineered so that the lower laser state is spatially decoupled from the LO phonon extraction well in a three well structure similar to the current $Al_xGa_{1-x}As$/GaAs high temperature design. This design was investigated with a DM model similar to that in Chapter 4, however the coherent tunnelling extraction transport is treated with spatially extended wavefunctions. While the barrier is only 3.3 nm, the nitride triangular well potential extends the distance over which carriers must tunnel and therefore extraction efficiency may be overestimated. Moreover, it is desirable to propose designs with binary rather than tertiary alloys which are currently grown more commonly by MBE growers.

The $Al_xGa_{1-x}N$/GaN QCL shown in figure 5.12 was proposed in 2008 by Bellotti *et. al* in Ref. 102. This structure is engineered to emit at 2 THz and designed so that the extraction well states are separated by an energy similar to that of the LO phonon energy. Electrons are injected from the injector state (red) to the ULL (pink), which emits a photon. The LLL (blue) is then aligned with the extraction state (green) which is resonantly depopulated to the injector state. Figure 3 in Ref. 102 shows how this design is more insensitive to temperature by a factor of over three with a population inversion predicted up to room temperature. Figure 5.13 shows the gain versus applied field (calculated with the DM model in Chapter 4) for this structure with standard and reduced IFR parameters. It is found

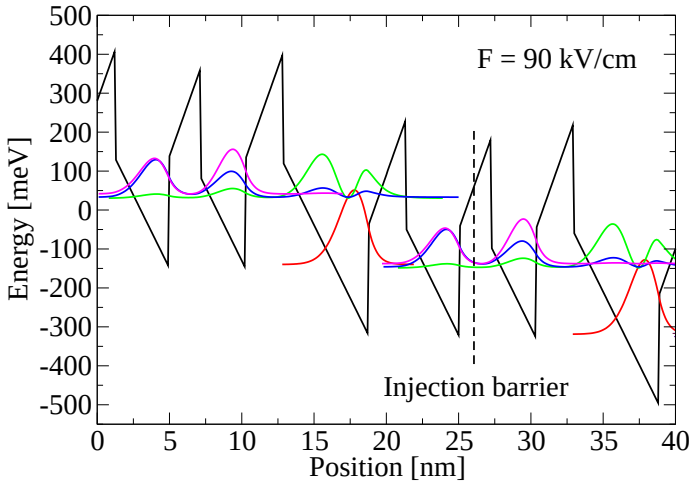

Figure 5.12: Bandstructure and wavefunction plot of the three-well QCL design presented in Ref. 102.

that the gain predicted in Ref. 102 is only replicated if the IFR roughness height is reduced to 0.1 nm. Even with this reduction, gain is not predicted at room temperature, and this is attributed to the effect of broadening due to LO phonons also being neglected. The increased sensitivity of the structure to IFR scattering can be explained by considering the increased conduction band offset potential at the $Al_xGa_{1-x}N/GaN$ interface; the difference for a defined alloy value is typically two times larger than the offset at an $Al_xGa_{1-x}As/GaAs$ interface. Section 5.3 described how IFR scattering is proportional to the square of this discontinuity, and it is the same mechanism occurring in this structure.

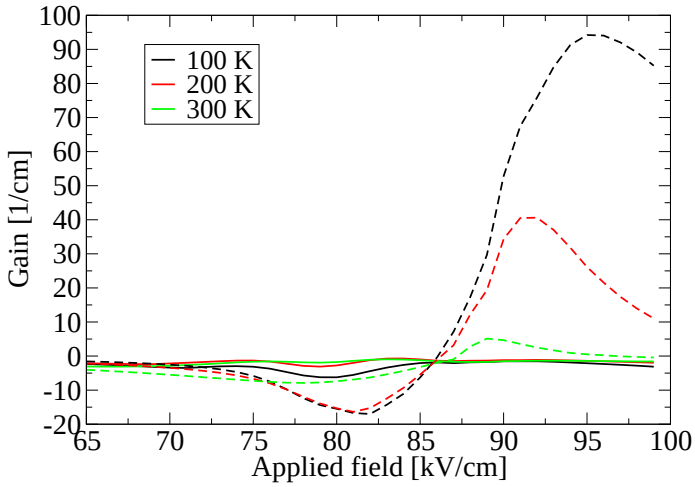

Figure 5.13: Calculated gain versus applied field for the three-well QCL design presented in Ref. 102 with standard (solid) and reduced (dashed) IFR roughness height.

5.5.2 Optimised THz design

The genetic algorithm described previously relies upon the initial structure to define the general parameters of the structure: number of wells, alloy content, and number of bound states. Figure 5.13 showed how IFR scattering reduced the gain of a previous $Al_xGa_{1-x}N$/GaN QCL and therefore 8 % barrier alloy was used for the initial structure instead of 15 % barrier alloy content. This leads to an $Al_{0.08}Ga_{0.92}$/GaN discontinuity of 140 meV, in line with the typical $Al_{0.15}Ga_{0.85}As$/GaAs 149 meV discontinuity in the current highest temperature QCL [8]. Assuming similar IFR parameters (as suggested is possible by Ref. 105, Ref. 106, and the results presented in Chapter 8) this will reduce gain broadening significantly. Additionally, as shown in Refs. 16, 80, the enhanced LO phonon scattering in $Al_xGa_{1-x}N$/GaN

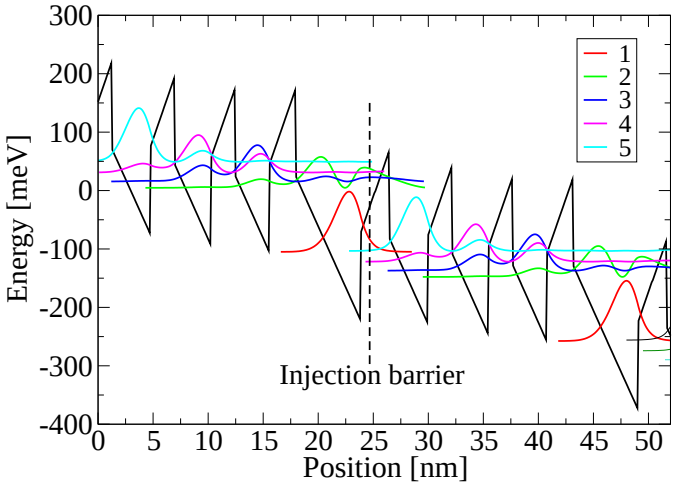

Figure 5.14: Bandstructure and wavefunction plot of the optimised $Al_xGa_{1-x}N$/GaN QCL at 61 kV/cm.

QCLs can make the LLL lifetime too short and broaden the gain excessively; therefore, the initial structure had an extra well inserted to improve separation of the LLL and resonant extraction mechanism, similar to the "hybrid" design presented in Ref. 107. A similar optimisation to that in Section 5.4 was performed with an applied field of 60 kV/cm. This applied field bias was chosen to be in line with other $Al_xGa_{1-x}N$/GaN QCLs such as that in Ref. 15.

Figure 5.14 shows the calculated bandstructure and wavefunction plot for the optimised structure at $F = 60$ kV/cm. The layer widths for this design are **26**/35/**22**/33/**22**/31/**24**/<u>59</u> Å where the $Al_{0.08}Ga_{0.92}N$ barriers are in bold, the GaN wells are in regular text, and the underlined well section is n-doped with Si at 1.2×10^{17} cm^{-3}. Electrons are resonantly injected by state 1' into state 5 which is 17.5 meV (4.43 THz) above state 4; the injection coupling strength $\Omega_{1'5}$ was calculated to be 3.57 meV. Scattering and lasing transport occurs between states and state 2 (green) is depopulated by LO phonon emission to state 1 which lies 109.6 meV be-

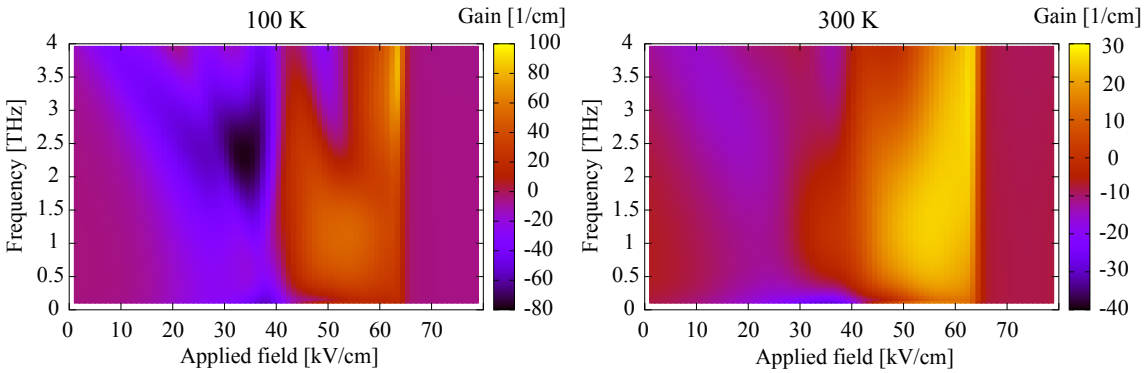

Figure 5.15: Calculated spectral gain versus applied field for the optimised $Al_xGa_{1-x}N$/GaN QCL operating with peak emission at 3.65 THz.

low it. Figure 5.15 shows the calculated gain spectrum versus applied field at 100 K and 300 K. This shows the gain calculated from 2 THz to 4 THz with gain achieved after a bias of 40 kV/cm. Peak gain at both temperatures is found to be at 3.65 THz corresponding to the energy transition of state 4 into state 3 in figure 5.14. The injector state is therefore found to be state 5, which injects carriers by incoherent scattering transport. Since the injector and LLL states are spatially decoupled, this allows a population inversion to be achieved rapidly when the Stark effect changes the overlap of these states. The lifetime of the lower state is controlled by the overlap of its wavefunction with states 1 and 2; in this design state 2 is spatially extended over the optically active well and the phonon extraction well so that the LLL can remain localised. Figure 5.15 also shows that gain of 26 cm^{-1} is achieved even at room temperatures since this injection scheme remains robust due to suppressed LO phonon scattering caused by the large phonon energy.

Figure 5.16 shows the calculated gain versus applied field for the QCL at different temperatures. While the design was optimised with an input field of 60 kV/cm, at lower temperature peak gain can be achieved at 63 kV/cm over a narrow range. This is not predicted at 300 K, and this is attributed to the resonant characteristics

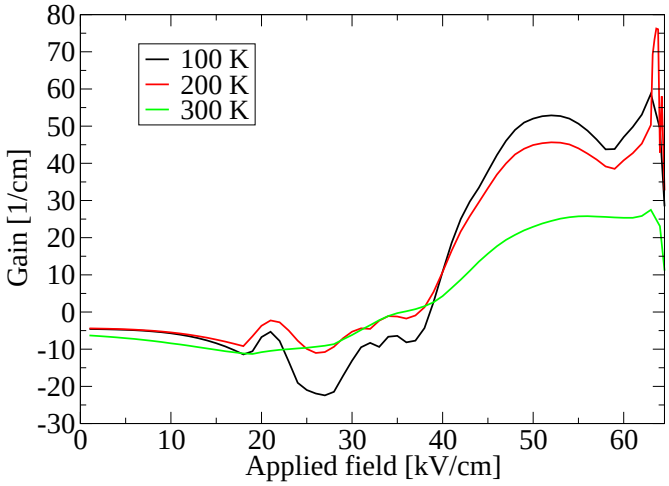

Figure 5.16: Gain versus applied field for the optimised $Al_xGa_{1-x}N$/GaN QCL at different temperatures.

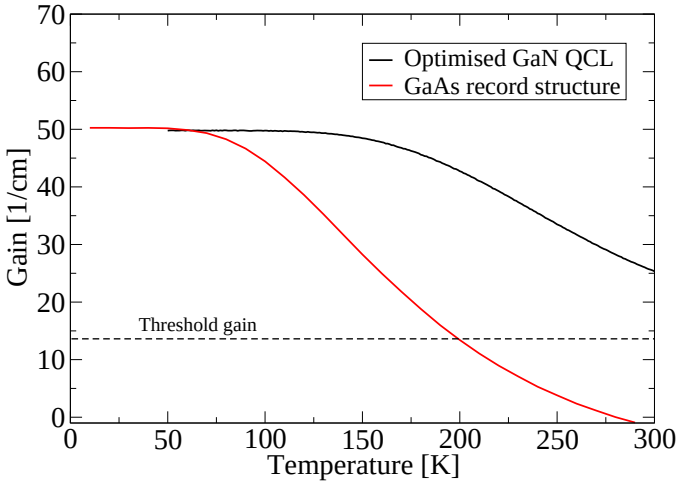

Figure 5.17: Comparison of peak gain versus lattice temperature for the optimised $Al_xGa_{1-x}N$/GaN QCL and the current high temperature $Al_xGa_{1-x}As$/GaAs design in Ref. 8.

of incoherent transport. Gain reduces from a peak value of $55\,\mathrm{cm}^{-1}$ to $26\,\mathrm{cm}^{-1}$ at $F = 61\,\mathrm{kV/cm}$ as the lattice temperature increases from 100 K to 300 K. The peak gain at approximately 50 kV/cm is due to the direct alignment of the ULL with state 1' of the upstream period. This illustrates the restrictions still faced by an automatic optimisation program: changing layer widths with fixed barrier heights and applied fields may reach some local gain maximum in the parameter space. An extreme example of this would be that gain is not possible with any possible structure with zero applied field. Similarly, the optimisation has here produced a design which operates at high temperature, but has several possibilities of applied field that will provide similar gain. Figure 5.17 shows the comparison of the peak gain predicted by the DM model for the optimised $Al_xGa_{1-x}N/GaN$ design with the current high temperature record design in Ref. 8 at 61 and 12.2 kV/cm respectively. At 300 K the $Al_xGa_{1-x}N/GaN$ design is predicted to have a gain of $26\,\mathrm{cm}^{-1}$ sufficient to achieve lasing.

5.6 Conclusion

An analysis of novel QCL designs was presented in this chapter along with approaches to achieve improvements in gain at different temperatures. It was shown that tall barrier QCLs, which are a form of variable height QCL that is easier for MBE teams to grow, can improve threshold current performance at high temperatures. This is due to reduced leakage of carriers to continuum states which improves injection efficiency and reduces the self-heating effect which causes further gain degradation. The density matrix model was used to explain recent experimental data in Ref. 89 in which structures with all AlAs barriers were not expected to lase and it was shown in the present work that this is due to excessive interface roughness broadening which is proportional to the square of the $Al_xGa_{1-x}As/GaAs$ interface

discontinuity. It was also shown by performing statistically averaged simulations that a normal distribution applied to the intended layer thicknesses affects these structures more than typical constant 15 % alloy QCLs due to narrower layers.

Genetic optimisation methods have been shown previously to improve characteristics such as the dynamic operating range of QCLs, however further improvements on the current high temperature QCL design have not been achieved. This approach was applied to the reference structure to show how QCL performance metrics (such as unsaturated gain) can be optimised for different temperatures. For example, low temperature QCLs can be engineered to have a large output power at low temperatures but not operate at 200 K. Conversely, a design that operates at 200 K can be achieved however its performance at low temperatures will be inferior to the previous case due to increased diagonality of the optical transition. Furthermore, it was shown that injection coupling strengths converged to values of 1.2 meV over 20 generations of the genetic algorithm. Using the concepts learned from this analysis of $Al_xGa_{1-x}As/GaAs$ designs, an initial design with lower alloy content and an additional quantum well were used for optimisation of an $Al_xGa_{1-x}N/GaN$ design. The optimised design was shown to have a gain of $26\,cm^{-1}$ at 3.65 THz at 300 K which has been shown to be sufficient for lasing. The results presented in Chapter 4 have validated the density matrix approach for $Al_xGa_{1-x}As/GaAs$ designs and it is shown in Chapters 7 and 8 that the scattering rates used can also achieve good agreement with experimentally observed $Al_xGa_{1-x}N/GaN$ optical and electronic transport properties.

Chapter 6

Origin of voltage signals in THz QCL self-mixing interferometry

This chapter presents the application of the density matrix model to bound-to-continuum QCLs used in self-mixing interferometry. This is one technique in which QCLs can be used in interferometry applications to exploit the promising properties of terahertz radiation. By calculating the change in photon-driven current due to a varying cavity light field, a model is developed that can replicate the experimentally observed magnitude of self-mixing signal with excellent agreement and attribute it to the local gradient of the I–V curve.

6.1 Introduction

Self-mixing (SM) interferometry refers to the partial reinjection of radiation emitted from a laser. The injected radiation field interacts with the intra-cavity field causing measurable variations of the QCL terminal voltage and their optical properties. The first demonstration of this effect was the detection of Doppler shifts caused by moving remote reflectors with gas lasers in 1968 [108]. Important developments using

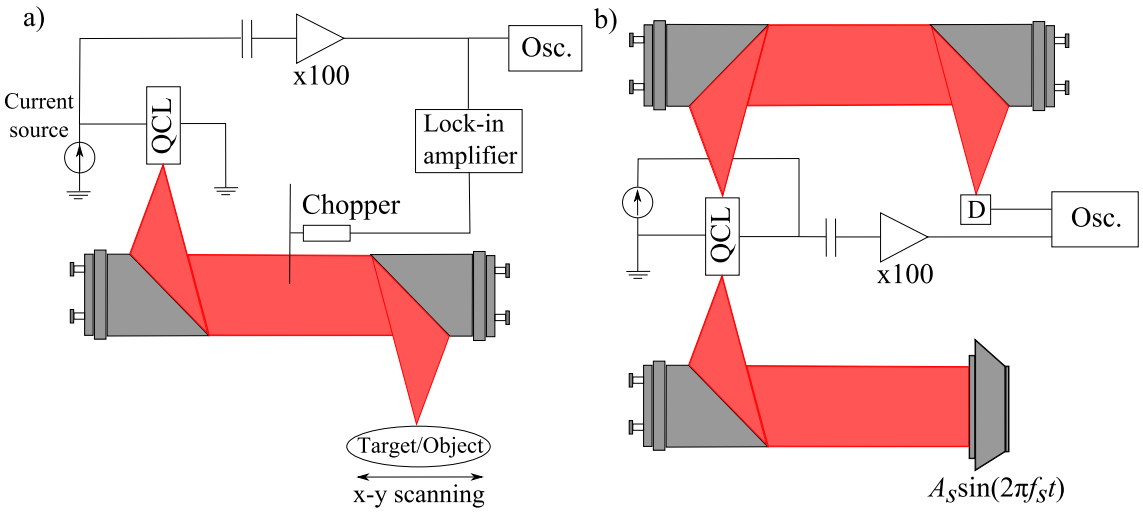

Figure 6.1: Experimental schematics for self-mixing imaging with a THz QCL. (a) THz beam is focussed onto target fixed to translational stage. Feedback is modulated by the optical chopper which is used by the lock-in amplifier to acquire the modulation-amplitude of the self mixing signal. (Osc.=oscilloscope). (b) Collimated beam is focused onto oscillating target (e.g. speaker sub-woofer) which is driven by a sinusoidal voltage. SM signals are also measured by the effect of SM on the power emitted from the back facet with a helium-cooled bolometer, D. In both setups, the QCL is driven by a constant current and the voltage variations are measured with an AC-coupled differential amplifier.

this principle were its use in a self-mixing interferometer to measure optical path length in 1978 [109], and the demonstration of SM with a laser diode in 1986 [110]. The theory of SM with conventional laser sources is well studied and explained by the Lang–Kobayashi approach [111]. Its effect has only recently been demonstrated in THz QCLs [29] for imaging in 2011 by Dean *et al.* following the use of SM to measure the linewidth enhancement factor of THz QCLs [112] in 2008. SM techniques have been applied to displacement sensing [113], high-resolution imaging of concealed objects [30] and 3D imaging of materials using swept frequency interferometry [114].

Figure 6.1(a) shows an experimental set up for a self mixing scheme where emit-

ted THz radiation from one facet is focussed onto a target on a translational stage. The QCL is driven slightly above threshold current and the optical feedback is modulated mechanically by an optical chopper. Reflected emission from this target (several %) of the emitted field strength is reinjected into the cavity and the effect of this on the QCL is measured. While SM signals can be extracted from the cavity optical power with an embedded photodetector, THz QCL measurements are typically done by measuring the change in voltage across terminals with an AC-coupled differential amplifier [29]. In this way, the QCL is used as both a source and detector without the need for extra cryogenic cooling for detectors which is an advantage for possible applications. Alternatively, another setup (figure 6.1(b)) for velocimetry measurements consists of collimated THz radiation incident on an oscillating target such as a speaker sub-woofer driven by a sinusoidal voltage [113]. In this setup, the varying power emitted during SM from the back facet of the device is collected by a helium-cooled bolometer and an oscilloscope is used with the differential amplifier to measure terminal voltage fluctuations. These techniques have been used recently to acquire high-resolution images of objects through varying levels of attenuation and optical path lengths [113]. The upper limit for coherent detection is limited by the linewidth of the free-running laser, which is very small for QCLs ($\Delta f \sim 20$–$30\,\mathrm{kHz}$) leading to a possible maximum path length of $\sim 10\,\mathrm{km}$ [30].

An approximation of conventional modelling techniques (such as approaches in Refs. 113 and 115) is the assumption that measured voltage variations are linear with respect to the cavity change in power, ΔP such that:

$$\Delta V_{\mathrm{SM}} \propto \Delta P \tag{6.1}$$

This is not fully justified in QCL structures since carrier transport is dominated by the mechanisms of subband alignment, intersubband scattering and photon driven transport. Indeed, figure 2(b) in Ref. 29 shows peak sensitivity of a bound-to-continuum (BTC) QCL near threshold and decreasing with increasing current.

Ref. 116 presents a scheme to calculate the terminal voltage response for QCLs, however this approach adapts some approximations typical for diode lasers such as Boltzmanns law of carrier concentration for a changing diode voltage. Recent experimental results shared by P. Dean and colleagues (unpublished) of a BTC device with the same structure as in Ref. 29 has demonstrated a significant increase in sensitivity near cut-off and is the motivation for the present work to explain the underlying physics. BTC devices are preferred for self-mixing interferometry due to their low current densities that allow continuous wave operation. However, they are inherently more complex due to there being over 9 states in each period of the active region leading to an increase in computational expense and uncertainty over the contributions from incoherent and coherent transport.

6.2 Modelling of BTC QCLs

6.2.1 Reduced rate equations

Chapter 4 presented a density matrix model capable of replicating THz QCL power–current and voltage–current characteristics. In addition to this work, the present author has contributed to the modelling of BTC QCLs with a reduced rate equation (RRE) approach in Ref. 117. In this work, Agnew *et al.* use parameters calculated with full rate equations in a time dependent model which couples the ULL and LLL populations, photon densities and temperature of the active region over time. This dynamical model improved upon previous reduced rate equation approaches [118] which assumed fixed laser parameters irrespective of applied bias and temperature, an approach only valid near the conditions they were calculated for. Figure 6.2(a) shows the calculated and experimental L–I characteristics for a 2.9 THz QCL along with experimental data (inset). Excellent agreement of threshold current, roll-over and cut-off current is achieved as well as decreasing emitted power with increas-

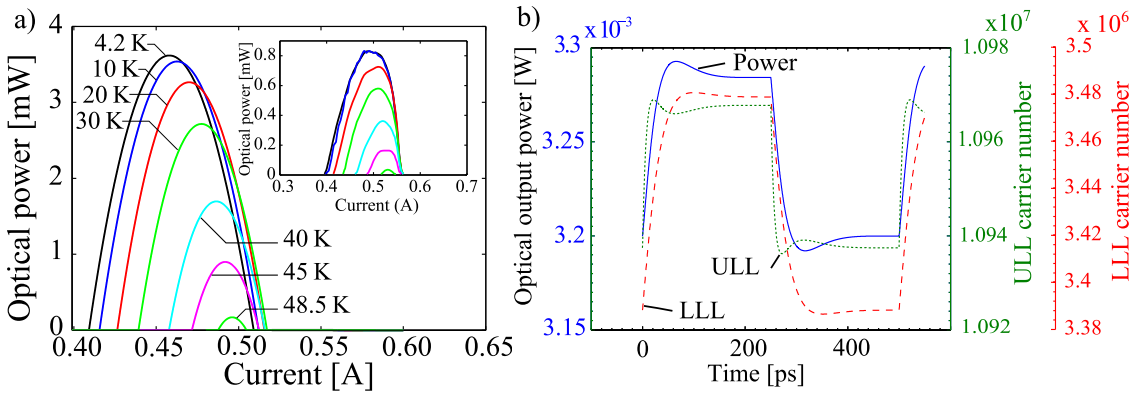

Figure 6.2: (a) Calculated optical output power versus current for a 2.9 THz QCL at different temperatures. Inset shows experimentally measured data with temperatures corresponding the same colours in the main figure. (b) Calculated emitted power and populations over time; a steady state condition is reached after 150 ps. Adapted from joint publication with G. Agnew [117].

ing temperature. However, the rate equation approach used to evaluate the QCL parameters was shown in Chapter 4 to have significant weaknesses due to state hybridisation. Extensive polynomial fitting of the full rate equation output is necessary to obtain input to the reduced rate equation. While this is only necessary once, it is nevertheless beneficial to calculate QCL parameters with a more reliable model such as the density matrix approach. It is noteworthy that reduced rate equations behave intuitively and may be able to capture the dynamics of QCLs under self-mixing. Most significantly, the inclusion of self-heating effects during operation means that it is applicable to QCLs which work under pulsed operation, allowing a feasibility study of SM with QCLs near their limits of high temperature performance.

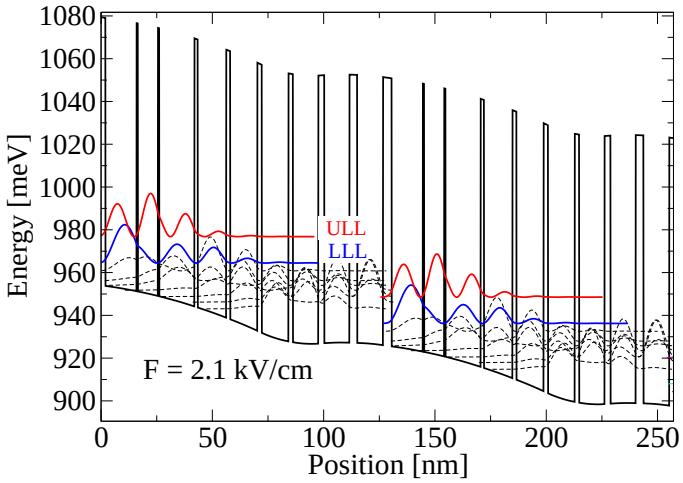

Figure 6.3: Bandstructure and wavefunction plot for a 2.6 THz BTC QCL at an applied field of 2.1 kV/cm.

6.2.2 Density matrix modelling

The DM model described in Chapter 4 is capable of accounting for the effect of light field strength on active region current. This effect occurs as stimulated emission drives current through the device between lasing states. Figure 6.3 shows the wavefunction and bandstructure of the 2.6 THz BTC QCL with 9 states per period at its designed alignment field of 2.1 kV/cm. Lasing occurs between the red (ULL) and blue (LLL) states with fast depopulation of the LLL by a miniband of states lying close in energy. To date, DM modelling of BTC QCLs in materials other than SiGe [73] has not been demonstrated. Figure 6.4 shows the comparison of the experimental and simulated I–V and L–I characteristics assuming cavity losses of 18 cm^{-1} and IFR parameters of Δ=1.3 Å and Λ=100 Å. Also shown are the simulated I–V characteristics assuming a series resistance of 2 Ω applied as described in Chapter 8. Excellent agreement is achieved for the threshold current density, magnitude of the output power, and voltage characteristics. It is important for the following work to

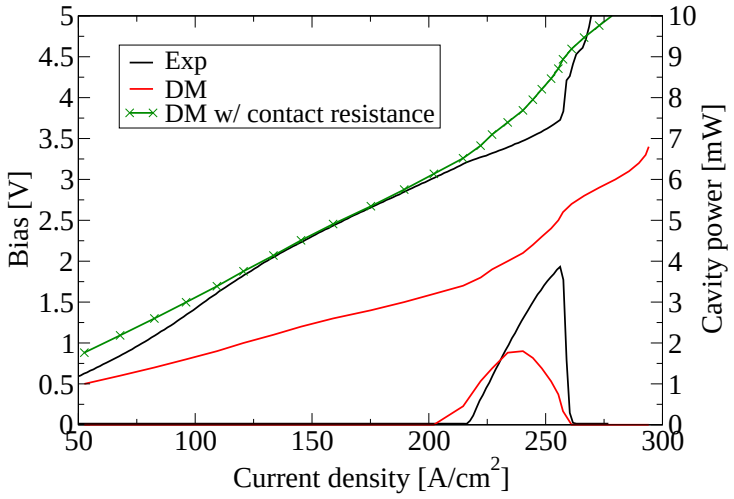

Figure 6.4: Simulated and experimental L–I and V–I data for the BTC device grown and characterised by colleagues at the University of Leeds and shared by P. Dean.

note that the experimental I–V curve exhibits an NDR like feature at $\approx 260\,\mathrm{A/cm^2}$ where voltage current no longer increases with voltage. This is also evident in the modelling results which use the applied field as an input parameter. Above a bias of 4 V (with contact resistance applied) the experimentally measured current does not increase further. This is due to there being no state lying energetically close above the ULL as shown in figure 6.3. As discussed in Chapter 4, NDR features in current-driven QCLs cause oscillations between voltages where current is equivalent to the driving current and this NDR feature prevents the QCL from lasing at this current density. In contrast, the density matrix calculated lasing stops naturally at this current density due to the losses and IFR values chosen.

6.3 Three mirror cavity loss

During operation, the laser cavity field reaches a steady state magnitude where the gain is clamped to the losses of the cavity as discussed in Chapter 4. Typically, the laser cavity and target are treated as a three mirror cavity with its own associated loss (or the threshold gain value) [115]. In a simple picture, if the target reflector (third mirror) is positioned so that it reflects precisely at a node of the emitted standing wave, then the reflected (and reinjected) radiation will be 180 degrees out of phase to the emitted radiation. In the classical wave picture of electromagnetic radiation, waves can interfere constructively or destructively as is the case with light fields with opposite phase interacting. Since it is typically asserted that cavity gain is always clamped to cavity losses, it follows that for a QCL operating with a fixed applied bias, the cavity field strength will decrease when interacting destructively with a field out of phase. This reduction in the magnitude of the cavity light field can be represented by a new cavity loss which varies according to the phase and magnitude of reinjected radiation.

The effect of changing cavity loss on the simulated current and predicted output power is significant. Figure 6.5 (and direct side-on view in figure 6.6) show the effect of changing loss on current density at each applied bias point at 25 K. This shows a gradient in current above the threshold current of 210 $\mathrm{A/cm^2}$ for low to mid values of cavity loss. Increased cavity loss results in higher threshold currents and this is evident from the horizontal grid lines remaining flat at high losses. Separation of grid lines indicates the gradient of the I–V curve along the applied field axis. It was found that above threshold, a change in cavity loss of 1 $\mathrm{cm^{-1}}$ results in a change in cavity current of approximately 0.9085 $\mathrm{A/cm^2}$ around the loss value of 12 $\mathrm{cm^{-1}}$.

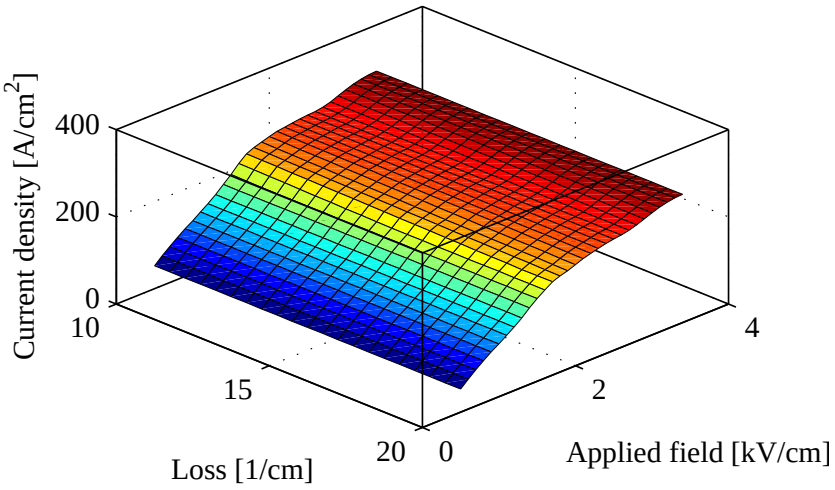

Figure 6.5: Calculated current density for QCL under lasing operation at 25 K. Changing cavity loss changes the threshold gain and lasing power which varies the photon driven current.

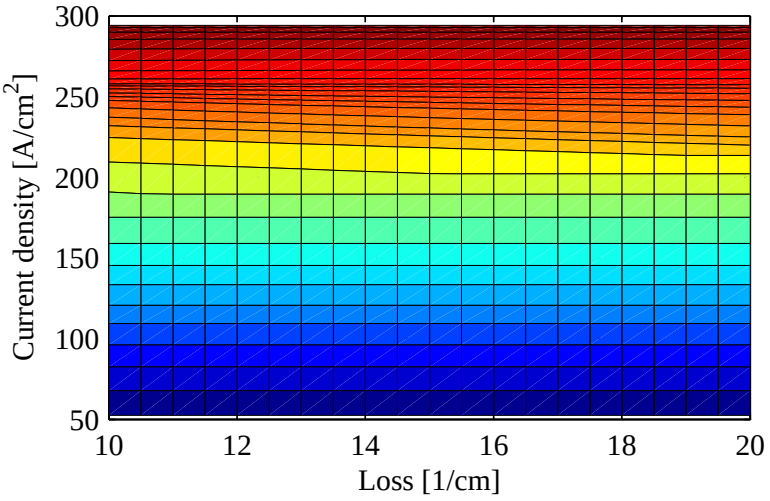

Figure 6.6: Calculated current density versus loss along the applied field axis. At lower losses the cavity power and current density increase.

Changing the threshold gain has a significant effect on the emitted power of the QCL since it changes the required cavity field strength required for clamping. Figure 6.7 shows the calculated emitted power versus cavity loss and applied field. This shows peak output power predicted at 2.1 kV/cm for losses between 10 and 20 cm^{-1}. Peak emitted power is predicted to decrease from 10 mW to 0.5 mW over this range and the threshold applied field increases gradually from 1.7 kV/cm to 1.9 kV/cm.

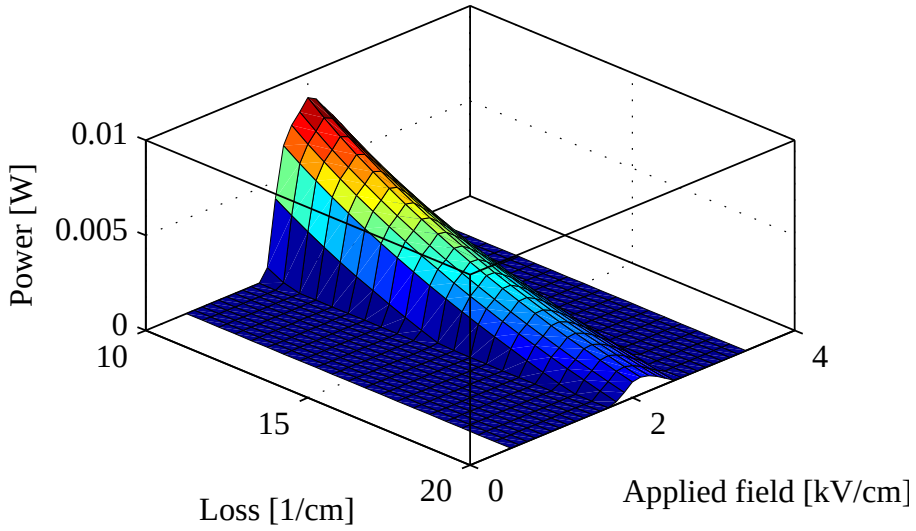

Figure 6.7: Simulated emitted cavity power versus applied field and loss. Peak power is achieved with states aligned at 2.1 kV/cm.

6.4 QCL terminal voltage variations

Self-mixing setups such as those shown in figure 6.1 have a complex combination of standing wave formations for the lasing cavity and three mirror cavity. The QCL cavity with its own lasing cavity field emits radiation from its facet which travels to the target, is reflected and is reinjected to the cavity as shown in figure 6.8. In chopper modulated and oscillating target setups, the changed phase of the returning

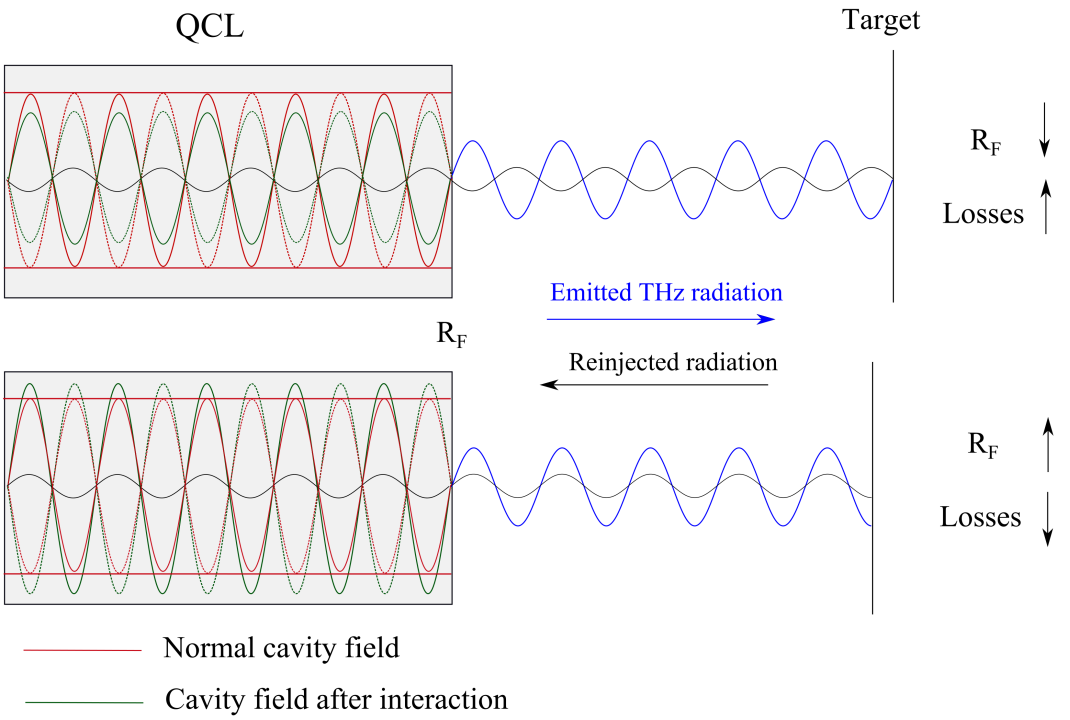

Figure 6.8: Schematic for origin of changing cavity loss for a three mirror system. The resultant cavity field depends on both the magnitude and phase of the reinjected radiation. When constructive (destructive) interference occurs the equivalent system losses decrease (increase).

light field and the cavity field phase interact; this changes the emission frequency of the QCL so that the field is continuous across the facet boundary. Typically this is solved for using the excess phase equation in the Lang-Kobayashi approach [111]. This is neglected here for simplicity and it is assumed that only the classical interaction of waves occurs. However, it is shown that excellent agreement between simulations and experimental work is achieved for steady state conditions with this approach. For an example oscillating target setup, the radiative power, P, emitted

from the laser back facet will vary according to:

$$P(\tau_{\text{ext}}) = P_0 \left[1 + m\cos(\tau_{\text{ext}})\right] \tag{6.2}$$

where P_0 is the unperturbed (free-running) laser power and m is an amplitude factor proportional to $\epsilon\sqrt{R_{\text{ext}}}$ [113]. ϵ is the coupling-efficiency factor to account for optical losses such as external cavity attenuation, and mismatch between emitted and reflected radiation.

Equation (6.2) states that at points where the cosine function equals 1, the maximum change in power will occur $(\Delta P)_{\max} = mP_0$. For weak feedback, this will be a factor of a few percent change. Assuming trial values of $R_{\text{ext}} = 0.25$ for an aluminium target such as the plate used in Ref. 113 and $\epsilon = 0.1$ yields a peak variation of $\approx 5\%$ due to interaction with reinjected radiation. While these choices are arbitrary as the coupling of reinjection back into the cavity is unknown here experimentally, it is typically accepted that several percent of emitted power is reinjected depending on the feedback strength regime. To obtain the experimental peak change in power/voltage for chopper modulated systems, the target position is varied to find the position where the self mixing signal is largest at each current point.

Figure 6.9 shows the interpolated data for applied field values (without any contact resistance effect) for desired current density and cavity loss values. The underlying concept of this lookup table is to find the required device bias and photon field strength combination that gives the QCL drive current. For example, if the virtual cavity loss increases, then threshold gain increases and power subsequently decreases. This implies reduced photon driven transport and a different (typically higher) bias field across the active region to supply the correct current which is held constant. For the case where the cavity loss decreases then the opposite is true and typically the required bias is reduced. To find the cavity loss value required for a given cavity power including feedback, a similar lookup table is produced at

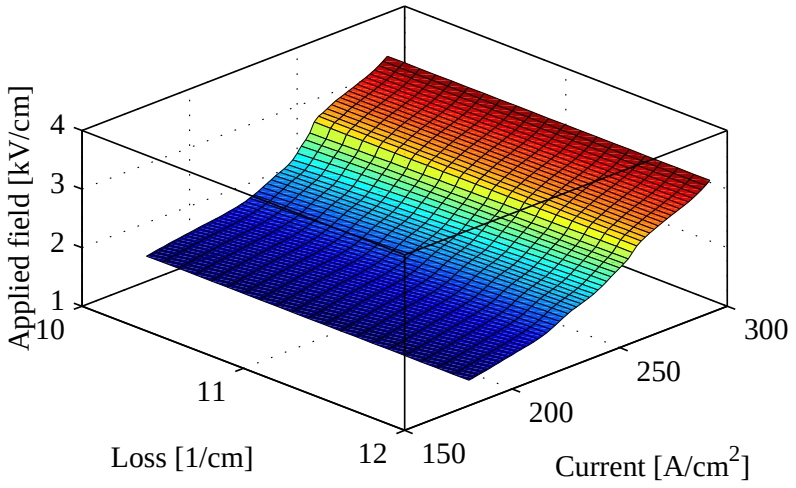

Figure 6.9: Calculation of applied field values necessary for a QCL drive current and loss value for the BTC structure at 25 K.

each current drive density. The assumed free-running loss value and current density parameters are used first to establish the loss value after reinjection, which is then used with current density to find the applied field. By finding the difference between free-running QCL bias and the QCL bias under feedback, the self-mixing voltage is extracted as shown in figure 6.10 along with results of the recent experimental device and calculated differential resistance.[1] Reasonable agreement between the magnitude and features of the device are found. By comparing the V_{SM} and calculated differential resistance it is clear these are related. The calculated differential resistance has features very similar to the experimental self mixing voltage signal however the theoretical V_{sm} calculation does not have a similar maximum peak. This is due to the the calculated and experimental QCLs being in different regions of their light output roll-over curve. The calculated L value with the assumed free running loss has almost turned off at the current density where a large V_{sm} peak is

[1]This was achieved with a variation around a reference loss of 12 cm^{-1} which gave the best agreement with experimental V_{SM} measurements. The loss value of 18 cm^{-1} used for figure 6.4 however was fitted for agreement with threshold and cut off current densities.

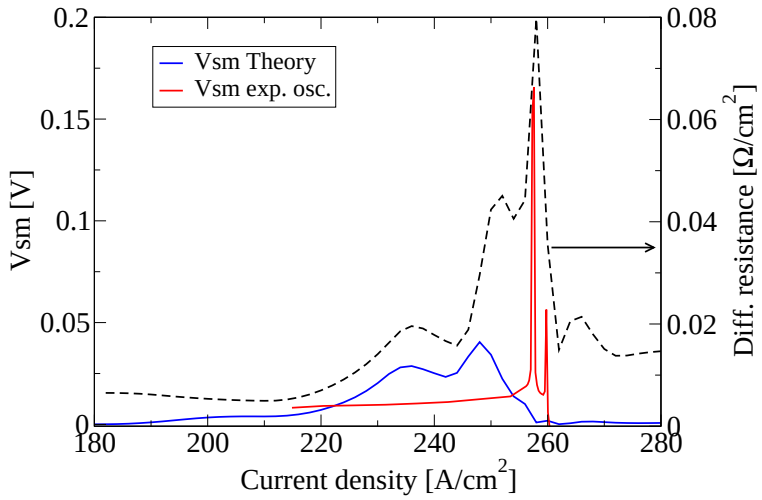

Figure 6.10: Comparison of peak self-mixing terminal voltage signal calculated with the density matrix solver and experimental data provided by colleagues at the University of Leeds. Calculated differential resistance is also shown.

observed experimentally. The change in current and therefore self-mixing signal are then small at this point. Conversely, the experimental QCL cuts off due to the NDR feature where it appears to be near its peak output power. It would be desirable to fit the position of the DM peak light current however this depends on several fitting parameters such as IFR values and waveguide losses. Nevertheless it is shown in the next section that combining these results with the experimental I-V curve can give good agreement with the voltage variation. To summarise, it is proposed that the peak observed experimentally is due to the QCL changing voltage over a larger range to achieve the field required for scattering current and photon driven current to be equal to the drive current.

6.5 Hybrid model - combining DM results with experimental I–V

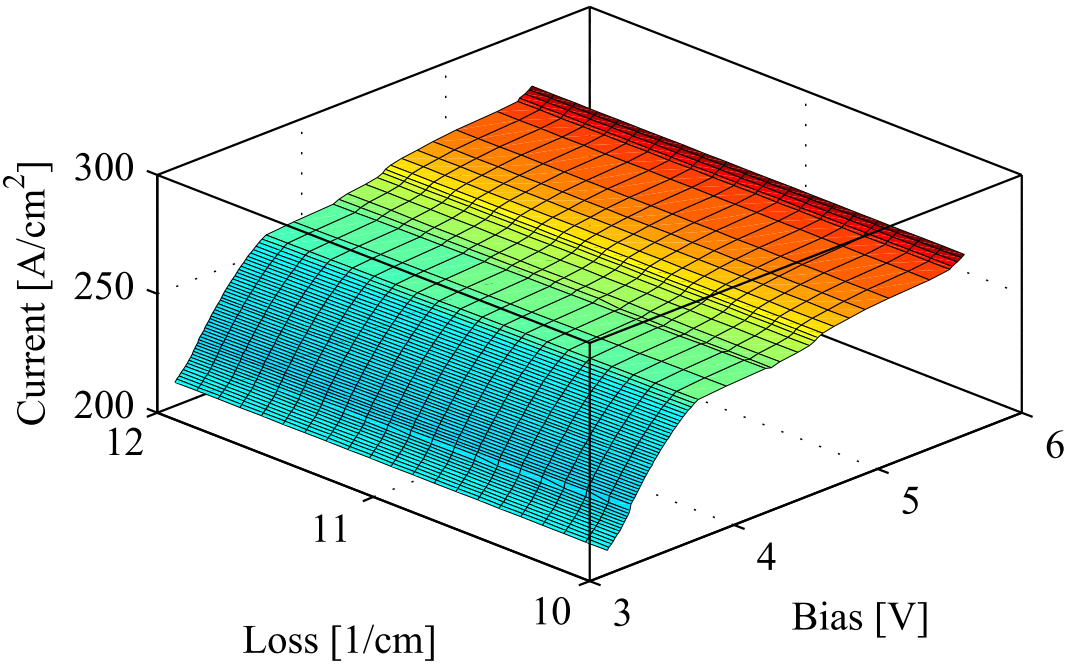

Figure 6.11: Current density versus loss applied to experimentally measured I–V data of the QCL.

The previous section demonstrated how the sensitivity of the QCL at each current point is highly dependent on the local gradient of the I–V curve. Although the carrier transport and light interaction abilities of the DM model can obtain good agreement with experimental data, there will be typically many unaccounted for effects occurring in experimental devices. These can include contact resistance, contact voltage drops, parasitic currents and device heating. Therefore it is desirable to combine the current–light response calculated by the DM model with the actual experimental V–I curve. Over large changes in cavity field intensity the squared dependence of the power will make this approach invalid however the small change

in cavity power allows a linear correlation between power and current. Values of $\mathrm{d}P/\mathrm{d}Loss = -3.8 \times 10^{-4}$ Wcm and $\mathrm{d}J/\mathrm{d}Loss = -0.9$ A/cm were extracted from the DM model for the QCL at 2.1 kV/cm. These gradients were applied to the experimental V–I and L–I curves over a small range of loss values. The magnitude of loss value used here is arbitrary as long as the assumed free-running loss lies reasonably within the range since the applied current gradient is linear. Figure 6.11 shows the raw data with this gradient applied to obtain predicted current density for a changing cavity loss for each applied field.

Figure 6.12 shows the data then interpolated to find applied field points equivalent to each current density and loss values. It can be seen that at lower current densities (< 260 A/cm^2) that the gradient of the applied field change with the loss is small by the grid lines almost parallel with the $y-$ axis. However, at approximately 260 A/cm^2 a large miscut occurs and the gradient of voltage change increases significantly. As in the case of the theoretical work, this is attributed to the field requiring large changes in voltage to acquire alignment of subbands so that scattering current and photon driven current equal the driving current. The unusual characteristic of this experimental device is that the significant plateau of current with respect to voltage is similar to an NDR feature however the QCL continues to lase with current increasing just into the NDR region. Figure 6.13 shows the predicted V_{SM} simulated with this "hybrid" method of combining results of the DM model with the experimental data. This shows the peak self-mixing signal as a function of current for both measurements done with a chopper and an oscillating target. The difference in magnitude for the experimentally measured signal for chopper modulated and oscillating target approaches is attributed to the chopper modulated measurements being done manually. Excellent agreement between the position of the peak signal is obtained indicating that this large peak is related to the I–V curve. The magnitude of the peak also has good agreement assuming a constant 5% reinjection of cavity

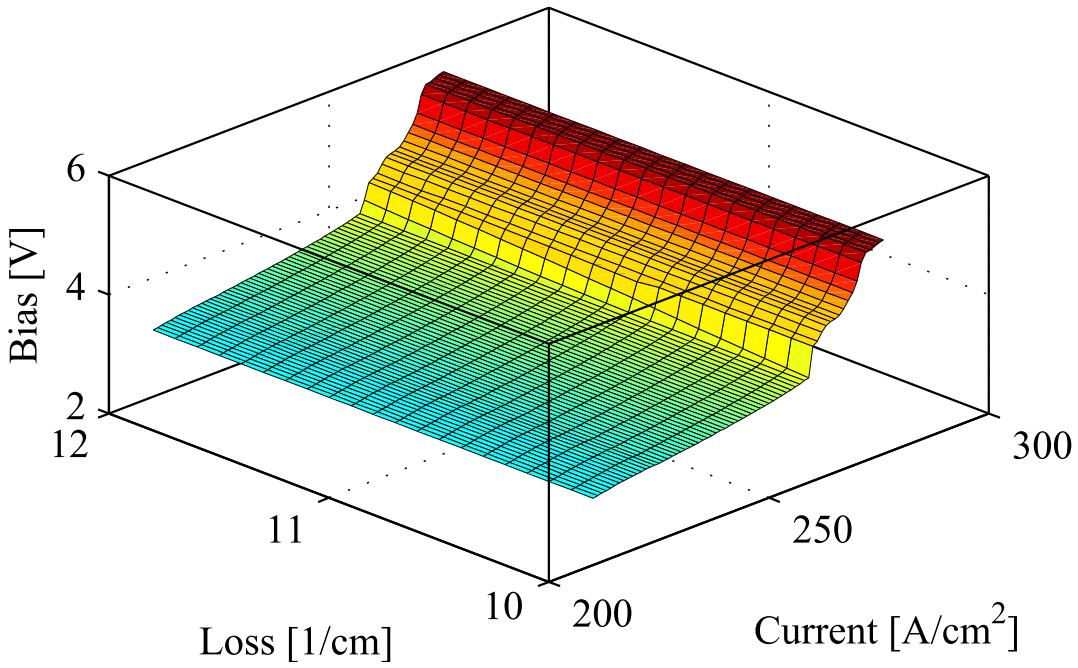

Figure 6.12: Interpolated bias field required for a given loss and drive current using the data presented in figure 6.11.

light. At lower current densities, the simulated V_{SM} is significantly smaller than that measured experimentally. This is likely due to the coupling efficiency of reinjected radiation changing depending on the emitted and reflected power which themselves depend on the current density. Peak output power is achieved at 260 A/cm^2 before the QCL abruptly turns off; it is proposed that the percentage of reinjected light (compared with emitted light) is greatest at this point experimentally.

6.6 Conclusion

In this chapter the usefulness of the density matrix model has been demonstrated by applying it to a THz BTC QCL. Its inclusion of effects of light interaction with the cavity allows the current response of the QCL to be calculated depending on

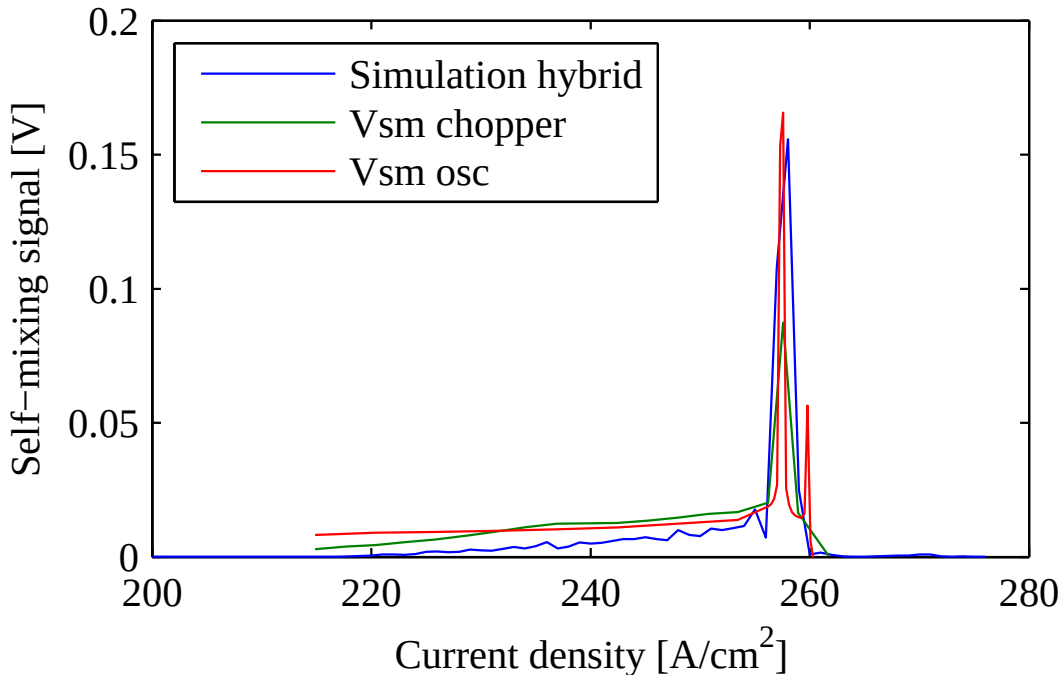

Figure 6.13: Comparison of peak self-mixing terminal voltage signal calculated with the "hybrid" model to experimental data provided by colleagues at the University of Leeds.

a changing cavity loss which the gain is clamped to. Self-mixing interferometry is a promising application of QCLs since it allows the QCL to be used as both a source and detector. By applying the model to this situation, an explanation for the origin of terminal voltage variations is presented for QCLs for the first time. By combining experimental I–V data of a QCL recently characterised by colleagues, excellent agreement is obtained for the magnitude and position of peak self-mixing signal with respect to the QCL drive current. This model could be used to design and evaluate QCLs tailored to have large sensitivities at desired wavelengths.

Chapter 7

AlGaN/GaN intersubband absorption

The characterisation of intersubband absorption is a critical first step toward nitride QCL or QWIP structures. Demonstration of absorption between the discrete energy states requires low defect densities, understanding of the internal electric fields present, and low enough interface roughness that does not broaden the linewidth to a value where peak absorption is weak. To date, it has been demonstrated in both polar and non-polar structures at near-IR and THz wavelengths. This chapter will describe a systematic investigation and comparison with experimental devices grown and characterised by collaborators at Purdue University presented in Ref. 32 and results are based therein.[1] This theoretical work uses the scattering mechanisms discussed in Chapter 3 to establish agreement of simulated linewidth for both ranges of the electromagnetic spectrum.

[1]Additionally, the scattering rate calculations are presented in a conference publication in Ref. [31] as well as the present authors 2012 University of Leeds transfer report.

7.1 Introduction

Nitride absorption at near-infrared wavelengths was first demonstrated in 1999 [13] and subsequent studies [13, 14, 119] have observed a significant blue-shift of the experimental peak energy with calculated subband energies. It was shown in Ref. 17 that the inclusion of many-body effects such as the depolarisation shift, excitonic correction and exchange correlation perturbation are necessary to obtain experimental and theoretical agreement. Intersubband absorption with linewidths of 10–20 % have been shown for transition energies of 600–800 meV [17, 32]. Initial scattering rate calculations in 1.55 µm quantum wells [120, 121] suggested that the fastest intra-subband scattering mechanism is LO phonon scattering. However, only results for intrasubband scattering in the ground state were calculated. It was shown in Chapter 4 that gain due to an inversion between two states is affected by the lifetime of *both* states. This is also true in the case of intersubband absorption, and in the present work it was found that this leads to significantly different predictions for the dominant scattering contributions to the linewidth.

7.2 Intersubband Absorption

The intersubband absorption of a photon with angular frequency ω is calculated by [31, 122]:

$$A_{if}(\omega) = \frac{e^2\omega}{2n\epsilon_0 c}|M_{ij}|^2 \int_0^\infty L(\hbar\omega, \hbar\omega_0, k_t^2) F_{if}(k_t^2) dk_t^2, \tag{7.1}$$

where n is the refractive index, c the velocity of light, ϵ is the vacuum permittivity, $\hbar\omega$ and $\hbar\omega_0$ are the photon and effective absorption energies and M_{ij} is the dipole transition matrix element. F_{if} accounts for the difference in population and is the difference of Fermi-Dirac factors for the two states at wavevector k. L is the

normalized Lorentzian:

$$L(\hbar\omega, \hbar\omega_0, k_t^2) = \frac{\Gamma/2\pi}{(\hbar\omega - \hbar\omega_0)^2 + (\Gamma/2)^2}, \tag{7.2}$$

where Γ is the FWHM broadening of the absorption spectra. $\hbar\omega_0$ has an in-plane wavevector, k_t, dependent component and includes the effects of non-parabolicity in the transverse direction. This introduces a small broadening depending on the electron distribution within the subband. The transition energy between two subbands at a particular wavevector $\hbar\omega_0$ becomes [122]:

$$\hbar\omega_0 = E_{0f} - E_{0i} + \frac{k_t^2\hbar^2}{2m_{if}}, \tag{7.3}$$

where m_{if}^{-1} is the difference of reciprocal in-plane masses $m_{if}^{-1} = m_{||f}^{-1} - m_{||i}^{-1}$ with $m_{||}$ having a different change than the perpendicular case, i.e. $m_{||}^*(E) = m^*[1 + (2\alpha' + \beta)(E - U)]$ [38]. The Schrödinger-Poisson and absorption calculations were done using two values of non-parabolicity α values (0.3 and 0.6 eV^{-1}) reported in literature [17, 122], however it was found that $\alpha = 0.3\,\text{eV}$ gives better agreement with experimental values of absorption energy. The quantum well material GaN value of β was taken as 0.049 eV^{-1} [122].

7.3 Absorption broadening mechanisms

The incoherent scattering processes discussed in Chapter 3 will affect state lifetimes which introduce an energy broadening. The lifetime, τ_{broad}, used to determine lifetime broadening is given by [64]:

$$\frac{1}{\tau_{\text{broad}}} = \frac{1}{2\tau_i} + \frac{1}{2\tau_f} + \frac{1}{\tau_{ii}} + \frac{1}{\tau_{ff}} \tag{7.4}$$

where τ_i and τ_{ii} are the the inter- and intrasubband scattering lifetimes, respectively of state i. In addition to homogeneous lifetime broadening, the absorption spectra will also be broadened by the presence of wells with varying thickness. These well

fluctuations in the x–y plane cause energy separations to fluctuate and for the total absorption to be broadened accordingly. At high doping densities subband populations increasingly occupy high subband wavevectors where non-parabolic effects become apparent. Noting that photon interactions are strictly vertical, the difference in energy between different states increases with increasing wavevector. While this introduces a broadening effect, it is negligible during the absorption integral for even the high doping densities observed here. The scattering rate calculations used in this chapter were completed with the integral step numbers of $nk = 15$, $n\Theta = 15$ and $nq = 15$ for the wavevector, scattering angle, and scattering magnitude respectively to reduce computational time.

7.4 Many-body effects

At high carrier densities, many-body effects can alter the position of the absorption peak energy significantly due to interactions beyond the electrostatic potential and Coulomb scattering. The exchange interaction (an effect due to interaction with identical particles) is included as a perturbation to the ground state E_1 as [17, 31, 32]:

$$\begin{aligned}\Delta E_1^{\text{exch}} = &- \frac{e^2}{2\epsilon_0\epsilon_r}\int_{-\infty}^{+\infty} dz \int_{-\infty}^{+\infty} dz' \int_0^{k_F} \frac{k'dk'}{2\pi}\frac{e^{-k'|z-z'|}}{k'} \\ &\times |\Psi_1(z')|^2|\Psi_1(z)|^2,\end{aligned} \tag{7.5}$$

where ϵ_r is the dielectric constant of the QW material (GaN). The modulus of the in-plane wave vector is given by k' and k_{F} is related to the surface free carrier density, n_s (approximated to be that of the populations in a single isolated quantum well) by $k_{\text{F}} = \sqrt{2\pi n_s}$. Ψ_1 is the ground state wavefunction in the well. The effective resonant absorption energy used by the Lorentzian in Eq. (7.1) is modified from that calculated without many-body effects to [17]:

$$\hbar\omega_0 = \hbar\omega_{12}\sqrt{1+\alpha-\beta} \tag{7.6}$$

where $\hbar\omega_{12}$ is the intersubband transition energy between ground and first excited states. The depolarisation shift, α, introduces a blue-shift to the transition due to resonant screening by the electron plasma, and the excitonic correction, β, causes a smaller transition red-shift due to interaction with the ground quasi-hole which includes correlation effects. These are given by [17, 31, 32]:

$$\alpha = \frac{2e^2 n_s}{\epsilon_0 \epsilon_r e_{12}} \int_{-\infty}^{+\infty} dz \left(\int_{-\infty}^{z} dz' \Psi_1(z') \Psi_2(z') \right)^2, \tag{7.7}$$

where n_s is again approximated as the surface carrier density of the isolated well, and the excitonic correction is calculated as:

$$\beta = \frac{2n_s}{e_{12}} \int_{-\infty}^{+\infty} dz |\Psi_1(z)|^2 |\Psi_2(z)|^2 \frac{\partial V_{xc}[n(z)]}{\partial n(z)}, \tag{7.8}$$

$V_{\mathrm{xc}}[n(z)]$ is calculated as a function of the spatially dependent 3D carrier density $n(z)$ given by Eq. 2.19 as:

$$V_{\mathrm{xc}}[n(z)] = -\frac{2}{r_s} \left(\frac{9}{4\pi^2} \right)^{1/3} \frac{e^2}{8\pi\epsilon_0\epsilon_r a^*} \times \left[1 + 0.7734 \frac{r_s}{21} \ln\left(1 + \frac{21}{r_s} \right) \right], \tag{7.9}$$

with dimensionless parameter $r_s = \sqrt[3]{\frac{3}{4\pi (a^*)^3 n(z)}}$ and the effective Bohr radius $a^* = \frac{4\pi\epsilon_0\hbar^2}{m_0 e^2} \frac{\epsilon_r}{m^*/m_0}$ [17, 31, 32].

7.5 Polar GaN near-IR absorption

The large energy spacing required for near-IR wavelength transitions offers some advantages over THz spacings since intersubband scattering is expected to be slow even at high temperatures. However, it requires very narrow well widths (around 3 nm compared with 6 nm for THz absorption). The devices investigated in this work were grown and characterised at Purdue University, USA and modelled in collaboration with the author [32]. These devices were grown by MBE on free-standing GaN substrates with dislocation densities of the order of $1 \times 10^6\,\mathrm{cm}^{-2}$. They

consist of 15 repetitions of a 26 Å $Al_{0.18}Ga_{0.82}N$ barrier/26 Å GaN well structure. This study included a range of growth variations, however the following scattering rate investigations are comparable to samples D, E-1, and E-2. These samples vary only the position of the well delta doping which is predicted not to be ionised in simulation, and therefore should be equivalent. The large difference in observed superlattice absorption FWHMs was attributed to the growth pause necessary for delta doping improving AlGaN/GaN interface quality. The superlattice structure was grown on top of an undoped GaN buffer layer and capped with a 2.6 nm GaN layer.

7.5.1 Calculation of absorption bandstructures

Bandstructure calculations were calculated with the Fermi energy pinned to half the bandgap below the GaN cap bandedge. This pinning level was suggested in Ref. 123 to be due to Al dangling-bonds on the Al-polar (0001) surface for large alloy fractions. The practical effect of this is negligible as the system will converge to a similar bandstructure for most wells irrespective of the position of the Fermi-level. Only the unpopulated wells near the surface of the device will be affected, as the field required to have no voltage drop across the device varies. Each iteration of the Schrödinger-Poisson loop was damped by 99.9 % such that only 0.1 % of the newly calculated Poisson potential was added to the conduction band potential. This is necessary for a stable convergence toward a steady state bandstructure due to the large internal fields. In the first S–P iteration (shown in figure 7.1(a)), the bulk/superlattice interface lies far below the pinned Fermi energy, causing the first several wells to have a large sheet density with carriers donated from the intended doping profile. Without damping, this large sheet density will cause a large local Poisson potential pushing these wells well above the Fermi energy. Subsequent iterations will oscillate between these two situations; however with damping the Poisson

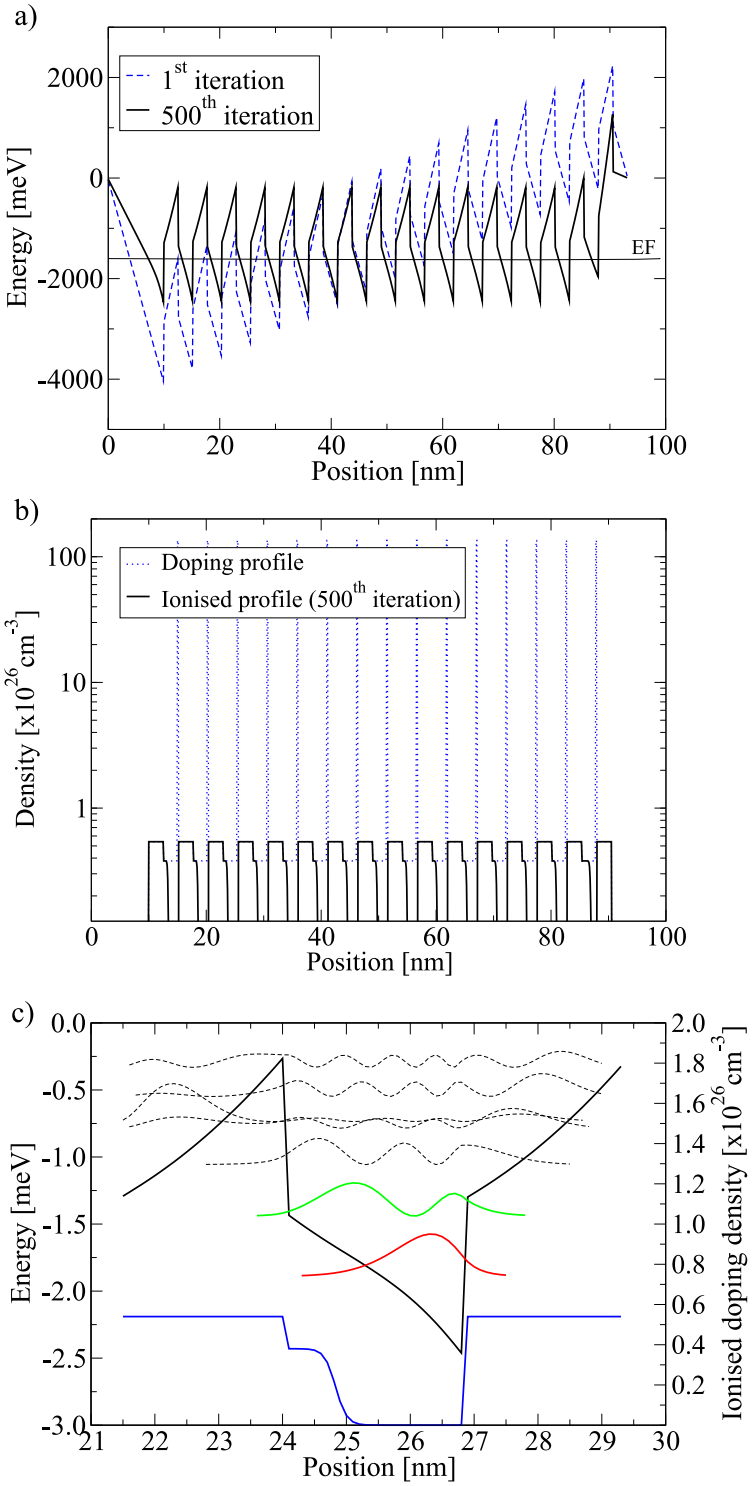

Figure 7.1: (a) Initial and converged bandstructure calculated for near-IR samples described in Ref. [32]. (b) As grown doping profile and ionised doping profile predicted by simulation. (c) Bandstructure and wavefunction plot for one well of the structure. Also shown is the ionised doping profile to show proximity of ionised impurities and wavefunctions.

potential will gradually converge to a steady value which can be combined with the conduction band potential without fields. Figure 7.1(b) shows how this converged bandstructure leads to only partial ionisation of the dopants given to the well as they lie below the system Fermi energy. It is found that all of the barrier dopants are ionised, while only the states lying at the very left of each triangular well are partially ionised, with no ionisation of the delta doping whether it is placed at either the middle or end of the well. Figure 7.1(c) shows the confined wavefunctions for one complete well and the ionised doping profile. Due to the high doping densities of nitride absorption structures, it is expected that the Coulombic interactions (impurity and electron–electron scattering) will contribute significantly to the linewidth via lifetime broadening [17]. Assuming nominal layer thicknesses, the energy difference between ground and first excited states (ΔE) is 478.8 meV (without correcting for many-body effects) while the experimental peak is 654 meV for Sample D. Including the exchange interaction perturbation this becomes 608.37 meV, and with excitonic and depolarisation shifts this becomes 675.58 meV in reasonable agreement with experiment.[1]

Broadening was estimated by calculating the scattering rates for the ground and first excited states due to the mechanisms described in Chapter 3. Table 7.1 shows the relative contribution of each mechanism for the device with the intended well width and doping density. The lowest experimental linewidth value for this structure measured in Ref. [32] was 87 meV. Intrasubband scattering due to ionised impurities and carrier–carrier scattering is found to be significant in line with what is expected for such highly doped structures in the next section. Interface roughness was not calculated in all of the investigations in this chapter since it is a parameter that varies between samples. Calculations for this device using IFR parameters of Δ=2.8 Å

[1]These values were calculated by the present author whereas the similar values presented in Ref. [32] were calculated with *nextnano3* [124] by C. Edmunds at Purdue University, USA.

Scattering mechanism	Impurity	e-e	ADS	e-LO	e-AP	Total
Broadening (meV)	99	0.1	0.20	2.5	0.10	102

Table 7.1: Homogeneous broadening contributions in meV to absorption linewidth from impurity scattering, e–e=electron–electron scattering, ADS = alloy disorder scattering, e-LO longitudinal-optical phonon scattering, e-AP = acoustic phonon scattering

and Λ=100 Å give scattering rates of $W_{1,1} = 8.25 \times 10^{13}\,\mathrm{s}^{-1}$, $W_{1,2} = 3.06 \times 10^{-3}\,\mathrm{s}^{-1}$, $W_{2,1} = 1.10 \times 10^{3}\,\mathrm{s}^{-1}$ and $W_{2,2} = 8.13 \times 10^{15}\,\mathrm{s}^{-1}$ due to interface roughness. In Chapter 4 intrasubband IFR scattering was not included in the linewidth calculation due to correlation of interfaces and this appears to be a reasonable conclusion here as broadening would be excessive. While intrasubband scattering due to impurity scattering may also reduce its contribution to the linewidth, QCL simulations without dephasing appear to overestimate the gain suggesting that it is reasonable to include the effect of intrasubband impurity dephasing on the linewidth.

7.5.2 Effect of well width variation

Variation of well width in intersubband devices affects energy separation, scattering rates, and in the case of nitride devices, the internal electric field strength. Consequentially, the extent of ionisation of dopants in the well is also affected. Energy separation and linewidth calculations were repeated for the initial structure above and the GaN well width varied from 10 Å to 100 Å. Figure 7.2 shows how the predicted position of peak absorption energy decreases with increasing well width. The increasing contribution by many-body effects is explained by the changing electric fields causing more of the well material to be above the Fermi level. This increased ionisation increases the overall carrier density that contributes to many-body perturbations. Exact agreement of the peak absorption energy can be achieved with a

well width of 29 Å rather than the intended 26 Å (over 1 ML larger) and it is possible that agreement can also achieved with other variations of the growth parameters, e.g. barrier height, doping level, and barrier width.

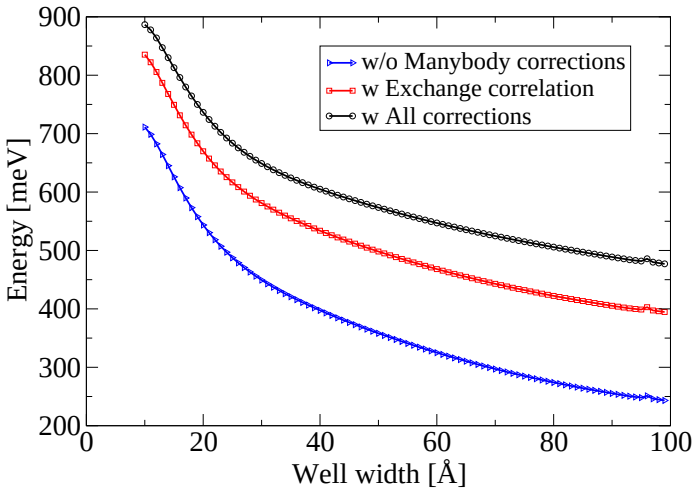

Figure 7.2: Ground state and first excited state energy difference versus well width with and without many-body corrections.

Figure 7.3(a) shows the changing linewidth contribution predicted by the model using Eq. (7.4) with varying well width. The dominant impurity contribution is found to oscillate with increasing well width as the interaction of changing wavefunction overlap and doping profile vary. The magnitude of the oscillation is large, especially for narrow wells which is as expected due to the increased sensitivity of subband confinement with these widths. As well width increases beyond 90 Å the general trend is a decreasing impurity scattering contribution as well ionisation and spatial overlap with the ionised donors decreases. Alloy disorder scattering is predicted to decrease with increasing well width which is an intuitive result as state wavefunction overlap with disorder in the barriers decreases. The slight decrease in LO phonon related scattering can be explained by a changing form factor for

initial and final states, as well as an increasing population in the upper subband introducing final state blocking.

Figure 7.3(b) shows the calculated broadening with the lifetime contribution only from the ground and first excited states of the well, i.e:

$$\frac{1}{\tau_{\text{broad}}} = \frac{1}{2\tau_i} + \frac{1}{2\tau_f} \tag{7.10}$$

The substantially lower predicted linewidths indicate that the majority of the scattering responsible for broadening in Figure 7.3(a) is due to intrasubband scattering. Also noteworthy is that LO phonon emission is expected to be the dominant contribution to broadening in line with that reported in Ref. 121. This is an intuitive result as the subband separation does not allow fast scattering by elastic mechanisms. Noting the different y-axis scales between Figure 7.3(a) and Figure 7.3(b), it is the intrasubband form of LO phonon absorption and acoustic phonon scattering that contribute most to linewidth calculated with Eq. (7.4). Small variations from the trend of LO phonon emission broadening are attributed to the relatively low integration resolution used to calculate the scattering rates rather than a convergence issue of the bandstructure since some other mechanisms are unaffected.

Finally, to illustrate the effects of including the well ground state only, i.e:

$$\frac{1}{\tau_{\text{broad}}} = \frac{1}{2\tau_i} + \frac{1}{\tau_{ii}}, \tag{7.11}$$

figure 7.3(c) shows the calculation contributions versus well width. One difference here is that intrasubband carrier-carrier scattering is now included in the calculation. While this value is now comparable to the experimental linewidth, it is important to note that this approach neglects the broadening contribution from the final absorption subband.

Figure 7.4 shows the dipole matrix element and sheet density versus well width. The dipole matrix element is shown to smoothly increase from -0.4 nm to 0.7 nm as the overlap of upper and lower absorption states vary; this will lead to a dip on

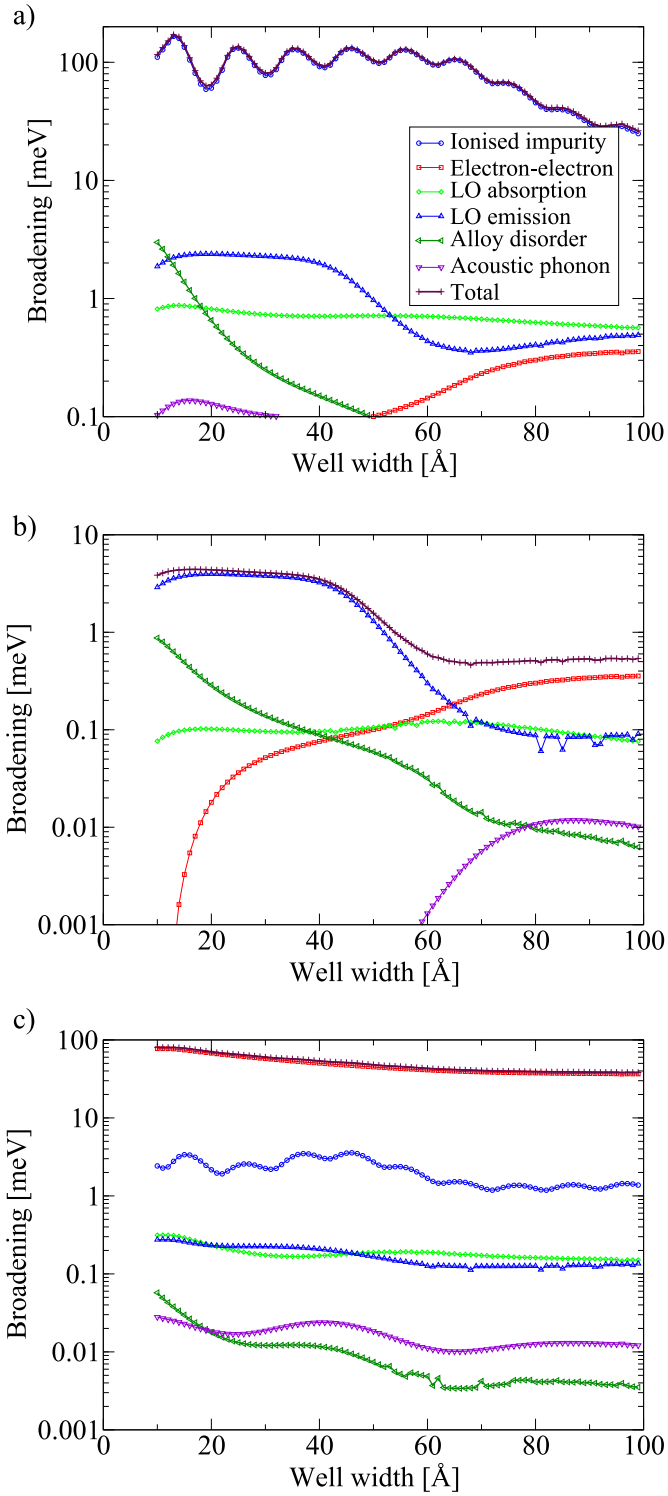

Figure 7.3: Homogeneous lifetime contributions from different scattering mechanisms versus well width using different expressions for broadening. (a) includes inter- and intrasubband scattering contributions from both states (Eq. 7.4), (b) includes intersubband scattering only (Eq. 7.10) and (c) includes inter- and intrasubband scattering for the ground state only (Eq. 7.11).

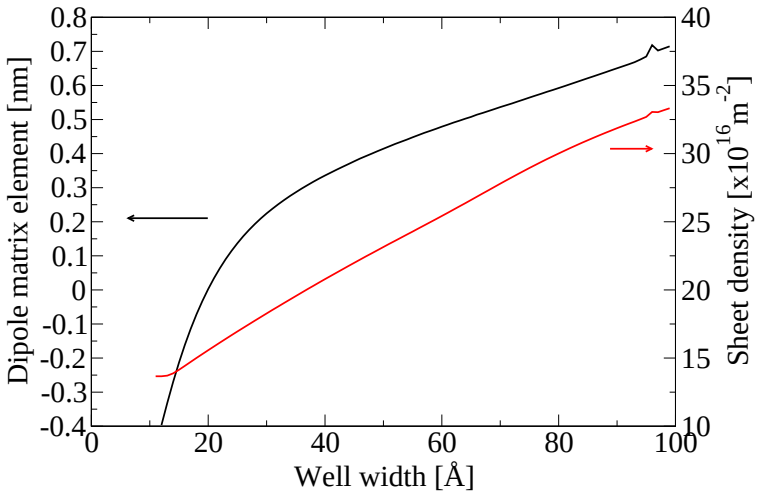

Figure 7.4: Dipole matrix element and subband sheet density versus well width. Increasing well widths lead to a larger proportion of the well doping being ionised leading to higher subband densities.

absorption which is proportional to the square of the dipole matrix element. The sheet density is shown to increase from $\sim 13\times10^{16}\mathrm{m}^{-2}$ to $\sim 33\times10^{16}\mathrm{m}^{-2}$ due to the increasing degree of well ionisation discussed previously which leads to the varying contribution from many-body effects. Ionised impurity does not increase accordingly since the widening well reduces wavefunction overlap with the ionised dopants at the beginning of the well.

7.5.3 Effect of barrier doping variation

Figure 7.1(b) and (c) show that only the barrier dopants are significantly ionised in these absorption structures. While MBE growth is capable of accurate and high quality growths, the implantation of active dopants may differ from the intended doping density. Figure 7.5 shows the calculated transition energy and energies in-

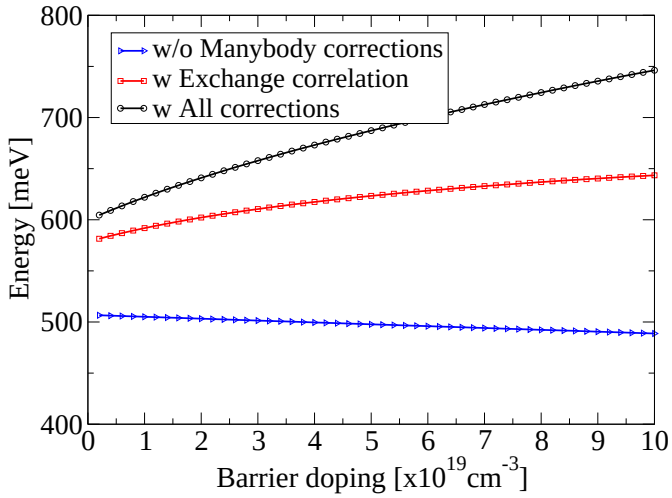

Figure 7.5: Calculated absorption energies for varying barrier doping level. Increasing doping causes a greater contribution from many-body corrections explaining the blue-shift of experimental peak absorption energy with that calculated without corrections.

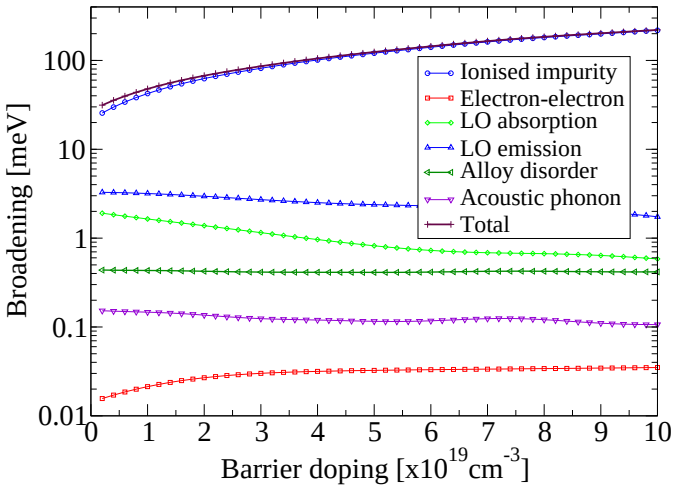

Figure 7.6: Homogeneous lifetime contributions from different scattering mechanisms versus barrier doping.

cluding many-body corrections versus doping density. The calculated energy without corrections is found to decrease slightly with increasing doping density. This is attributed to the ionised donors reducing the barrier potential which reduces confinement of the absorption subbands. The magnitude of the exchange correlation perturbation increases slightly with increasing doping density, however the increase is most significant for the combined depolarisation and excitonic corrections. Figure 7.6 shows how the increasing doping density leads to increasing scattering due to electron-electron and ionised impurity scattering. The experimental linewidth could be matched theoretically with a doping density of $3.2\times10^{19}\text{cm}^{-3}$ instead of the intended $3.8\times10^{19}\text{cm}^{-3}$ value representing a modest 15 % variation.

7.5.4 Effect of temperature variation

Figure 7.7 shows the effect of temperature on the calculated intersubband absorption linewidth. The total linewidth is not expected to change significantly as intrasubband impurity scattering is relatively temperature insensitive. LO phonon emission and absorption processes increase with temperature due to them being boson processes.

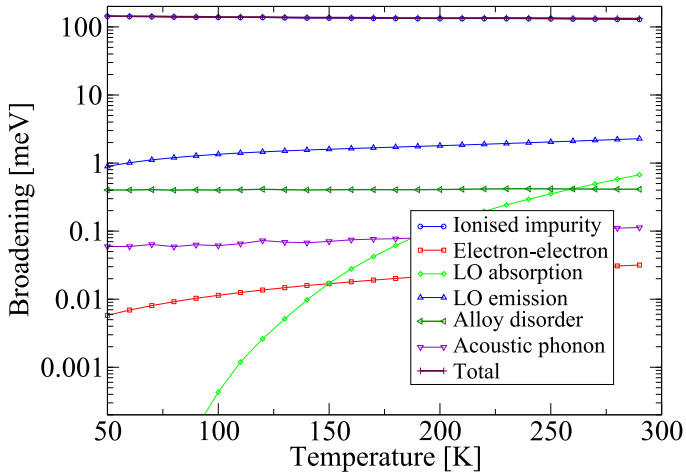

Figure 7.7: Homogeneous lifetime contributions from different scattering mechanisms versus lattice temperature. While phonon mechanisms are highly dependent on temperatu g, is relatively insensitive to

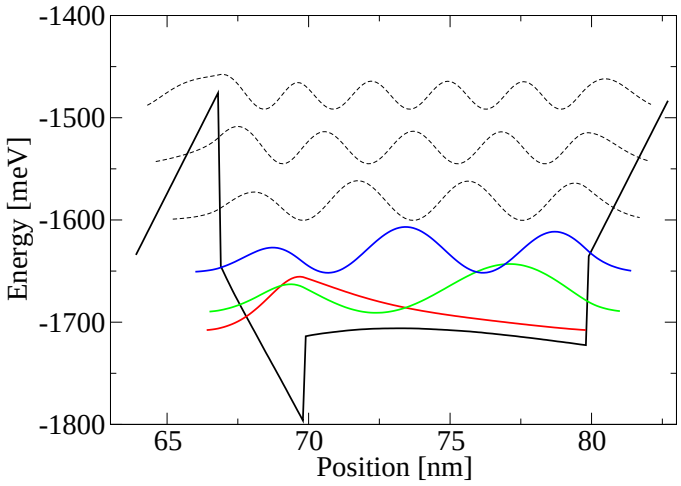

Figure 7.8: Bandstructure and wavefunction plot for the structure presented in Ref. 125. The 10 nm step well is used to achieve a flat band potential that allows smaller energy gaps.

7.6 Absorption in THz structures

THz absorption in $Al_xGa_{1-x}N$/GaN QWs was first demonstrated by Machhadani *et al.* in 2010 [125]. This work used optimised layer widths and a step barrier to achieve a flat bandstructure so that subband separations could be controlled. The sensitivity of this structure to experimental design fluctuations such as step barrier alloy content led to the development of a more robust design in 2013 [126]. In addition to the demonstrations of absorption in polar GaN, THz absorption has also been demonstrated in non-polar m-plane structures by Edmunds *et. al* [127]. This section investigates the linewidth contributions as in the previous section but for the THz absorption structure described in Ref. 125.

The bandstructure and wavefunctions for this design are shown in figure 7.8. The structure consists of a superlattice of QWs with a 3 nm $Al_{0.05}Ga_{0.95}N$ barrier, a 3 nm GaN well and a 10 nm $Al_{0.1}Ga_{0.9}N$ step barrier. Additionally, a similar structure but with a 15 nm step barrier was also grown. The GaN well were doped to $1\times10^{19}\text{cm}^{-3}$ and $5\times10^{18}\text{cm}^{-3}$ respectively [125]. The experimental peak absorption energy was reported as 17.4 meV for the 10 nm structure and 8.7 meV for the 15 nm structure at 4.7 K. The corresponding absorption linewidths for these structures were 9.93 meV and 2.98 meV. Sample A with the 10 nm step well was used as the reference structure and the step well width and temperature were varied to investigate their effect on linewidths. The calculated transition energy was found to be 16.6 meV without any many-body corrections. With depolarisation and excitonic corrections this value was found to be 45 meV and with both these and the exchange interaction perturbation the absorption energy is calculated as 55 meV. The applicability of the many-body corrections presented in section 7.4 have been doubted in other works also [127] and are ignored as good agreement has already been achieved. The individual contributions from each mechanism with a step barrier width of 10 nm are shown in Table 7.2 with a lattice temperature of 4.7 K. The total predicted

Scattering mechanism	Impurity	e-e	ADS	e-LO	e-AP	Total
Broadening (meV)	2.91	0.08	0.20	0.33	0	3.32

Table 7.2: Homogeneous broadening contributions in meV to absorption linewidth from impurity scattering, e–e=electron–electron scattering, ADS = alloy disorder scattering, e-LO longitudinal-optical phonon scattering, e-AP = acoustic phonon scattering

is 3.32 meV which is much lower than the 9.93 meV measured experimentally in Ref. [125]. This suggests that these structures are perhaps more susceptible to long and short range thickness variations. Intersubband scattering due to short range fluctuations (IFR) is possible in this structure due to the closer energy spacing of the states. The scattering rate model predicts a rate of $W_{IFR,2,1} = 1.023 \times 10^{12}\,\mathrm{s}^{-1}$ which gives a broadening contribution of 0.3 meV i.e, still insufficient to agree with experiment. The discrepancy could then be attributed to long range fluctuations causing broadening, or variations in the parameters such as doping density.

7.6.1 Effect of well width variation

Figure 7.9 shows the variation of absorption linewidth contributions with increasing step barrier width for a lattice temperature of 4.7 K. It can be seen that most scattering rates decrease as the well width increases and this is attributed to a decreasing dipole matrix element. LO phonon emission processes drop suddenly as soon as the well width changes from 25 Å to 30 Å. The energy separations between the ground and excited state at these two points are 96.13 and 83.79 meV respectively and this feature is therefore explained by it crossing the GaN phonon energy of 92 meV. The shift appears sharp due to the low lattice and electron temperatures. Carrier carrier contributions (coming from intersubband events only) increase with increasing well width as the subbands get closer together in energy. Beyond step

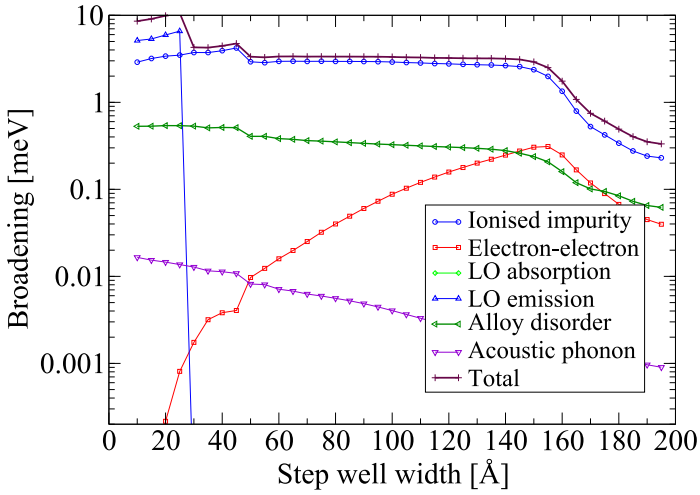

Figure 7.9: Calculated lifetime broadening contributions versus well width for the structure presented in Ref. 125. Ionised impurity scattering is calculated to be the dominant scattering mechanism.

widths of 160 Å the wavefunction overlap of the states decreases as band bending of the step causes wavefunctions to diverge spatially.

7.6.2 Effect of temperature variation

Chapter 4 illustrated how THz structures are heavily affected by increasing lattice temperature. Figure 7.10 illustrates the effect of temperature on the contributions to lifetime for sample A in Ref. 125. The total linewidth is predicted to increase 196 % from 2.8 meV to 5.5 meV from 10 K to 270 K. Experimental measurements of this variation for $Al_xGa_{1-x}N/GaN$ absorption structures have not been reported however the results calculated here may explain why room temperature absorption of THz radiation has not been demonstrated. All scattering rates increase with temperature as electrons move up the carrier subbands. LO phonon emission and

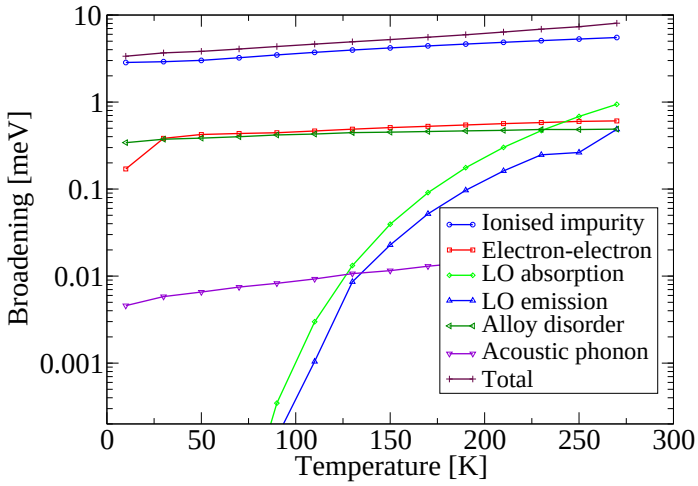

Figure 7.10: Calculated lifetime contributions versus temperature for the THz absorption structure. Only LO phonon scattering processes are affected significantly by increasing temperature.

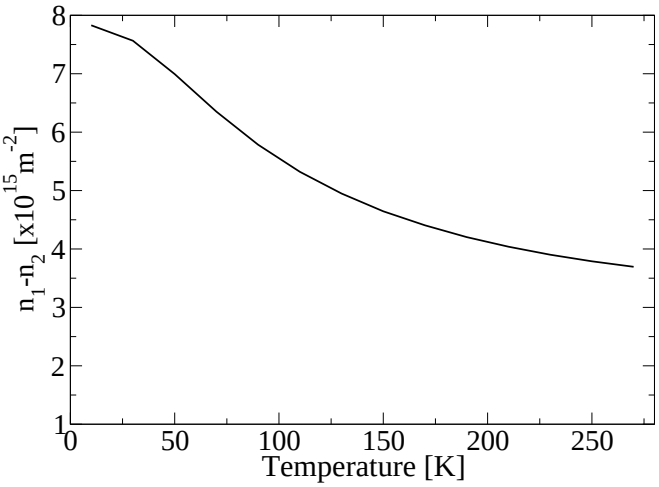

Figure 7.11: Calculated population difference between the ground and excited states in the THz structure.

absorption processes have the most significant increase due to the increasing thermal energy allowing intersubband scattering to increase. Figure 7.11 illustrates that the population difference decreases with temperature as the Fermi level shifts with temperature; this also contributes to the weakening of the absorption magnitude with temperature.

7.7 Conclusion

This chapter has investigated the scattering rate contributions to lifetime broadening of intersubband absorption. Using the scattering rates presented in Chapter 3, the lifetime of electrons in the upper and lower absorption states was calculated. The effect of these on the linewidth calculated with the scheme in Ref. 64 was presented for both near-IR and THz structures. A linewidth of 102 meV was predicted for the near-IR structure investigated in a recent collaboration between C. Edmunds and O. Malis at Purdue University and the present author [32]. The dominant contribution to this was found to be intrasubband scattering due to ionised impurities in the excited state involved in the intersubband absorption. It was also shown that variations in well width, doping and temperature could also be used to account for the remaining discrepancy between theory and experiment. Ideally, the calculated linewidth should be smaller than that measured experimentally so that long and short range interface roughness can also be included. However these are difficult to establish as they depend on the growth quality and the conclusions reached regarding the dominant broadening mechanism are sufficient to improve future devices. Namely, that the doping level and position should be carefully considered so that broadening is not excessive. Reducing the density of, and spatially separating dopants from carrier distributions has been used in Ref. 127, and a linewidth reduction of 40 % was observed. Ionised impurity scattering was also calculated to be

the dominant broadening mechanism for the THz absorption structure reported in Ref. 125 however the agreement of the total linewidth is not as good as in the near-IR case: the linewidth was predicted to be 3.32 meV however the experimentally measured value was 9.93 meV at 4.2 K.

The experimentally measured peak absorption energy of the near-IR structures had a significant blue shift compared to that calculated theoretically. Many-body corrections such as the exchange correlation interaction, depolarisation shift and excitonic correction were shown to give excellent agreement when included. These were shown to vary significantly with the doping density. The validity of these corrections in the far-IR scheme is questioned as the peak absorption energy was calculated to be 16.6 meV without corrections, 55 meV with corrections, and 17.4 meV experimentally.

Chapter 8

Transport in experimental nitride heterostructures

This chapter investigates the electron transport in epitaxially-grown nitride-based resonant tunnelling diodes (RTDs) and superlattice sequential tunnelling devices. The density-matrix model described in Chapter 4 is adapted for RTDs and shown to reproduce the experimentally measured features of the current–voltage curves at different temperatures. These comparisons are completed in collaboration with experimental collaborators at Purdue University, USA who grew and characterised the devices.

Lifetime broadening effects due to dephasing are shown to have a significant influence in the experimental data. Additionally, it is shown that the interface roughness geometry has a large effect on current magnitude, peak-to-valley ratios and misalignment features; in some cases eliminating negative differential resistance entirely in RTDs. Sequential tunnelling device characteristics are dominated by a parasitic current that is most likely to be caused by dislocations, however excellent agreement between the simulated and experimentally measured tunnelling current magnitude and alignment bias is demonstrated. This analysis of the effects of scattering life-

times, contact doping and growth quality on electron transport highlights critical optimisation parameters for the development of III–nitride unipolar electronic and optoelectronic devices.

8.1 Introduction

Resonant tunnelling diodes (RTDs) are the simplest devices in which to explore vertical tunnelling transport and they have undergone extensive experimental and theoretical investigation since the pioneering work by Esaki and Tsu [128]. While they are well studied in arsenide [129] and antimonide [130] materials, measurement in nitrides remains relatively challenging. Initial reports of nitride RTDs [131, 132] demonstrated that an NDR was only observed during the forward I–V bias sweep and was absent during the reverse scan. This was attributed to deep defects which trap charges at AlGaN/GaN interfaces; it was proposed that these lower the barrier height of AlGaN layers and alter transport depending on direction of the applied bias [21, 133]. The existence of defects such as these charge traps and screw dislocations led to the need for systematic verification of the origin of negative differential resistance (NDR) features [22, 134–136] to establish whether resonant tunnelling had actually been demonstrated. Typically this benchmark is the temperature dependence and repeatability of results over several forward and reverse bias sweeps. Recent advances in growth technology such as those discussed in Chapter 2 have reduced threading dislocation densities substantially. These developments have led to repeatable measurements of wurtzite and cubic AlGaN RTDs since 2010 [23, 133, 137–139] and sequential tunnelling devices [140, 141] since 2011.

Sequential tunnelling devices rely on repeated tunnelling and scattering of carriers through up to several hundred periods of a structure in a similar way to the QCL structures investigated in Chapter 4. Sequential transport was first demon-

strated in nitride devices by Sudradjat *et al.* [142] with 20–30 three-well periods of an $Al_{0.15}Ga_{0.85}N/GaN$ structure at low temperature with good agreement between the experimental and predicted subband-alignment voltages. Following this, a thinner structure with 10 periods of a single well and AlN barriers was grown and compared with analytical expressions [141] for current, however it was found that domain formation dominates the I–V characteristics, preventing investigation into the roles of scattering on transport. To date, there has been no detailed theoretical study and comparison of devices which require scattering and tunnelling between several states per period.

Several approaches exist for the modelling of RTD current–voltage characteristics including the transfer matrix [128], Wigner functions [143–145] and non-equilibrium Green's function (NEGF) methods [129]. To date, nitride RTDs have been studied with the transfer matrix approach [146] which assumes purely ballistic (coherent) transport through the double barrier structure, and also by the NEGF approach [147] which is computationally intensive but describes scattering in the presence of coherent transport. Even fewer theoretical results are available for sequential tunnelling transport due to its recent experimental realisation.

In this Chapter, transport modelling for RTDs and sequential tunnelling devices is unified by developing a modified form of the density matrix (DM) approach for RTDs similar to the QCL approach used in Chapter 4. This DM approach was shown to have good I–V and output power agreement with experimental $Al_xGa_{1-x}As/GaAs$ QCLs. By comparing output from the model with state-of-the-art nitride experimental devices, the relative importance of coherent and incoherent transport mechanisms and the effect they have on critical characteristics such as the current peak-to-valley ratio, magnitude of current and high temperature behaviour is shown.

8.2 Resonant tunnelling diodes

Electrons in an RTD travel from a highly-doped emitter region into a double barrier structure with resonant quantised subbands and then on to a collector region. By applying a bias to the device, the quantised states move in and out of alignment with a distribution of carriers in the emitter, causing NDR features in their I–V characteristics.

8.2.1 Preparation of experimental devices

$Al_{0.18}Ga_{0.82}N$/GaN RTDs with 49 Å wells (barriers 24 Å) were grown by collaborators using plasma-assisted molecular beam epitaxy (MBE) on n^{++} GaN substrates, which were grown using hydride vapour phase epitaxy (dislocation density estimated to be less than $< 5 \times 10^6\,\mathrm{cm}^{-2}$) that were supplied by Kyma Technologies [23, 139]. Low Al composition was used to suppress relaxation effects of the strained AlGaN barrier layers during growth/processing and also to minimise electrical breakdown through interaction of the applied bias with polarisation discontinuities. The emitter and collector regions consisted of GaN with silicon doping at a level of $1{\times}10^{19}\,\mathrm{cm}^{-3}$ separated by 20 Å spacer layers from the well structure. After processing into 4×4 µm mesas, the chips were mounted on copper blocks and wire bonded to gold contact pads before measurement in a liquid nitrogen-flow cryostat.

8.2.2 DM RTD model

In the RTD DM model, the device is split into three sections (the emitter, well, and collector) and it is assumed that the barriers are sufficiently thick or tall enough to limit transport to quantum tunnelling only. This is appropriate since incoherent scattering will dominate transport within each section independently. This is similar to how incoherent transport dominates in THz QCLs except for tunnelling across the

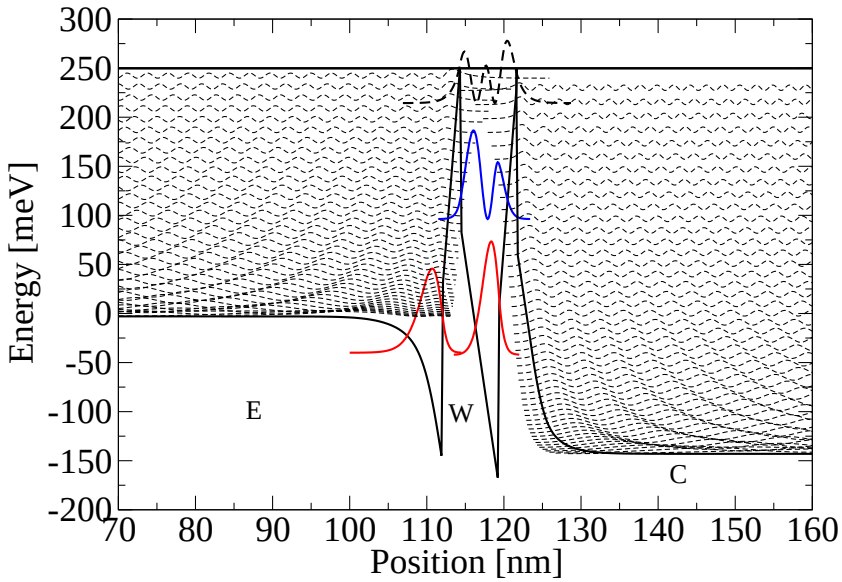

Figure 8.1: Bandstructure and wavefunction plot of an $Al_{0.18}Ga_{0.82}N$ 49 Å RTD. The localised wavefunctions are obtained using a 'tight-binding' scheme with the device split into emitter (E), well (W) and collector (C) regions.

thicker injection barrier. Rather than calculate the bandstructure with the approach used in Chapter 2, the self-consistent Schrödinger–Poisson solver *nextnano3* [124] was used to calculate steady-state conduction band profiles which include the internal electric fields and the effects of contact Fermi level pinning and carrier distributions at each voltage step. The bandprofiles were calculated only once and so the effect of temperature on the ionisation of the heavily doped contact regions is not included here. Localised wavefunctions are obtained in each of the three sections of the device and similar to the QCL tight-binding Hamiltonian, the other sections of the device are replaced with barrier material. The resulting electron probability densities are shown in figure 8.1. These can then be used as basis states for coherent transport through the device. The density matrix is expressed in block form as:

$$\rho = \begin{pmatrix} \rho_{\mathrm{EE}} & \rho_{\mathrm{EW}} & \rho_{\mathrm{EC}} \\ \rho_{\mathrm{WE}} & \rho_{\mathrm{WW}} & \rho_{\mathrm{WC}} \\ \rho_{\mathrm{CE}} & \rho_{\mathrm{CW}} & \rho_{\mathrm{CC}} \end{pmatrix} \tag{8.1}$$

where E, W and C refer to emitter, well and collector states respectively. This is significantly different from the QCL density matrix since RTDs are not periodic structures. The size of the system is therefore $(N_{\mathrm{E}} + N_{\mathrm{W}} + N_{\mathrm{C}})^2$ where N is the number of states for each section. The effect of changing the well width used to create a continuum (and therefore the number of states) on the model is presented in Appendix A. The Hamiltonian for the unperturbed system is:

$$\mathrm{H} = \begin{pmatrix} H_{\mathrm{EE}} & H_{\mathrm{EW}} & 0 \\ H_{\mathrm{WE}} & H_{\mathrm{WW}} & H_{\mathrm{WC}} \\ 0 & H_{\mathrm{CW}} & H_{\mathrm{CC}} \end{pmatrix} \tag{8.2}$$

where the diagonal elements consist of the basis state energies. The off-diagonal elements within the intra-region blocks (EE, WW and CC) are zero since no optical interaction is assumed. Again, similar to the QCL model; the inter-region blocks

(EW, WE, WC and CW) describe the coupling between states and are calculated according to that in Ref. 148. If two energy levels of neighbouring sections couple coherently, electron wave packets can propagate (tunnel) through the barrier from one energy level to another. The coherent transport depends on the strength of the coupling, the detuning from resonance, and the lifetime of the coherence. Dephasing terms are similarly calculated according to Eq. (4.18) in Chapter 4 with contributions from LO phonons, acoustic phonons, ionised impurities and interface roughness scattering for the emitter and collector reservoirs. Since the population of the wells is not known in advance of calculating transport through the structure, its population is set to be an insignificant value. The consequence of this is that mechanisms where intrasubband events are dominant such as electron-electron and interface roughness scattering overestimate the dephasing and are not included here. Additionally, since the DM implementation is tight binding, ionised impurity scattering is not included since the well module is isolated from the other sections. Therefore only phonon transport is included to allow carriers to tunnel into the well excited state, and either tunnel to the collector reservoir or scatter to the ground state and tunnel from there. The intrasubband electron–electron scattering rate was calculated to be approximately $W_{ii} = 1 \times 10^{13}\,\mathrm{s}^{-1}$ at 77 K and this was applied to all subbands in the emitter and collector reservoirs to account for dephasing by this mechanism. Variations on this approximation are presented in Appendix A.

8.2.3 Steady state solution and current

The Tsu–Esaki formalism for current assumes a Fermi–Dirac distribution of carriers in the reservoir regions with Fermi energies pinned to contacts on each side of the device to determine the magnitude of current. However, since the subband quasi-Fermi energy was set before the calculation of scattering rates, the solution for the diagonal ρ elements naturally resembles a Fermi–Dirac distribution in each

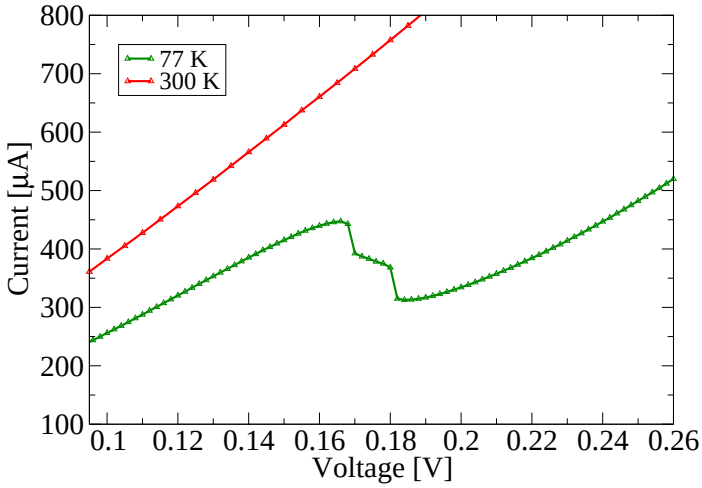

Figure 8.2: Experimental I–V characteristics for the $Al_{0.18}Ga_{0.82}N$ RTD with a 49 Å well and mesa size of 4×4 μm^2 at 77 K. Data shared by O. Mails at Purdue University, USA.

reservoir. Eq. (4.11) (the Liouville equation) in Chapter 4 is solved with $\frac{\partial \rho}{\partial t} = 0$ to find the steady-state emitter and well state populations and coherences using the Armadillo/LAPACK C++ linear algebra libraries [35, 149]. To make the system inhomogeneous, trace conditions for the reservoirs were set so that $\sum_i \rho_{ii} = 1$. Physical quantities such as current density for this device are calculated as in Chapter 4 with a mesa size of 4×4 μm.

8.2.4 Experimental device characteristics

Experimental I–V characteristics at 77 K are shown in figure 8.2. The experimental device shows a resonant peak at 0.165 V with a plateau-like feature between 0.17–0.18 V. Previous experimental measurements of AlGaAs RTDs have also observed plateau features in their I–V characteristics [129, 150]. Several theories for their origin have been proposed including inter-valley interface scattering[151], quantised

interface states [150, 152] or time averaged oscillations [153].

8.2.5 RTD Dephasing time and coupling strengths

Figure 8.3(a) shows the calculated dephasing times over a range of temperatures between states in the emitter reservoir and the ground and first excited states of the quantised well at $V = 0.136\,\mathrm{V}$ where the simulations predicted a peak current. The slight discrepancy with the experimentally measured 0.165 V resonance is attributed to contact resistance effects, as discussed in Chapter 4 and shown later in this section. Dephasing times are found to vary significantly with temperature, decreasing from 94 fs at 6 K to 33 fs at 300 K between the quantised emitter state (at $E = -40\,\mathrm{meV}$) and the ground state in the well. This is due to a significant increase in intrasubband scattering caused mainly by interface roughness and impurity scattering. Dephasing time decreases at higher energies in the emitter reservoir due to the absence of final-state blocking (as they are weakly populated) leading to a faster scattering rate. This absence of final-state blocking causes the dephasing time for continuum states at 6 K to be lower than that at higher temperatures. Additionally, the smaller population of the first excited state in the well contributes to a reduction in the dephasing time for tunnelling in and out of this state.

Initial coupling strengths given by Eq. (4.15) were found to yield currents larger than the experimentally measured values, and a scaling factor of 0.365 was used to account for this overestimation. This is a predictable error since the anti-crossing energy will be overestimated by the tight-binding Hamiltonian and its effect on the PVR is shown in Appendix A. Extraction-coupling strengths were calculated to be larger than emitter-coupling strengths and therefore play a less significant role in determining the vertical electron transport in these devices. Figure 8.3(b) shows the calculated coupling strengths for both EW and CW blocks of the Hamiltonian versus energy. These show that the coupling strength between the quantised emitter state

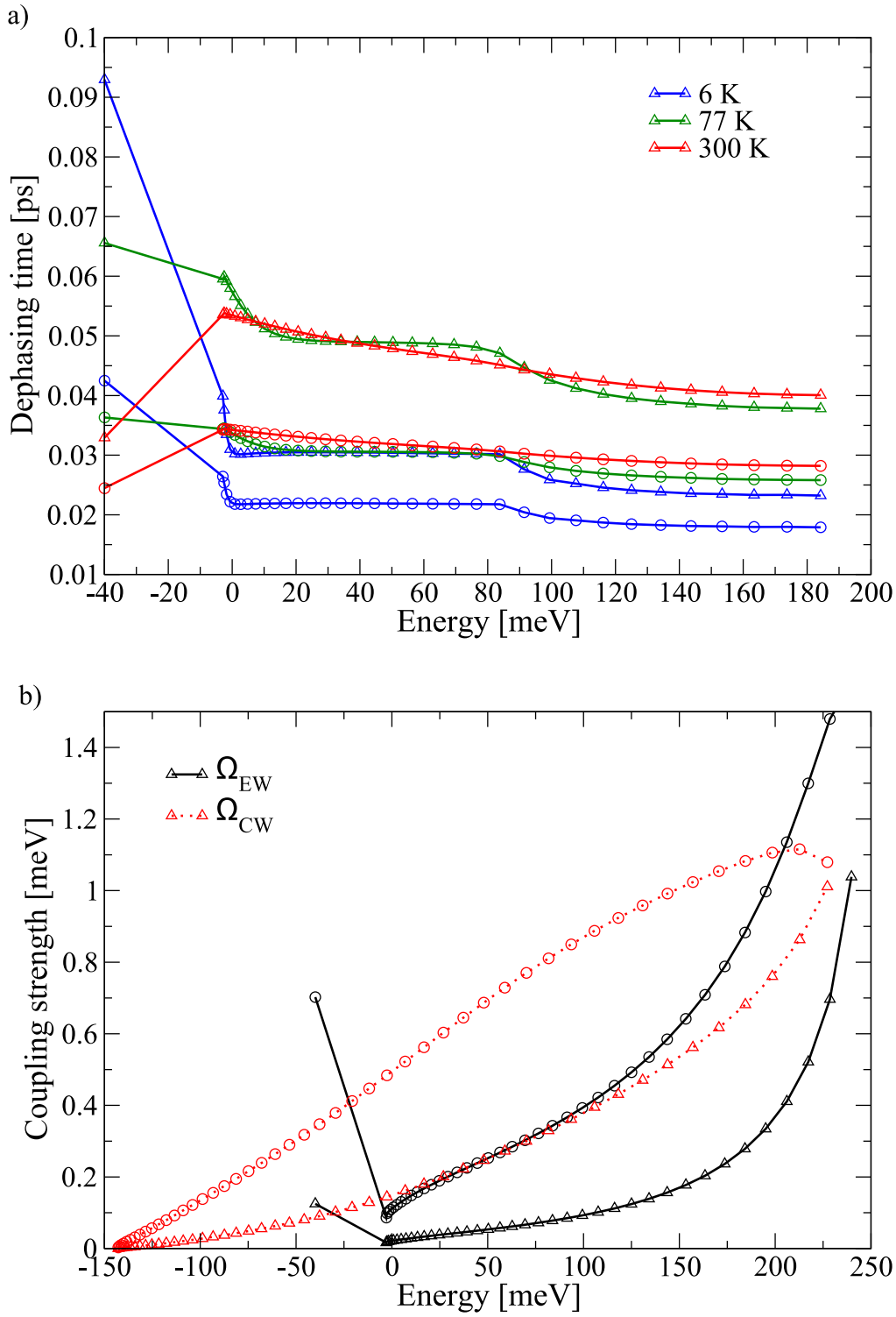

Figure 8.3: Calculated dephasing times (a) and coupling strengths (b) for the quantised emitter state into the ground (triangles) and first excited state (circles) of the RTD well at 0.136 V.

and well states is large due to its localisation at the interface. Coupling strengths between the first excited state in the well and the continuum reservoir states is higher due to the reduced confinement of the triangular barrier potential at these higher energies.

Figure 8.4 shows the calculated off-diagonal block coherences between the emitter continuum states and the ground state of the well at different temperatures. At 6 K the coherence value is largest between the emitter and well ground states at the alignment bias of 0.136 V. Since the density matrix describes the statistical nature of the system and coherence between all states, the interaction of these two states also increases the coherence of all other emitter states with the well ground state (plotted with a smaller range on right pane). The coherences for the emitter states and the well first excited states are also shown to be increasing above 0.15 V as the alignment of this pair increases.

As temperature increases, the magnitude of coherence between the emitter states and the well decreases as dephasing due to scattering increasing and the population spreading over a larger energy range accoring to Fermi-Dirac statistics. At 300 K the coherence between the emitter states and the first excited state of the well (dashed lines in figure 8.4) is comparable to that for the well ground state. This implies that transport occurs from the emitter to the collector via both states and is the reason for no NDR occurring in the simulations at high temperature.

8.2.6 Effect of interface roughness on PVR

Figure 8.5 shows the effect of varying IFR parameters on the peak-to-valley (PVR) ratio calculated by the DM model. Interface roughness has been shown to have a significant effect on transport in unipolar devices [154] and can suppress gain almost completely in tall-barrier QCLs [89]. Figure 8.5 illustrates that increasing the roughness height or correlation length decreases the PVR by increasing dephasing.

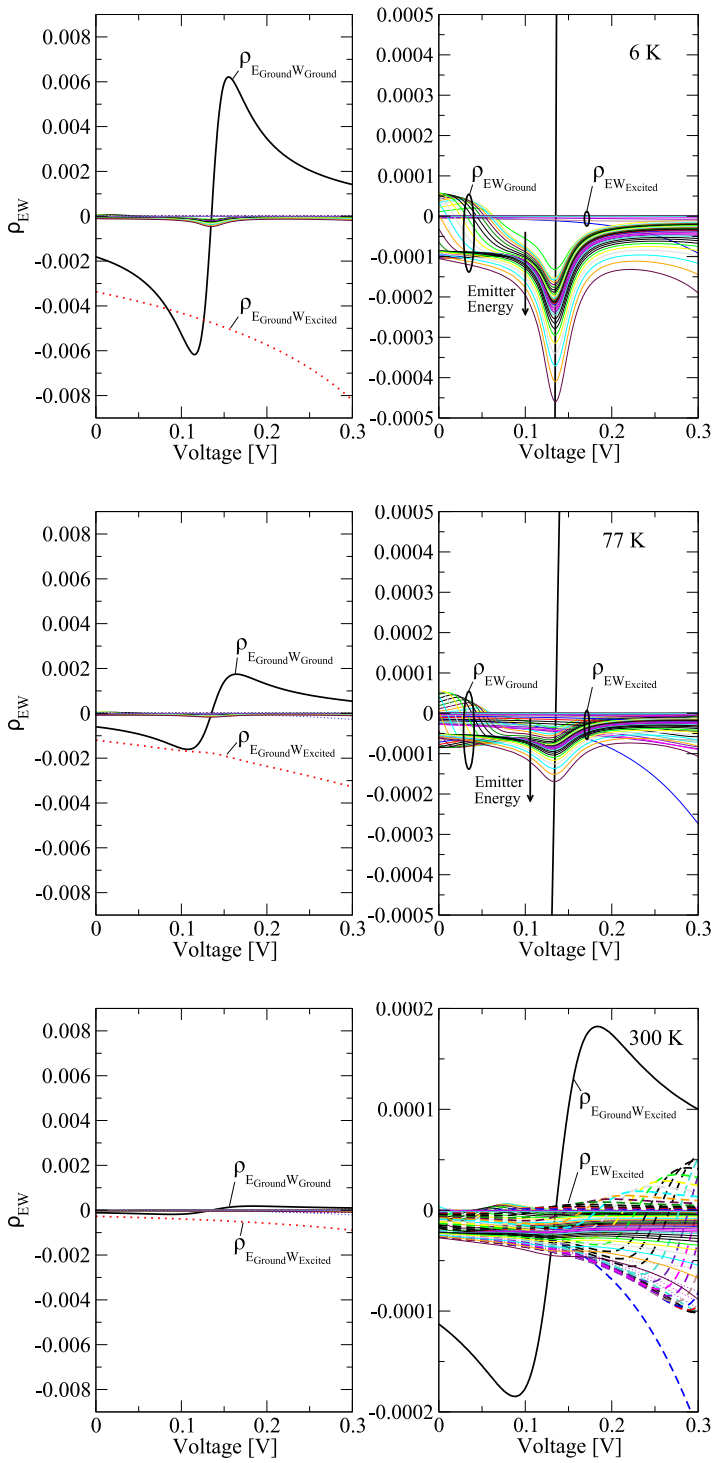

Figure 8.4: Calculated coherence between the continuum of states in the emitter at different temperatures. Solid lines, emitter-well ground state; dashed lines, emitter-well excited state

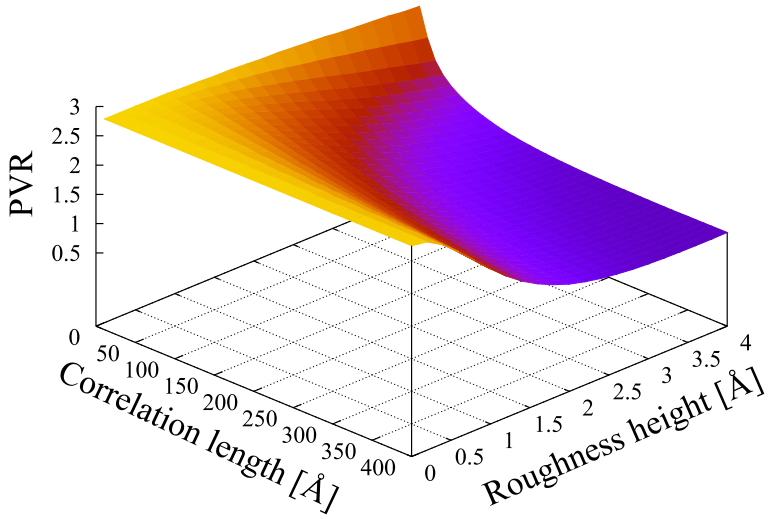

Figure 8.5: Peak to valley ratio versus correlation length (Λ) and roughness height (Δ) interface roughness parameters used in dephasing calculation at 77 K.

Typically, for intersubband scattering, Λ in the exponent term of Eq. (3.23) causes scattering rate to decrease with increasing Λ until it is outweighed by its contribution in the prefactor of Eq. (3.22), causing scattering to increase after some value. However, since dephasing is the main effect of scattering in RTDs, intrasubband elastic events are of greatest importance. These result in a small change in electron wavevector, and therefore the exponent term in Eq. (3.23) remains significant at large values of Λ.

8.2.7 Density matrix electron transport characteristics

Figure 8.6 shows the calculated I–V curve from 0.10–0.30 V using interface-roughness parameters Δ=2.8 Å and Λ=100 Å. Excellent agreement is obtained with the experimentally measured location of the current peak as well as the magnitude of the PVR. These roughness parameters are typical for AlGaAs/GaAs structures such as QCLs [66] suggesting that interface quality is very high in these MBE grown structures however this conclusion is subject to the condition that dephasing due to

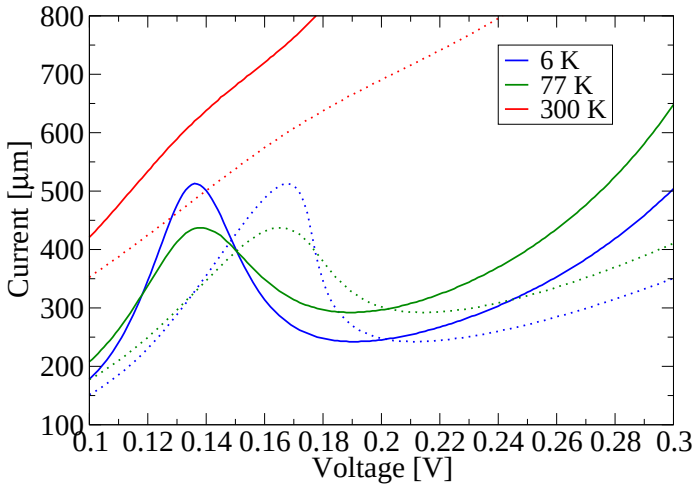

Figure 8.6: Simulated current with (dashed) and without (solid) an external series resistance applied to the data.

electron-electron scattering has been reasonably approximated.

The broadening due to dephasing gives improved agreement for the PVR compared with transfer matrix simulations for similar RTDs in Ref. 146; these predict a significant PVR value even at room temperature. Increasing current due to alignment of the first excited state in the well is underestimated by the model (current at the 0.136 V peak is achieved again at 0.26 V in the simulation, rather than 0.25 V observed experimentally) and this is likely due to overestimating the relevant confinement of the excited state in the well compared to the ground state. The DM model elucidates that the experimental current peak at V=0.165 V arises from the alignment with the quantised emitter state rather than the continuum above the emitter band edge where a combination of lower population, dephasing time and coupling strength is insufficient to induce an NDR feature. A previous study [23] of nitride RTDs has also observed alignment features prior to a significant NDR

feature. It is inferred from the DM model that these can be attributed to alignment with the emitter band-edge in cases where the alignment energies are sufficiently separated.

8.2.8 Experimental and theory discrepancies

It is noteworthy that the position of the NDR is close to that calculated theoretically but lies 29 mV above it. This suggests the presence of a contact resistance, R_{s}, in series with the device that shifts the physical NDR to higher voltages as described in Chapter 4. To estimate the magnitude of the series resistance, the R_{S} is found using Eq. (4.30) therein. The resulting shifted calculated I–V curves with a 60 Ω contact resistance are shown in Figure 8.6; this value is similar to those in Ref. 88 and that necessary for fitting with $\mathrm{Al}_x\mathrm{Ga}_{1-x}\mathrm{As}$/GaAs QCLs in Chapter 4. Alternatively, agreement can be achieved by assuming a constant voltage drop due to contacts. However, it is likely a combination of these effects is present. The absence of a plateau feature in the simulated I–V characteristics is consistent with experimental features being due to time-averaged oscillations of current when switching between configurations of an empty well while misaligned, and a populated well at resonance.

8.3 Nitride sequential tunnelling devices

In this section the theoretical and experimental characteristics are compared for a periodic triple-well structure similar to that in Ref. 140 with a period thickness of 178 nm in which interface and domain formation effects are not expected to dominate. These experimental devices were also grown at Purdue University, USA and studied in a recent collaboration with the present author. Ten periods of the structure were grown by the collaborators on a GaN substrate using MBE. The epitaxial layer thicknesses in each period are **23**/47/**10**/23/**26**/49 Å where the $\mathrm{Al}_{0.15}\mathrm{Ga}_{0.85}\mathrm{N}$

barriers are in bold, the GaN wells are in regular text, and the underlined well is n-doped with Si at $1 \times 10^{17}\,\mathrm{cm}^{-3}$ to give a sheet density of $5 \times 10^{10}\,\mathrm{cm}^{-2}$ per period. Contact layers were n^{++} doped at $2 \times 10^{18}\,\mathrm{cm}^{-3}$. The calculated bandstructure of the device at 18.6 kV/cm is shown in Figure 8.7(a), assuming a linear voltage drop across the device. The entire structure is also modelled with the *nextnano3*

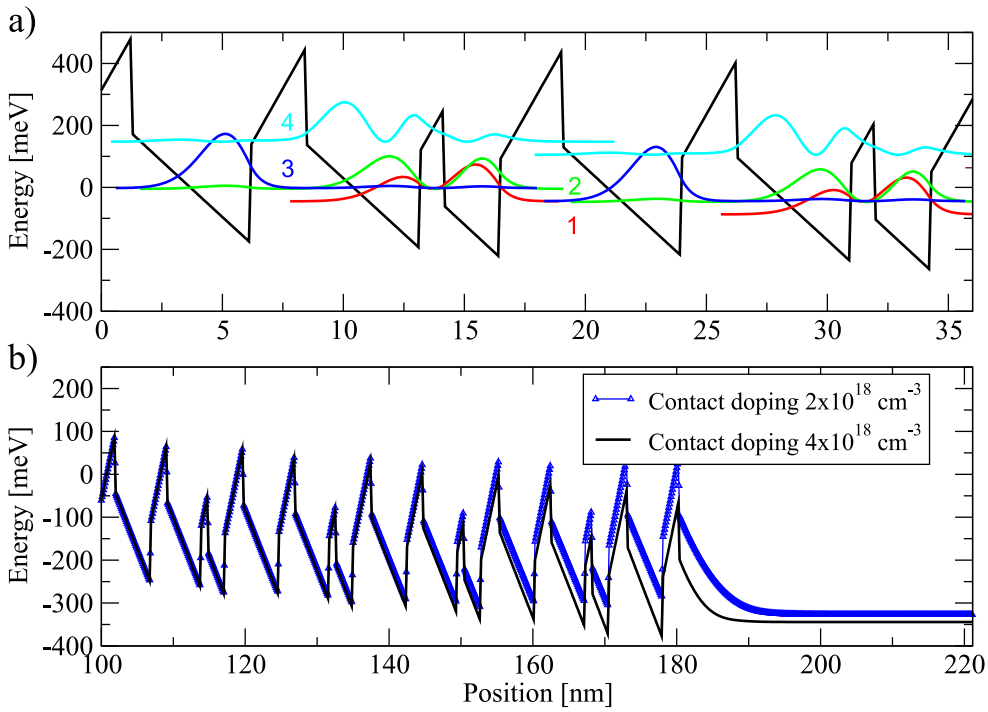

Figure 8.7: (a) Bandstructure and wavefunction plot of the sequential tunnelling device under an 18.6 kV/cm bias assuming a linear voltage drop. (b) Trailing few periods of the structure and contact region calculated with *nextnano3*.

solver [124] to check for voltage non-uniformity due to interface accumulation and depletion regions. This is shown in Figure 8.7(b), which verifies that the voltage drop is linear across most of the device. Figure 8.7(b) also shows that by doubling

the contact doping, *nextnano3* predicts that residual bending near the end of the device can be suppressed by increased screening due to the ionised dopants. While interface charge effects do not have a significant effect on sequential tunnelling in the majority of the device, careful control of the doping and spacer layers is necessary for the most efficient overall electron transport and simulations suggest that contact doping should generally be as high as possible.

The theoretical results in subsection 8.3.1 were calculated with the DM model described in Chapter 4 for three periods of the structure. No light field interaction was assumed since these sequential tunnelling structures exhibit no population inversion at any applied field.

8.3.1 Comparison of DM model and experimental results

The experimental and calculated current are shown in figure 8.8 as a function of the applied electric field, along with the subband energy variation. Two strong alignment features are apparent in the simulated current. From the DM model it is deduced that these arise from the ground state of the 49 Å well coming into resonance with the upstream states and downstream states at different biases. This behaviour is less readily apparent in the experimental data, since the sequential tunnelling features are obscured by a large parasitic current, which is likely due to traps and other current paths associated with defects such as screw dislocations [155]. However, the alignment features are clearly visible as plateaus in the differential resistance and there is excellent agreement between the experimental and simulated alignment voltages, indicating that effects of electric field domain formation are negligible on overall current.

The effect of electron–electron scattering is to reduce and broaden the vertical electron transport as shown in figure 8.8 and this must be taken into account in superlattice doping considerations for optimised structures. Simulations of the de-

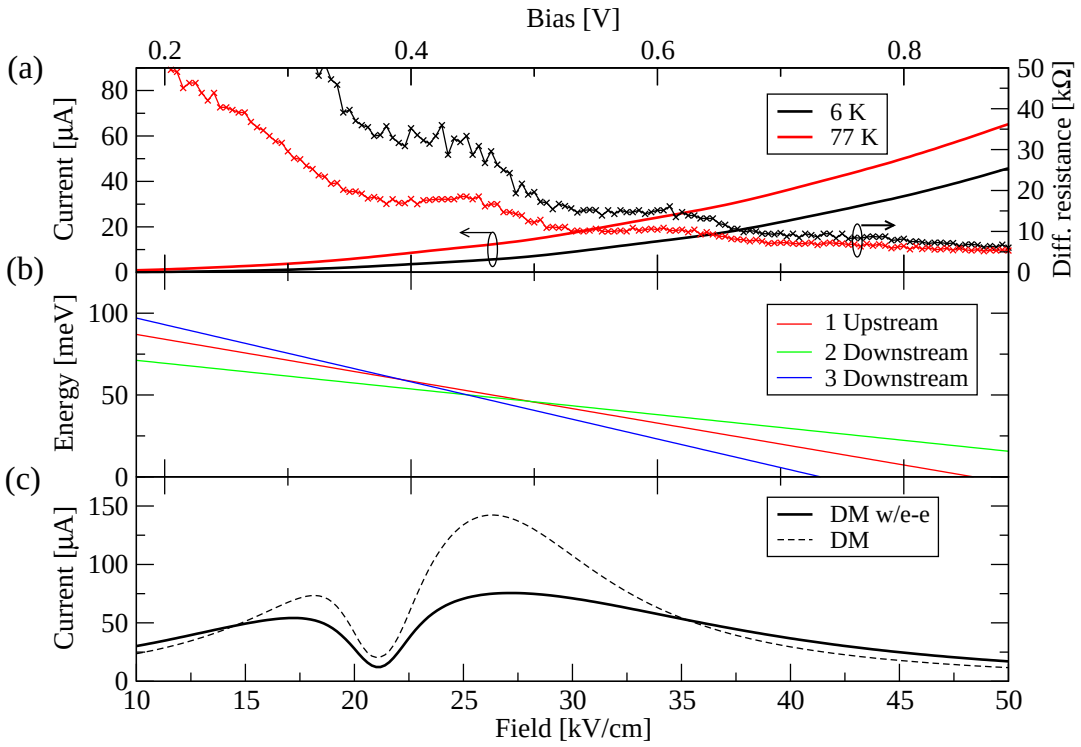

Figure 8.8: (a) Experimental current and differential resistance. (b) Calculated subband alignment energies at 77 K. (c) Current calculated with the density matrix formalism with and without additional e-e dephasing at 77 K. Experimental data shared by O. Malis for shared publication.

vice at 6 K resulted in negligible I–V differences compared with simulations at 77 K. This was unexpected since the experimental data shows a shift to lower resistance at higher temperatures. This discrepancy can be explained by the low lattice temperatures at which phonon scattering is insignificant, thus causing simulations to be similar at both temperatures. The experimental decrease in resistance is then consistent with recent studies on the thermal activation of charge traps [156] and resembles features of Frenkel–Poole tunnelling [157].

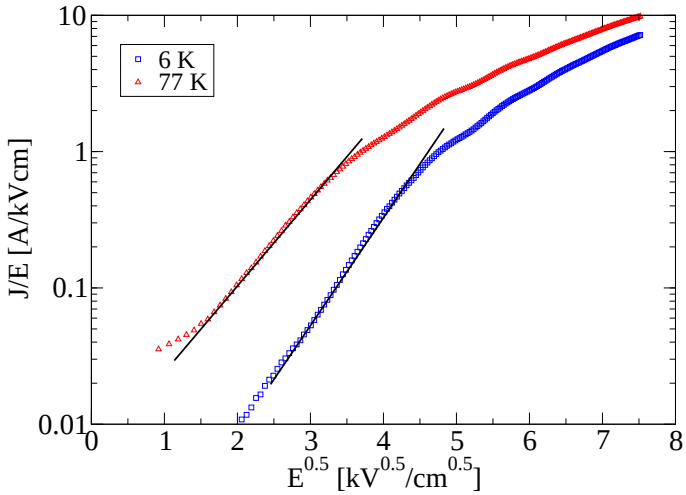

Figure 8.9: Experimental sequential tunnelling current divided by electric field vs square root of electric field at 6 K and 77 K along with straight line fits.

8.3.2 Effect of nitride defects

Frenkel–Poole tunnelling enhances current flow with a linear dependence between the current divided by the electric field and the square root of the electric field. Figure 8.9 shows a clear linear dependence between these functions however the linear electric field over the active region could not be used to fit Frenkel–Poole or phonon emission expressions typically applied to HEMTs [158]. This may indicate that the electric field relevant for these expressions is a complex interaction between forward applied bias, reverse barrier fields and domain formation effects (if present), or that the leakage current comes from another mechanism entirely. Along with previous studies on the electron charge trapping, these results (along with those presented in Chapter 5) indicate that room temperature sequential tunnelling is feasible provided material quality and suppression of defects is improved further. This is important for thicker structures, such as QCLs, which require up to 10-µm-thick active regions, although several studies have been performed to minimise strain

with balanced substrates [159, 160].

8.4 Conclusion

This chapter investigated the vertical electron transport in different types of AlGaN/GaN heterostructures both theoretically and experimentally. The density matrix formalism adapted for use with RTDs was shown to have excellent agreement with the measured current–voltage characteristics. It was shown that a continuous range of interface roughness parameters can yield the experimentally observed PVR and that values of Δ=2.8 Å and Λ=100 Å that are typical for $Al_xGa_{1-x}As$/GaAs devices gave an excellent fit. Only the interface roughness parameters, electron-electron dephasing and coupling strength scaling factor were used to obtain agreement with the measurement, suggesting that it can be used as a reliable analyser, if not yet a predictive RTD model. A novel characteristic of this model is that it is based on the same model that obtained excellent results for $Al_xGa_{1-x}As$/GaAs QCLs and was used to design $Al_xGa_{1-x}N$/GaN QCL design proposals.

Additionally, agreement between the predicted subband alignments and experimental differential resistance plateaus was achieved with the DM model. By comparing the magnitude of the current, it was shown that parasitic transport attributed to defects appears to dominate the experimental I–V. While these could not be fitted with forms of Frenkel–Poole tunnelling, it was shown that the experimental curves do shown a linear dependence between the current divided by the electric field and the square root of the electric field. Domain formation at the interface between cladding layers and the superlattice heterostructure was shown to be reduced by increased doping of the cladding layers. This, along with further reduction of the substrate defect density are identified as some remaining solutions to potentially realising an $Al_xGa_{1-x}N$/GaN QCL.

Chapter 9

Concluding remarks

A range of intersubband devices in $Al_xGa_{1-x}As/GaAs$ and $Al_xGa_{1-x}N/GaN$ have been investigated to establish the feasibility of room temperature THz QCL sources. This chapter summarises the findings of each of the relevant chapters and presents proposals for future work.

Quantum cascade lasers are promising sources of THz radiation which are powerful and compact. However, they are currently limited to temperatures where cryogenic cooling is necessary which limits their adoption in applications. Improvements in QCL output power and even more importantly, operating temperature is an active area for many research groups. While most THz QCL active region records have been set with the $Al_xGa_{1-x}As/GaAs$ material system, $Al_xGa_{1-x}N/GaN$ is a promising alternative due to its significantly different material parameters. The material parameters and methods for calculating the confined subband energies were shown in Chapter 2. The effect of internal electric fields due to spontaneous and piezoelectric polarisations were shown to have a significant effect on the confined subband energies for a quantum well system.

The optical and electronic transport properties in intersubband devices are both affected by the incoherent scattering mechanisms that cause electrons to change

state. The scattering rates based on Fermi's golden rule derived by others and used in this work were presented in Chapter 3 for both inter- and intra-subband scattering due to alloy disorder, interface roughness, LO-phonons, acoustic phonons, impurities, and electron-electron scattering. In addition to these incoherent scattering mechanisms, coherent transport such as tunnelling is present in electrically active intersubband devices. The density matrix approach offers many advantages over the rate equation approach which has been used previously to design AlGaAs and AlGaN QCLs. This approach allows the incoherent scattering rates described in Chapter 3 to be used with a tight-binding Hamiltonian for a structure so that tunnelling can be calculated coherently.

The concepts of density matrices and how they can be applied to QCL structures is presented in Chapter 4. This model was applied to the current high temperature record structure based on resonant LO-phonon depopulation of the lower laser level and extraction state. The current–voltage and light–current characteristics variation with temperature were observed to have good agreement. IFR values of $\Delta = 2.8\,\text{Å}$ and $\Lambda = 100\,\text{Å}$ were shown to give good agreement in the present work similar to the findings of other theoretical modelling groups [66]. Gain predicted by the model was predicted to peak at $\sim$3.2 THz in good agreement with the experimentally observed 3.22 THz. For lasing to cease at 200 K, our model predicts cavity losses of $13.5\,\text{cm}^{-1}$ in reasonable agreement with values presented elsewhere [8, 66]. This performance degradation with temperature was shown to be due to thermal activation of carriers in subbands allowing LO-phonon emission (non-radiative emission) and thermal backfilling. While this model had been previously applied to SiGe QCL structures, it had not been validated or compared with other approaches and experimental data. Chapter 4 also showed comparisons of the output with that of a rate equation approach [82] and a non equilibrium Green's function model. These results show that the extended DM model here is capable of replicating QCL characteristics

without the need for the computationally intensive Green's function approach. It was also shown that experimental discrepancies in some regrowths of this structure can be explained by contact voltage drops and a contact resistance in series with the QCL. A voltage drop of 5 V and series resistance of 0.8 Ω were shown to give good agreement with the QCL results presented in Ref. [89].

Theoretical simulations of recently grown QCLs at MIT [89] with tall AlAs barriers were shown in Chapter 5 to explain experimentally observed phenomenon. Specifically, designs where all barriers are replaced with AlAs are not expected to lase due to excessive broadening by interface roughness scattering. This was attributed to the IFR scattering proportionality with the square of the AlAs/GaAs interface potential. While previous studies have investigated the effect of growth imperfections such as alloy inter-diffusion, the effect of long-range interface roughness on QCL structures was shown for the first time in the present work. Previous demonstrations applied to simple QW structures only [32] showed how this broadens the peak absorption energy and this was shown to lead to reduced gain in QCLs due to its effect on broadening. Devices with tall, thin barriers were shown to be more sensitive to these long-range fluctuations and it is suggested that spatially separated tall barriers are used instead. Genetic algorithms are an efficient technique to optimise QCL structures and it was shown that $Al_xGa_{1-x}As$/GaAs QCLs optimised for different temperatures have significantly different gain-temperature characteristics. High temperature QCLs can be expected to have a smaller output power at low temperatures due to the more diagonal optical transition typically necessary to minimise non-radiative emission when subbands become thermalised. Calculations of existing $Al_xGa_{1-x}N$/GaN QCL designs [15, 102] suggest that these did not include the effect of both intra- and inter-subband scattering on the linewidth and therefore their designs were not predicted to have gain even at low temperature.

The critical design parameters of QCLs were shown during the course of this

work to be:

- Optimised doping levels; increasing doping increases the gain until a point where dephasing and scattering processes reduce it
- Minimisation of well/barrier potential to reduce effect of interface roughness broadening of gain
- Efficient injection and extraction of carriers into the upper and lower lasing levels

These were used to suggest an initial starting structure for optimisation of nitride structures. 8 % alloy content barriers were used rather than the typical 15 % to reduce the effect of the much larger conduction band offset between AlN and GaN than that in $Al_xGa_{1-x}As/GaAs$. A 4-well structure was designed with two energy level pairs having similar transition energies with a population inversion predicted between each pair of upper and lower lasing levels. The optimised structure was shown to have sufficient gain of $26\,cm^{-1}$ to overcome waveguide losses at room temperature at an applied field of 61 kV/cm with current densities of $\sim$13kA/cm^2. While this current density is larger than for $Al_xGa_{1-x}As/GaAs$ devices, they are typical for $Al_xGa_{1-x}N/GaN$ structures due to the higher doping and required applied fields [15].

To demonstrate how the DM model could be used to explain QCL characteristics in applications, the effect of light variations due to self-mixing on the QCL was investigated in Chapter 6. It was shown that varying the cavity losses that the QCL is clamped to for a given applied field changes the current density by an appreciable amount. Since QCLs are typically driven with a fixed current, the structure changes bias so that the current due to scattering and tunnelling plus the photon driven current are equal to the drive current. By assuming a fixed change in cavity power, this assumption was proven to give good agreement with experimentally measured

variation of the self-mixing signal V_{SM} with drive current using both a theoretically calculated I–V curve and a hybrid model with the experimental data.

The feasibility of optical $\mathrm{Al}_x\mathrm{Ga}_{1-x}\mathrm{N}$/GaN intersubband devices was proven by a theoretical investigation of near-IR and THz absorption structures in Chapter 7. It was found that many body effects have a significant effect on the transition energy for near-IR structures and must be included for agreement of theoretical and experimentally measured peak absorption energy. By varying the well widths and doping density it was shown that predicted linewidths due lifetime broadening are expected to change significantly. In the near-IR structures grown by collaborators at Purdue University, USA it was found that intrasubband scattering due to ionised impurities contributed most to the intersubband absorption between ground and first excited states. A value of 102 meV was predicted for the sample investigated, in good agreement with the 90 meV measured experimentally [32]. While interface roughness scattering was not included here, it can be inferred from the results that small changes in doping or well width could reduce the predicted impurity scattering contribution to a value less than 90 meV so that the effect of thickness variations can also be included. Good agreement was also obtained for THz absorption structures however many-body corrections did not improve agreement of the peak absorption energy position.

To investigate electron transport properties of $\mathrm{Al}_x\mathrm{Ga}_{1-x}\mathrm{N}$/GaN intersubband devices, the density matrix model in Chapter 4 was adapted for use with resonant tunnelling diodes. This assumes a continuum of states for the emitter and collection reservoirs with a continuum of states in a sufficiently wide well. The effect of interface roughness parameters on the RTD figure of merit, the peak to valley ratio (PVR), was presented. It was found that large values of IFR roughness height can suppress the NDR completely even at 77 K. Inclusion of broadening due to IFR and other mechanisms was shown to give improved results compared with transfer matrix

simulations in Ref. [146] which assume purely coherent transport. I–V curves with good agreement to experimental devices also grown and characterised by collaborators at Purdue University was achieved. However, sequential tunnelling devices were shown to be dominated by parasitic currents likely due to defects such as charge traps and screw dislocations. Despite the significant difference between theoretical and experimental I–V characteristics, the alignment of experimental differential resistance plateaus with peaks in current predicted by the DM model indicate that sequential tunnelling is likely occurring in these devices. It is suggested that if contact doping is increased, defect density is reduced, and layer thicknesses optimised, then QCL structures may be realised in the next few years.

9.1 Further work

The present work on the optical and electronic properties of $Al_xGa_{1-x}As/GaAs$ and $Al_xGa_{1-x}N/GaN$ intersubband devices has led to the identification of possible future research topics. While improvements of active regions and modelling are desirable, it is likely that reduction of experimental $Al_xGa_{1-x}N/GaN$ defect densities is most critical to the realisation of nitride QCL structures.

The DM QCL model used in the present work (Chapter 4) was shown to have good agreement with NEGF and experimental results however it is still based on several assumptions. Most importantly, a single electron subband temperature was used for all states. This has shown to be a fair approximation however improved agreement may be obtained with Monte-Carlo approaches which track electron distributions over time and can show subbands having different temperatures [102]. Additionally, second order tunnelling was shown to be important in mid-IR QCLs and this should be included in the DM model to investigate its relevance in THz QCLs [161].

Active region optimisation for high-temperature operation is an active research area at many institutions. Several groups are currently working on variable height barriers to optimise the optical transition, and some have proposed tall barriers selectively placed to reduce leakage current. It was shown that a genetic algorithm can be used to automatically propose designs for operation at a desired wavelength and temperature in Chapter 5. This should now be applied to devices with variable barrier heights to suggest possible improved $Al_xGa_{1-x}As$/GaAs designs. Similarly, further investigation of $Al_xGa_{1-x}N$/GaN QCL designs should be completed for designs operating in the Reststrahlen band of GaAs devices.

Chapter 6 presented results of the DM model applied to self-mixing interferometry to investigate the origin of terminal voltage variations. While good agreement was achieved, a full model which solves the excess phase equation should now be completed. Additionally, the partial derivative form of the Liouville equation is suitable to analyse the time evolution of the QCL populations and coherences [75]. This could be used to develop a dynamic model similar to the simple RRE approach proposed in collaboration with the present author in Ref. 117. This would allow the investigation of self-mixing with electrically modulated pulsed QCLs, as well as concepts such as self-induced transparency [162].

Finally, it was shown in Chapters 7 and 8 that interface roughness in $Al_xGa_{1-x}N$/GaN devices is comparable to that of $Al_xGa_{1-x}As$/GaAs devices which have been experimentally realised. It would be prudent to use the RTD DM model to evaluate the PVR of RTDs with various barrier alloy contents and well thicknesses to investigate the effect of dephasing. Efforts should now focus on innovations such as those discussed in Chapter 1 to improve growth quality and reduce defect densities. This may be achieved by advances in MBE growth or by strain engineering of substrates [15, 159].

Appendix A

On the approximations of the DM RTD model

A.1 Contact well widths

The density matrix model developed for transport in resonant tunnelling diodes in Chapter 8 is an adaption of that used for QCLs. However, the presence of highly doped contact regions on either side of the active region is significantly different from the approach for QCLs where periodic transport is assumed. In the RTD model, a continuum of discrete energy levels is used to approximate a continuum of energy levels in the emitter and collector reservoirs. It is therefore important to establish the efficacy of this approach by varying the well width used to calculate wavefunctions.

As a bias is applied across the RTD device the reservoir contact band edge goes down in energy. Since collector states are required to be present at the top of the well near the well confined states, this well becomes increasingly deeper. During the voltage sweep, discrete energy states may enter the collector well and change the coherences of all other states by a small amount. In the results presented in

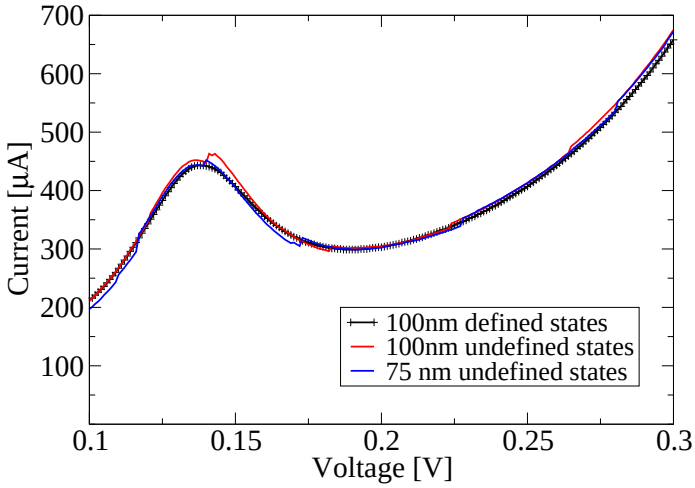

Figure A.1: I–V characteristics at 77 K for the RTD in Chapter 8 with a different contact length. Defined and undefined refer to specified and floating numbers of states in the wells.

Chapter 8 the number of states was set to be 35, 2, and 40 in the emitter, well, and collector regions respectively with a contact length of 100 nm. This removes the effect of states entering and leaving the calculation. A comparison of this approach (with "defined" states) with a floating number of states ("undefined") is shown in figure A.1. It can be seen that defining a reasonable number of states has little effect on the peak current, its position, or the PVR value. This is due to the states at the top of each well having an insignificant population to contribute to the electron transport characteristics. A full I–V sweep with undefined states and 75 nm contacts is also shown in figure A.1 and it can be seen that this change in contact length also has little effect. To establish the minimum well width necessary for correct treatment of contacts, it is necessary to calculate the current over a wider range of contact widths.

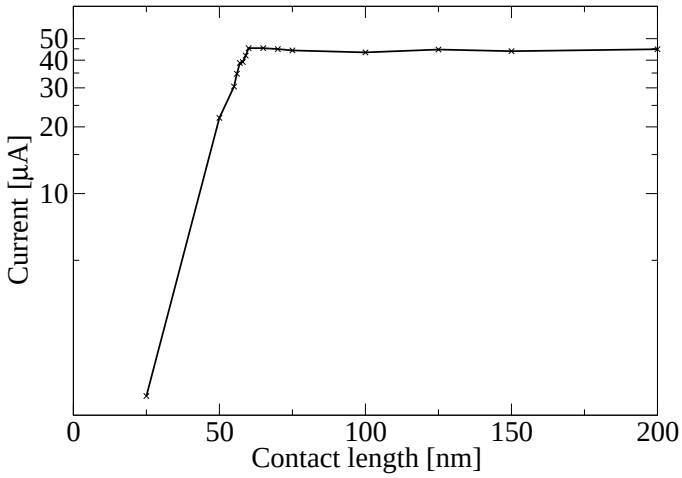

Figure A.2: Calculated current density at 0.135 V versus length of emitter and collector reservoirs.

Figure A.2 shows the calculated current at 0.135 V versus the length of the contacts in the emitter and collector reservoirs. For this calculation the number of states included for the density matrix was undefined so that the states present are set correctly. It can be seen that current density rapidly converges after contact lengths of 60 nm. Along with the results in figure A.1, this supports the suitability of discrete states used to approximate the emitter and collector reservoirs.

A.2 Estimation of coupling strengths

In Chapter 8 the calculated coupling strengths between states in adjacent periods were scaled by 0.36 to achieve agreement between the theoretical and experimental current. While this is attributed to overestimation caused by the tight-binding Hamiltonian, this may have an affect on the coherences and therefore the PVR. To investigate this, simulations for the RTD at 77 K were repeated with the same

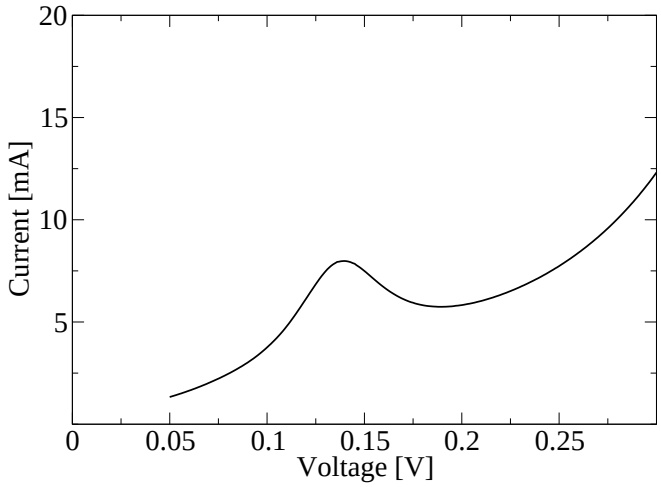

Figure A.3: I–V simulation at 77 K for the RTD in Chapter 8 at 77 K with no fitting of the calculated coupling strengths. Magnitude of the PVR remains 1.43 despite higher coupling strengths.

parameters. Figure A.3 shows that the current is a factor of 18.4 larger however the PVR remains the same as that predicted with scaled coupling strengths and the experimental data (PVR=1.43).

A.3 Electron-electron dephasing

An assumption in the density matrix model is a fixed intrasubband carrier-carrier scattering rate of $1\times10^{13}\,\mathrm{s}^{-1}$ for reservoir states. This value was set as it is similar to the average scattering rate calculated with the model presented in Chapter 3 and full calculations are computationally demanding due to the number of states present here. The fixed value underestimates the dephasing value for the quantised emitter state, and the effect of this on the PVR and current characteristics are presented here.

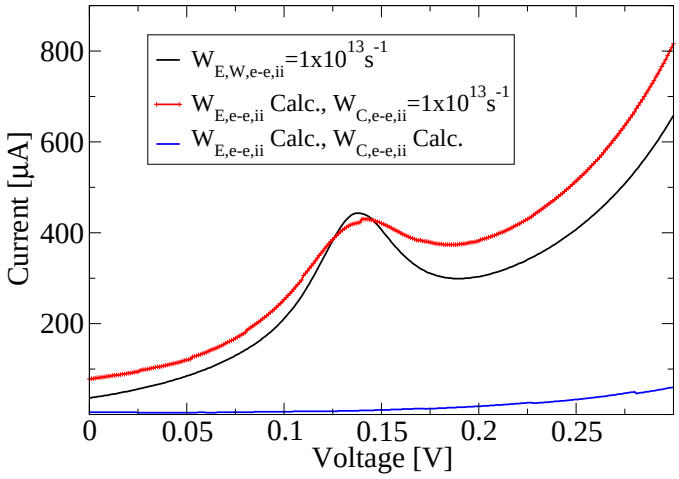

Figure A.4: I–V simulations with various implementations of electron-electron scattering. Including scattering as calculated (using Eq. 3.32) for the emitter reservoir reduces the PVR slightly, and its inclusion in the collector region suppresses all RTD behaviour.

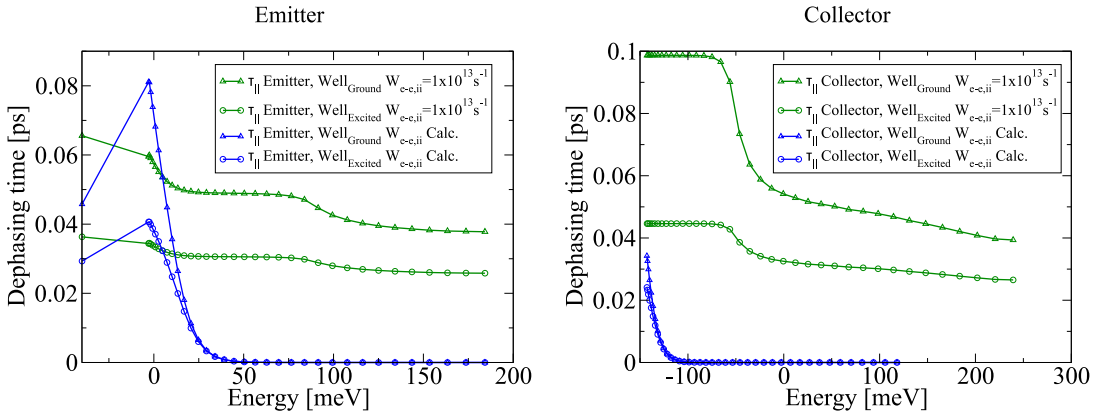

Figure A.5: Calculated dephasing times at 77 K for the emitter and contact regions with a fixed electron-electron scattering rate and with the calculated values.

Figure A.4 shows the *I-V* sweep of the device in Chapter 8 with electron-electron scattering included as they were calculated for the emitter side (collector dephasing due to electron-electron scattering is kept at W=1×10^{13}s^{-1}). It can be seen from this that this reduces the PVR predicted which is due to dephasing increasing. It was found that the experimental PVR of 1.43 could not be replicated even with low interface roughness values; the maximum PVR achievable with this implementation is 1.324. Including the calculated dephasing in the collector region suppresses any RTD type behaviour in the model due to almost instantaneous dephasing.

The carrier-carrier scattering model is often neglected in QCL simulations, and its validity at such high doping densities and regions high above the Fermi level may be questioned. Figure A.5 shows the calculated dephasing times in the emitter and collector reservoirs versus energy with fixed and calculated electron-electron scattering rates. At energies much higher than the Fermi level where states are insignificantly populated, final state blocking is negligible. The scattering rate in these regions increases to values $>1\times10^{20}$s^{-1} with the model presented in Ref. [67]. Since carriers do propagate through the second barrier experimentally, it can be inferred that these scattering rates are unphysical and a fixed value is appropriate. This does not affect the conclusion presented in Chapter 8 regarding the presence of high quality interfaces; a higher electron-electron scattering rate would imply lower interface roughness scattering for a given PVR.

References

[1] T. Ando, A. B. Fowler, and F. Stern, "Electronic properties of two-dimensional systems," *Rev. Mod. Phys.*, vol. 54, pp. 437–672, Apr. 1982.

[2] L. C. West and S. J. Eglash, "First observation of an extremely large dipole infrared transition within the conduction band of a GaAs quantum well," *Appl. Phys. Lett.*, vol. 46, no. 12, pp. 1156–1158, 1985.

[3] W. S. Chang, *Principles of lasers and optics*. Cambridge University Press, 2005.

[4] E. Yablonovitch and E. Kane, "Band structure engineering of semiconductor lasers for optical communications," *J. Lightwave Technol.*, vol. 6, pp. 1292–1299, Aug. 1988.

[5] A. Adams, "Band-structure engineering for low-threshold high-efficiency semiconductor lasers," *Electron. Lett*, vol. 22, pp. 249–250(1), Feb. 1986.

[6] J. Faist, F. Capasso, D. L. Sivco, C. Sirtori, A. L. Hutchinson, and A. Y. Cho, "Quantum cascade laser," *Science*, vol. 264, no. 5158, pp. 553–556, 1994.

[7] R. Kohler, A. Tredicucci, F. Beltram, H. Beere, E. Linfield, A. Davies, D. Ritchie, R. Iotti, and F. Rossi, "Terahertz semiconductor-heterostructure laser," *NATURE*, vol. 417, pp. 156–159, May 2002.

[8] S. Fathololoumi, E. Dupont, C. Chan, Z. Wasilewski, S. Laframboise, D. Ban, A. Mátyás, C. Jirauschek, Q. Hu, and H. C. Liu, "Terahertz quantum cascade lasers operating up to $\sim$ 200 K with optimized oscillator strength and improved injection tunneling," *Opt. Express*, vol. 20, pp. 3866–3876, Feb. 2012.

[9] L. Li, L. Chen, J. Zhu, J. Freeman, P. Dean, A. Valavanis, A. Davies, and E. Linfield, "Terahertz quantum cascade lasers with >1 W output powers," *Electron. Lett*, vol. 50, pp. 309–311(2), Feb. 2014.

[10] Y. Bai, S. Slivken, S. R. Darvish, A. Haddadi, B. Gokden, and M. Razeghi, "High power broad area quantum cascade lasers," *Appl. Phys. Lett.*, vol. 95, no. 22, 221104, 2009.

[11] Y. Yao, A. J. Hoffman, and C. F. Gmachl, "Mid-infrared quantum cascade lasers," *Nat. Photonics*, vol. 6, no. 7, pp. 432–439, 2012.

[12] S. Nakamura and S. Chichibu, *Introduction to nitride semiconductor blue lasers and light emitting diodes*. Taylor & Francis, 2000.

[13] C. Gmachl, H. M. Ng, and A. Y. Cho, "Intersubband absorption in GaN/AlGaN multiple quantum wells in the wavelength range of λ=1.75–4.2 µm," *Appl. Phys. Lett.*, vol. 77, no. 3, pp. 334–336, 2000.

[14] C. Gmachl, H. M. Ng, S.-N. George Chu, and A. Y. Cho, "Intersubband absorption at λ=1.55 µm in well- and modulation-doped GaN/AlGaN multiple quantum wells with superlattice barriers," *Appl. Phys. Lett.*, vol. 77, no. 23, pp. 3722–3724, 2000.

[15] V. D. Jovanović, D. Indjin, Z. Ikonić, and P. Harrison, "Simulation and design of GaN/AlGaN far-infrared (λ=34 µm) quantum-cascade laser," *Appl. Phys. Lett.*, vol. 84, no. 16, pp. 2995–2997, 2004.

[16] H. Yasuda, T. Kubis, I. Hosako, and K. Hirakawa, "Non-equilibrium green's function calculation for GaN-based terahertz-quantum cascade laser structures," *J. Appl. Phys.*, vol. 111, no. 8, 083105, 2012.

[17] M. Tchernycheva, L. Nevou, L. Doyennette, F. H. Julien, E. Warde, F. Guillot, E. Monroy, E. Bellet-Amalric, T. Remmele, and M. Albrecht, "Systematic experimental and theoretical investigation of intersubband absorption in GaN/AlGaN quantum wells," *Phys. Rev. B*, vol. 73, 125347, Mar. 2006.

[18] P. K. Kandaswamy, F. Guillot, E. Bellet-Amalric, E. Monroy, L. Nevou, M. Tchernycheva, A. Michon, F. H. Julien, E. Baumann, F. R. Giorgetta, D. Hofstetter, T. Remmele, M. Albrecht, S. Birner, and L. S. Dang, "GaN/AlN short-period superlattices for intersubband optoelectronics: A systematic study of their epitaxial growth, design, and performance," *J. Appl. Phys.*, vol. 104, no. 9, 093501, 2008.

[19] D. Hofstetter, D. P. Bour, and L. Kirste, "Mid-infrared electro-luminescence and absorption from AlGaN/GaN-based multi-quantum well inter-subband structures," *Appl. Phys. Lett.*, vol. 104, no. 24, 241107, 2014.

[20] W. Terashima and H. Hirayama, "Spontaneous emission from GaN/AlGaN terahertz quantum cascade laser grown on GaN substrate," *Phys. Status. Solidi C*, vol. 8, pp. 2302–2304, July 2011.

[21] S. Golka, C. Pflügl, W. Schrenk, G. Strasser, C. Skierbiszewski, M. Siekacz, I. Grzegory, and S. Porowski, "Negative differential resistance in dislocation-free GaN/AlGaN double-barrier diodes grown on bulk GaN," *Appl. Phys. Lett.*, vol. 88, no. 17, 172106, 2006.

[22] C. Bayram, Z. Vashaei, and M. Razeghi, "AlN/GaN double-barrier resonant

tunneling diodes grown by metal-organic chemical vapor deposition," *Appl. Phys. Lett.*, vol. 96, no. 4, 042103, 2010.

[23] D. Li, L. Tang, C. Edmunds, J. Shao, G. Gardner, M. J. Manfra, and O. Malis, "Repeatable low-temperature negative-differential resistance from $Al_{0.18}Ga_{0.82}N$/GaN resonant tunneling diodes grown by molecular-beam epitaxy on free-standing GaN substrates," *Appl. Phys. Lett.*, vol. 100, no. 25, 252105, 2012.

[24] F. Capasso, K. Mohammed, and A. Y. Cho, "Resonant tunneling through double barriers, perpendicular quantum transport phenomena in superlattices, and their device applications," in *Electronic Structure of Semiconductor Heterojunctions*, pp. 99–115, Springer, 1988.

[25] L. Esaki and R. Tsu, "Superlattice and negative differential conductivity in semiconductors," *IBM J. Res. Dev.*, vol. 14, pp. 61–65, Jan. 1970.

[26] B. S. Williams, "Terahertz quantum-cascade lasers," *Nat. Photonics*, vol. 1, no. 9, pp. 517–525, 2007.

[27] A. G. Davies, A. D. Burnett, W. Fan, E. H. Linfield, and J. E. Cunningham, "Terahertz spectroscopy of explosives and drugs," *Mater. Today*, vol. 11, no. 3, pp. 18–26, 2008.

[28] R. M. Woodward, B. E. Cole, V. P. Wallace, R. J. Pye, D. D. Arnone, E. H. Linfield, and M. Pepper, "Terahertz pulse imaging in reflection geometry of human skin cancer and skin tissue," *Phys. Med. Biol.*, vol. 47, no. 21, p. 3853, 2002.

[29] P. Dean, Y. L. Lim, A. Valavanis, R. Kliese, M. Nikolić, S. P. Khanna, M. Lachab, D. Indjin, Z. Ikonić, P. Harrison, A. D. Rakić, E. H. Linfield, and

A. G. Davies, "Terahertz imaging through self-mixing in a quantum cascade laser," *Opt. Lett.*, vol. 36, pp. 2587–2589, July 2011.

[30] P. Dean, A. Valavanis, J. Keeley, K. Bertling, Y. L. Lim, R. Alhathlool, A. D. Burnett, L. H. Li, S. P. Khanna, D. Indjin, T. Taimre, A. D. Rakić, E. H. Linfield, and A. G. Davies, "Terahertz imaging using quantum cascade lasers - a review of systems and applications," *J. Phys. D: Appl. Phys.*, vol. 47, no. 37, p. 374008, 2014.

[31] A. Grier, J. D. Cooper, L. Lever, A. Valavanis, Z. Ikonić, D. Indjin, P. Harrison, C. Edmunds, J. Shao, L. Tang, G. Gardner, D. Zakharov, M. J. Manfra, and O. Malis, "A scattering rate approach to the understanding of absorption line broadening in near-infrared AlGaN/GaN quantum wells," in *6th Space Agency - MOD Workshop on Wideband Gap Semiconductors and Components, 8–9 October 2012, ESA-ESTEC, Noordwijk, The Netherlands*, Oct 2012.

[32] C. Edmunds, L. Tang, M. Cervantes, M. Shirazi-HD, J. Shao, A. Grier, A. Valavanis, J. D. Cooper, D. Li, G. Gardner, D. N. Zakharov, Z. Ikonić, D. Indjin, P. Harrison, M. J. Manfra, and O. Malis, "Comparative study of intersubband absorption in AlGaN/GaN and AlInN/GaN superlattices: Impact of material inhomogeneities," *Phys. Rev. B*, vol. 88, 235306, Dec. 2013.

[33] P. Harrison, *Quantum wells, wires and dots: theoretical and computational physics of semiconductor nanostructures.* John Wiley & Sons, 2009.

[34] A. Valavanis, *n-type silicon-germanium based terahertz quantum cascade lasers.* PhD thesis, University of Leeds, 2009.

[35] E. Anderson, Z. Bai, J. Dongarra, A. Greenbaum, A. McKenney, J. Du Croz, S. Hammerling, J. Demmel, C. Bischof, and D. Sorensen, "LAPACK: A

portable linear algebra library for high-performance computers," in *Proceedings of the 1990 ACM/IEEE Conference on Supercomputing*, Supercomputing 1990, (Los Alamitos, CA, USA), pp. 2–11, IEEE Computer Society Press, 1990.

[36] J. D. Cooper, *Simulation of surface acoustic wave modulation of quantum cascade lasers*. PhD thesis, University of Leeds, 2013.

[37] J. D. Cooper, A. Valavanis, Z. Ikonić, P. Harrison, and J. E. Cunningham, "Finite difference method for solving the Schrödinger equation with band nonparabolicity in mid-infrared quantum cascade lasers," *J. Appl. Phys.*, vol. 108, no. 11, 113109, 2010.

[38] V. D. Jovanović, *Theory and design of GaAs and GaN-based quantum cascade lasers and quantum well infrared photodetectors*. PhD thesis, University of Leeds, May 2005.

[39] M. Stopa and S. Das Sarma, "Calculated shallow-donor-level binding energies in GaAs-$Al_xGa_{1-x}As$ quantum wells," *Phys. Rev. B*, vol. 40, pp. 8466–8472, Oct. 1989.

[40] K. Lee, D. Yoon, S. Bae, M. Park, and G. Kim, "Self-consistent subband calculations of AlGaN/GaN single heterojunction," *ETRI Journal*, vol. 24, no. 4, pp. 270–279, 2002.

[41] P. Harrison, "The nature of the electron distribution functions in quantum cascade lasers," *Appl. Phys. Lett.*, vol. 75, no. 18, pp. 2800–2802, 1999.

[42] I. Vurgaftman, J. R. Meyer, and L. R. Ram-Mohan, "Band parameters for III-V compound semiconductors and their alloys," *J. Appl. Phys.*, vol. 89, no. 11, pp. 5815–5875, 2001.

[43] S. Adachi, *GaAs and Related Materials: Bulk semiconducting and superlattice properties*. World Scientific, 1994.

[44] S. M. Sze and K. K. Ng, *Physics of semiconductor devices*. John Wiley & Sons, 2006.

[45] M. Sotoodeh, A. Khalid, and A. Rezazadeh, "Empirical low-field mobility model for III–V compounds applicable in device simulation codes," *J. Appl. Phys.*, vol. 87, no. 6, pp. 2890–2900, 2000.

[46] K. Momma and F. Izumi, "*VESTA3* for three-dimensional visualization of crystal, volumetric and morphology data," *J. Appl. Crystallogr.*, vol. 44, pp. 1272–1276, Dec. 2011.

[47] H. Machhadani, P. Kandaswamy, S. Sakr, A. Vardi, A. Wirtmüller, L. Nevou, F. Guillot, G. Pozzovivo, M. Tchernycheva, A. Lupu, L. Vivien, P. Crozat, E. Warde, C. Bougerol, S. Schacham, G. Strasser, G. Bahir, E. Monroy, and F. H. Julien, "GaN/AlGaN intersubband optoelectronic devices," *New J. Phys.*, vol. 11, no. 12, 125023, 2009.

[48] F. Bernardini and V. Fiorentini, "Spontaneous versus Piezoelectric Polarization in III-V Nitrides: Conceptual Aspects and Practical Consequences," *Phys. Status. Solidi B*, vol. 216, pp. 391–398, Nov. 1999.

[49] L. B. Cen, B. Shen, C. C. Huang, F. J. Xu, Z. X. Qin, G. Y. Zhang, X. S. Chen, and W. Lu, "Influence of polarization-induced electric fields on coherent electron tunneling in AlN/GaN coupled double quantum wells," *J. Appl. Phys.*, vol. 108, no. 11, 113107, 2010.

[50] V. D. Jovanović, Z. Ikonić, D. Indjin, P. Harrison, and R. A. Soref, "Designs for λ=1.55 µm GaN-Based Intersubband Laser Active Region," *Jpn. J. Appl. Phys.*, vol. 43, p. 7444, Nov. 2004.

[51] I. Vurgaftman and J. R. Meyer, "Band parameters for nitrogen-containing semiconductors," *J. Appl. Phys.*, vol. 94, no. 6, pp. 3675–3696, 2003.

[52] C. E. Dreyer, A. Janotti, and C. G. Van de Walle, "Effects of strain on the electron effective mass in gan and aln," *Appl. Phys. Lett.*, vol. 102, no. 14, 142105, 2013.

[53] H. Morkoç, *Nitride Semiconductor Devices: Fundamentals and Applications*. John Wiley & Sons, 2013.

[54] F. Bernardini, V. Fiorentini, and D. Vanderbilt, "Spontaneous polarization and piezoelectric constants of III-v nitrides," *Phys. Rev. B*, vol. 56, pp. 10024–10027, Oct 1997.

[55] M. Sánchez-García, J. Pau, F. Naranjo, A. Jiménez, S. Fernández, J. Ristic, F. Calle, E. Calleja, and E. M. noz, "Plasma-assisted MBE growth of group-III nitrides: from basics to device applications," *Mater. Sci. Eng. B*, vol. 93, no. 1–3, pp. 189–196, 2002.

[56] P. H. Holloway and G. E. McGuire, *Handbook of compound semiconductors: growth, processing, characterization, and devices*. Elsevier, 1996.

[57] H. H. Sun, F. Y. Guo, D. Y. Li, L. Wang, D. B. Wang, and L. C. Zhao, "Intersubband absorption properties of high Al content Al_x $Ga_{1-x}N$/GaN multiple quantum wells grown with different interlayers by metal organic chemical vapor deposition," *Nanoscale Res. Lett.*, vol. 7, no. 1, pp. 1–6, 2012.

[58] D. Hofstetter, J. Di Francesco, D. Martin, N. Grandjean, Y. Kotsar, and E. Monroy, "Si-interdiffusion in heavily doped AlN-GaN-based quantum well intersubband photodetectors," *Appl. Phys. Lett.*, vol. 98, no. 24, 241101, 2011.

[59] M. Lundstrom, *Fundamentals of Carrier Transport*. Modular series on solid state devices, Reading, Wokingham: Addison-Wesley, 1990.

[60] S.-H. Park, Y.-T. Lee, and D. Ahn, "Spontaneous polarization and piezoelectric effects on intraband relaxation time in a wurtzite GaN/AlGaN quantum well," *Appl. Phys. A Mater. Sci. Process.*, vol. 71, pp. 589–592, Nov. 2000.

[61] V. D. Jovanovic, S. Hofling, D. Indjin, N. Vukmirovic, Z. Ikonic, P. Harrison, J. P. Reithmaier, and A. Forchel, "Influence of doping density on electron dynamics in GaAs/AlGaAs quantum cascade lasers," *J. Appl. Phys.*, vol. 99, no. 10, 103106, 2006.

[62] T. Piorek, *Aspects of low-dimensional diluted semimagnetic structures*. PhD thesis, University of Hull, 1996.

[63] H. Sakaki, T. Noda, K. Hirakawa, M. Tanaka, and T. Matsusue, "Interface roughness scattering in GaAs/AlAs quantum wells," *Appl. Phys. Lett.*, vol. 51, no. 23, pp. 1934–1936, 1987.

[64] T. Unuma, M. Yoshita, T. Noda, H. Sakaki, and H. Akiyama, "Intersubband absorption linewidth in GaAs quantum wells due to scattering by interface roughness, phonons, alloy disorder, and impurities," *J. Appl. Phys.*, vol. 93, no. 3, pp. 1586–1597, 2003.

[65] A. Valavanis, Z. Ikonić, and R. W. Kelsall, "Intersubband carrier scattering in *n*- and *p*- Si/SiGe quantum wells with diffuse interfaces," *Phys. Rev. B*, vol. 77, 075312, Feb 2008.

[66] E. Dupont, S. Fathololoumi, Z. R. Wasilewski, G. Aers, S. R. Laframboise, M. Lindskog, S. G. Razavipour, A. Wacker, D. Ban, and H. C. Liu, "A phonon scattering assisted injection and extraction based terahertz quantum cascade laser," *J. Appl. Phys.*, vol. 111, no. 7, 073111, 2012.

[67] J. H. Smet, C. G. Fonstad, and Q. Hu, "Intrawell and interwell intersubband transitions in multiple quantum wells for far-infrared sources," *J. Appl. Phys.*, vol. 79, no. 12, pp. 9305–9320, 1996.

[68] P. F. Maldague, "Many-body corrections to the polarizability of the two-dimensional electron gas," *Surf. Sci.*, vol. 73, pp. 296–302, 1978.

[69] D. Indjin, P. Harrison, R. W. Kelsall, and Z. Ikonić, "Mechanisms of temperature performance degradation in terahertz quantum-cascade lasers," *Appl. Phys. Lett.*, vol. 82, no. 9, pp. 1347–1349, 2003.

[70] P. Harrison, D. Indjin, V. D. Jovanović, A. Mirčetić, Z. Ikonić, R. W. Kelsall, J. McTavish, I. Savić, N. Vukmirović, and V. Milanović, "A physical model of quantum cascade lasers: Application to GaAs, GaN and SiGe devices," *Phys. Status Solidi A*, vol. 202, no. 6, pp. 980–986, 2005.

[71] A. Wacker, M. Lindskog, and D. Winge, "Non-equilibrium green's function model for simulation of quantum cascade laser devices under operating conditions," *IEEE J. Sel. Top. Quantum Electron.*, vol. 19, pp. 1–11, Sept. 2013.

[72] K. Blum, *Density Matrix Theory and Applications*. Physics of Atoms and Molecules, Springer, 1996.

[73] T. V. Dinh, A. Valavanis, L. J. M. Lever, Z. Ikonić, and R. W. Kelsall, "Extended density-matrix model applied to silicon-based terahertz quantum cascade lasers," *Phys. Rev. B*, vol. 85, 235427, June 2012.

[74] G. Beji, Z. Ikonić, C. A. Evans, D. Indjin, and P. Harrison, "Coherent transport description of the dual-wavelength ambipolar terahertz quantum cascade laser," *J. Appl. Phys.*, vol. 109, no. 1, 013111, 2011.

[75] H. Callebaut and Q. Hu, "Importance of coherence for electron transport in terahertz quantum cascade lasers," *J. Appl. Phys.*, vol. 98, no. 10, 104505, 2005.

[76] M. A. Talukder and C. R. Menyuk, "Temperature-dependent coherent carrier transport in quantum cascade lasers," *New J. Phys.*, vol. 13, no. 8, 083027, 2011.

[77] A. Wittmann, Y. Bonetti, J. Faist, E. Gini, and M. Giovannini, "Intersubband linewidths in quantum cascade laser designs," *Appl. Phys. Lett.*, vol. 93, no. 14, 141103, 2008.

[78] C. Jirauschek and P. Lugli, "Monte-carlo-based spectral gain analysis for terahertz quantum cascade lasers," *J. Appl. Phys.*, vol. 105, no. 12, 123102, 2009.

[79] F. Banit, S.-C. Lee, A. Knorr, and A. Wacker, "Self-consistent theory of the gain linewidth for quantum-cascade lasers," *Appl. Phys. Lett.*, vol. 86, no. 4, 041108, 2005.

[80] W. Freeman and G. Karunasiri, "Non-resonant tunneling phonon depopulated GaN based terahertz quantum cascade structures," *Appl. Phys. Lett.*, vol. 102, no. 15, 152111, 2013.

[81] G. Zegrya and V. Perlin, "Intraband absorption of light in quantum wells induced by electron-electron collisions," *Semiconductors*, vol. 32, no. 4, pp. 417–422, 1998.

[82] D. Indjin, P. Harrison, R. W. Kelsall, and Z. Ikonić, "Self-consistent scattering theory of transport and output characteristics of quantum cascade lasers," *J. Appl. Phys.*, vol. 91, no. 11, pp. 9019–9026, 2002.

[83] W. Freeman and G. Karunasiri, "Nonequilibrium electron leakage in terahertz quantum cascade structures," *Phys. Rev. B*, vol. 85, 195326, May 2012.

[84] B. S. Williams, H. Callebaut, S. Kumar, Q. Hu, and J. L. Reno, "3.4-THz quantum cascade laser based on longitudinal-optical-phonon scattering for depopulation," *Appl. Phys. Lett.*, vol. 82, no. 7, pp. 1015–1017, 2003.

[85] Q. Hu, B. S. Williams, S. Kumar, H. Callebaut, S. Kohen, and J. L. Reno, "Resonant-phonon-assisted THz quantum-cascade lasers with metal metal waveguides," *Semicond. Sci. Technol.*, vol. 20, no. 7, p. S228, 2005.

[86] M. Franckié, D. O. Winge, J. Wolf, V. Liverini, E. Dupont, V. Trinité, J. Faist, and A. Wacker, "Impact of interface roughness distributions on the operation of quantum cascade lasers," *Opt. Express*, vol. 23, no. 4, pp. 5201–5212, 2015.

[87] M. Lindskog, J. M. Wolf, V. Trinite, V. Liverini, J. Faist, G. Maisons, M. Carras, R. Aidam, R. Ostendorf, and A. Wacker, "Comparative analysis of quantum cascade laser modeling based on density matrices and non-equilibrium Greens functions," *Appl. Phys. Lett.*, vol. 105, no. 10, 103106, 2014.

[88] Y. Hou, W.-P. Wang, N. Li, W. Lu, and Y. Fu, "Effects of series and parallel resistances on the current-voltage characteristics of small-area air-bridge resonant tunneling diode," *J. Appl. Phys.*, vol. 104, no. 7, 074508, 2008.

[89] C. W. I. Chan, Q. Hu, and J. L. Reno, "Tall-barrier terahertz quantum cascade lasers," *Appl. Phys. Lett.*, vol. 103, no. 15, 151117, 2013.

[90] Y. Bai, N. Bandyopadhyay, S. Tsao, S. Slivken, and M. Razeghi, "Room temperature quantum cascade lasers with 27% wall plug efficiency," *Appl. Phys. Lett.*, vol. 98, no. 18, 181102, 2011.

[91] M. A. Belkin, J. A. Fan, S. Hormoz, F. Capasso, S. P. Khanna, M. Lachab, A. G. Davies, and E. H. Linfield, "Terahertz quantum cascade lasers with copper metal-metal waveguides operating up to 178 K," *Opt. Express*, vol. 16, pp. 3242–3248, Mar. 2008.

[92] S. Kumar, Q. Hu, and J. L. Reno, "186 K operation of terahertz quantum-cascade lasers based on a diagonal design," *Appl. Phys. Lett.*, vol. 94, no. 13, 131105, 2009.

[93] A. Matyas, R. Chashmahcharagh, I. Kovacs, P. Lugli, K. Vijayraghavan, M. A. Belkin, and C. Jirauschek, "Improved terahertz quantum cascade laser with variable height barriers," *J. Appl. Phys.*, vol. 111, no. 10, 103106, 2012.

[94] A. Jiang, A. Matyas, K. Vijayraghavan, C. Jirauschek, Z. R. Wasilewski, and M. A. Belkin, "Experimental investigation of terahertz quantum cascade laser with variable barrier heights," *J. Appl. Phys.*, vol. 115, no. 16, 163103, 2014.

[95] Y. Bai, N. Bandyopadhyay, S. Tsao, E. Selcuk, S. Slivken, and M. Razeghi, "Highly temperature insensitive quantum cascade lasers," *Appl. Phys. Lett.*, vol. 97, no. 25, 251104, 2010.

[96] A. Valavanis, L. Lever, C. A. Evans, Z. Ikonić, and R. W. Kelsall, "Theory and design of quantum cascade lasers in (111) n-type Si/SiGe," *Phys. Rev. B*, vol. 78, 035420, July 2008.

[97] A. Łaszcz, J. Ratajczak, A. Czerwinski, K. Kosiel, J. Kubacka-Traczyk, J. Muszalski, M. Bugajski, and J. Kątcki, "Electron microscopy of GaAs/AlGaAs quantum cascade laser," in *EMC 2008 14th European Microscopy Congress 1–5 September 2008, Aachen, Germany* (S. Richter and A. Schwedt, eds.), pp. 61–62, Springer Berlin Heidelberg, 2008.

[98] A. Mirčetić, D. Indjin, Z. Ikonić, P. Harrison, V. Milanović, and R. W. Kelsall, "Towards automated design of quantum cascade lasers," *J. Appl. Phys.*, vol. 97, no. 8, 084506, 2005.

[99] M. Arafin, N. Islam, S. Roy, and S. Islam, "Performance optimization for terahertz quantum cascade laser at higher temperature using genetic algorithm," *Opt. Quantum. Electron.*, vol. 44, no. 15, pp. 701–715, 2012.

[100] A. Bismuto, R. Terazzi, B. Hinkov, M. Beck, and J. Faist, "Fully automatized quantum cascade laser design by genetic optimization," *Appl. Phys. Lett.*, vol. 101, no. 2, 021103, 2012.

[101] S. Fathololoumi, E. Dupont, Z. R. Wasilewski, C. W. I. Chan, S. G. Razavipour, S. R. Laframboise, S. Huang, Q. Hu, D. Ban, and H. C. Liu, "Effect of oscillator strength and intermediate resonance on the performance of resonant phonon-based terahertz quantum cascade lasers," *J. Appl. Phys.*, vol. 113, no. 11, 113109, 2013.

[102] E. Bellotti, K. Driscoll, T. D. Moustakas, and R. Paiella, "Monte Carlo study of GaN versus GaAs terahertz quantum cascade structures," *Appl. Phys. Lett.*, vol. 92, no. 10, 101112, 2008.

[103] M. Yamanishi, K. Fujita, T. Edamura, and H. Kan, "Indirect pump scheme for quantum cascade lasers: dynamics of electron-transport and very high T_0-values," *Opt. Express*, vol. 16, pp. 20748–20758, Dec. 2008.

[104] H. Yasuda, T. Kubis, P. Vogl, N. Sekine, I. Hosako, and K. Hirakawa, "Nonequilibrium green's function calculation for four-level scheme terahertz quantum cascade lasers," *Appl. Phys. Lett.*, vol. 94, no. 15, 151109, 2009.

[105] Y. Zhang, I. P. Smorchkova, C. R. Elsass, S. Keller, J. P. Ibbetson, S. Denbaars, U. K. Mishra, and J. Singh, "Charge control and mobility in Al-

GaN/GaN transistors: Experimental and theoretical studies," *J. Appl. Phys.*, vol. 87, no. 11, pp. 7981–7987, 2000.

[106] Y. Cao and D. Jena, "High-mobility window for two-dimensional electron gases at ultrathin AlN/GaN heterojunctions," *Appl. Phys. Lett.*, vol. 90, no. 18, 182112, 2007.

[107] M. I. Amanti, G. Scalari, R. Terazzi, M. Fischer, M. Beck, J. Faist, A. Rudra, P. Gallo, and E. Kapon, "Bound-to-continuum terahertz quantum cascade laser with a single-quantum-well phonon extraction/injection stage," *New J. Phys.*, vol. 11, no. 12, 125022, 2009.

[108] M. J. Rudd, "A laser Doppler velocimeter employing the laser as a mixer-oscillator," *J. Phys. E: Sci. Instrum.*, vol. 1, no. 7, p. 723, 1968.

[109] S. Donati, "Laser interferometry by induced modulation of cavity field," *J. Appl. Phys.*, vol. 49, no. 2, pp. 495–497, 1978.

[110] S. Shinohara, A. Mochizuki, H. Yoshida, and M. Sumi, "Laser Doppler velocimeter using the self-mixing effect of a semiconductor laser diode," *Appl. Opt.*, vol. 25, pp. 1417–1419, May 1986.

[111] R. Lang and K. Kobayashi, "External optical feedback effects on semiconductor injection laser properties," *IEEE J. Quant. Electron.*, vol. 16, no. 3, pp. 347–355, 1980.

[112] R. P. Green, J.-H. Xu, L. Mahler, A. Tredicucci, F. Beltram, G. Giuliani, H. E. Beere, and D. A. Ritchie, "Linewidth enhancement factor of terahertz quantum cascade lasers," *Appl. Phys. Lett.*, vol. 92, no. 7, 071106, 2008.

[113] A. Valavanis, P. Dean, Y. L. Lim, R. Alhathlool, M. Nikolic, R. Kliese, S. Khanna, D. Indjin, S. Wilson, A. Rakić, E. Linfield, and G. Davies, "Self-

mixing interferometry with terahertz quantum cascade lasers," *IEEE Sensors J.*, vol. 13, pp. 37–43, Jan. 2013.

[114] Y. L. Lim, T. Taimre, K. Bertling, P. Dean, D. Indjin, A. Valavanis, S. P. Khanna, M. Lachab, H. Schaider, T. W. Prow, H. P. Soyer, S. J. Wilson, E. H. Linfield, A. G. Davies, and A. D. Rakić, "High-contrast coherent terahertz imaging of porcine tissue via swept-frequency feedback interferometry," *Biomed. Opt. Express*, vol. 5, pp. 3981–3989, Nov. 2014.

[115] P. Dean, A. Valavanis, J. Keeley, K. Bertling, Y. Leng Lim, R. Alhathlool, S. Chowdhury, T. Taimre, L. H. Li, D. Indjin, S. J. Wilson, A. D. Rakić, E. H. Linfield, and A. Giles Davies, "Coherent three-dimensional terahertz imaging through self-mixing in a quantum cascade laser," *Appl. Phys. Lett.*, vol. 103, no. 18, 181112, 2013.

[116] S. Donati, "Responsivity and noise of self-mixing photodetection schemes," *IEEE J. Quant. Electron.*, vol. 47, no. 11, pp. 1428–1433, 2011.

[117] G. Agnew, A. Grier, T. Taimre, Y. L. Lim, M. Nikolić, A. Valavanis, J. Cooper, P. Dean, S. P. Khanna, M. Lachab, E. H. Linfield, A. G. Davies, P. Harrison, Z. Ikonić, D. Indjin, and A. D. Rakić, "Efficient prediction of terahertz quantum cascade laser dynamics from steady-state simulations," *Appl. Phys. Lett.*, vol. 106, no. 16, 161105, 2015.

[118] A. Hamadou, S. Lamari, and J.-L. Thobel, "Dynamic modeling of a mid-infrared quantum cascade laser," *J. Appl. Phys.*, vol. 105, no. 9, 093116, 2009.

[119] C. Gmachl, H. M. Ng, and A. Y. Cho, "Intersubband absorption in degenerately doped coupled double quantum wells," *Appl. Phys. Lett.*, vol. 79, no. 11, p. 1590, 2001.

[120] J. D. Heber, C. Gmachl, H. M. Ng, and A. Y. Cho, "Comparative study of ultrafast intersubband electron scattering times at wavelength in GaN/AlGaN heterostructures," *Appl. Phys. Lett.*, vol. 81, no. 7, pp. 1237–1239, 2002.

[121] N. Suzuki and N. Iizuka, "Electron scattering rates in AlGaN/GaN quantum wells for 1.55 µm inter-subband transition," *Jpn. J. Appl. Phys.*, vol. 37, no. Part 2, No. 4A, pp. L369–L371, 1998.

[122] V. D. Jovanović, D. Indjin, Z. Ikonić, V. Milanović, and J. Radovanović, "Design of GaN/AlGaN quantum wells for maximal intersubband absorption in 1.3-1.55 µm wavelength range," *Solid State Commun.*, vol. 121, no. 11, pp. 619–624, 2002.

[123] M. S. Miao, A. Janotti, and C. G. Van de Walle, "Reconstructions and origin of surface states on AlN polar and nonpolar surfaces," *Phys. Rev. B*, vol. 80, 155319, Oct. 2009.

[124] S. Birner, T. Zibold, T. Andlauer, T. Kubis, M. Sabathil, A. Trellakis, and P. Vogl, "nextnano: General purpose 3-D simulations," *IEEE Trans. Electron Dev.*, vol. 54, pp. 2137–2142, Sept. 2007.

[125] H. Machhadani, Y. Kotsar, S. Sakr, M. Tchernycheva, R. Colombelli, J. Mangeney, E. Bellet-Amalric, E. Sarigiannidou, E. Monroy, and F. H. Julien, "Terahertz intersubband absorption in GaN/AlGaN step quantum wells," *Appl. Phys. Lett.*, vol. 97, no. 19, 191101, 2010.

[126] M. Beeler, C. Bougerol, E. Bellet-Amalric, and E. Monroy, "Terahertz absorbing AlGaN/GaN multi-quantum-wells: Demonstration of a robust 4-layer design," *Appl. Phys. Lett.*, vol. 103, no. 9, 091108, 2013.

[127] C. Edmunds, J. Shao, M. Shirazi-HD, M. J. Manfra, and O. Malis, "Terahertz

intersubband absorption in non-polar m-plane AlGaN/GaN quantum wells," *Appl. Phys. Lett.*, vol. 105, no. 2, 021109, 2014.

[128] R. Tsu and L. Esaki, "Tunneling in a finite superlattice," *Appl. Phys. Lett.*, vol. 22, no. 11, pp. 562–564, 1973.

[129] R. C. Bowen, G. Klimeck, R. K. Lake, W. R. Frensley, and T. Moise, "Quantitative simulation of a resonant tunneling diode," *J. Appl. Phys.*, vol. 81, no. 7, pp. 3207–3213, 1997.

[130] B. R. Bennett, R. Magno, J. B. Boos, W. Kruppa, and M. G. Ancona, "Antimonide-based compound semiconductors for electronic devices: A review," *Solid-State Electronics*, vol. 49, no. 12, pp. 1875–1895, 2005.

[131] A. Kikuchi, R. Bannai, K. Kishino, C.-M. Lee, and J.-I. Chyi, "AlN/GaN double-barrier resonant tunneling diodes grown by rf-plasma-assisted molecular-beam epitaxy," *Appl. Phys. Lett.*, vol. 81, no. 9, pp. 1729–1731, 2002.

[132] A. E. Belyaev, C. T. Foxon, S. V. Novikov, O. Makarovsky, L. Eaves, M. J. Kappers, and C. J. Humphreys, "Comment on AlN/GaN double-barrier resonant tunneling diodes grown by rf-plasma-assisted molecular-beam epitaxy [Appl. Phys. Lett. 81, 1729 (2002)]," *Appl. Phys. Lett.*, vol. 83, no. 17, pp. 3626–3627, 2003.

[133] L. Yang, H. He, W. Mao, and Y. Hao, "Quantitative analysis of the trapping effect on terahertz AlGaN/GaN resonant tunneling diode," *Appl. Phys. Lett.*, vol. 99, no. 15, 153501, 2011.

[134] E. Baumann, F. R. Giorgetta, D. Hofstetter, H. Wu, W. J. Schaff, L. F. Eastman, and L. Kirste, "Tunneling effects and intersubband absorption in AlN/GaN superlattices," *Appl. Phys. Lett.*, vol. 86, no. 3, 032110, 2005.

[135] Z. Vashaei, C. Bayram, and M. Razeghi, "Demonstration of negative differential resistance in GaN/AlN resonant tunneling diodes at room temperature," *J. Appl. Phys.*, vol. 107, no. 8, 083505, 2010.

[136] C. Bayram, Z. Vashaei, and M. Razeghi, "Reliability in room-temperature negative differential resistance characteristics of low-aluminum content AlGaN/GaN double-barrier resonant tunneling diodes," *Appl. Phys. Lett.*, vol. 97, no. 18, 181109, 2010.

[137] M. Boucherit, A. Soltani, E. Monroy, M. Rousseau, D. Deresmes, M. Berthe, C. Durand, and J.-C. De Jaeger, "Investigation of the negative differential resistance reproducibility in AlN/GaN double-barrier resonant tunnelling diodes," *Appl. Phys. Lett.*, vol. 99, no. 18, 182109, 2011.

[138] Y. Shao, S. D. Carnevale, A. T. M. G. Sarwar, R. C. Myers, and W. Lu, "Single nanowire AlN/GaN double barrier resonant tunneling diodes with bipolar tunneling at room and cryogenic temperatures," *J. Vac. Sci. Technol., B: Microelectron. Nanometer Struct.*, vol. 31, no. 6, 2013.

[139] D. Li, J. Shao, L. Tang, C. Edmunds, G. Gardner, M. J. Manfra, and O. Malis, "Temperature-dependence of negative differential resistance in GaN/AlGaN resonant tunneling structures," *Semicond. Sci. Technol.*, vol. 28, no. 7, p. 074024, 2013.

[140] F. F. Sudradjat, W. Zhang, K. Driscoll, Y. Liao, A. Bhattacharyya, C. Thomidis, L. Zhou, D. J. Smith, T. D. Moustakas, and R. Paiella, "Sequential tunneling transport in GaN/AlGaN quantum cascade structures," *Phys. Status. Solidi C*, vol. 9, no. 3-4, pp. 588–591, 2012.

[141] S. Sakr, Y. Kotsar, M. Tchernycheva, E. Warde, N. Isac, E. Monroy, and F. H.

Julien, "Resonant tunneling transport in a GaN/AlN multiple-quantum-well structure," *Appl. Phys. Express*, vol. 5, no. 5, 052203, 2012.

[142] F. Sudradjat, W. Zhang, K. Driscoll, Y. Liao, A. Bhattacharyya, C. Thomidis, L. Zhou, D. J. Smith, T. D. Moustakas, and R. Paiella, "Sequential tunneling transport characteristics of GaN/AlGaN coupled-quantum-well structures," *J. Appl. Phys.*, vol. 108, no. 10, 103704, 2010.

[143] B. A. Biegel and J. D. Plummer, "Comparison of self-consistency iteration options for the wigner function method of quantum device simulation," *Phys. Rev. B*, vol. 54, pp. 8070–8082, Sept. 1996.

[144] F. Rossi, P. Poli, and C. Jacoboni, "Weighted Monte Carlo approach to electron transport in semiconductors," *Semicond. Sci. Technol.*, vol. 7, no. 8, p. 1017, 1992.

[145] K. L. Jensen and F. A. Buot, "Numerical simulation of intrinsic bistability and high-frequency current oscillations in resonant tunneling structures," *Phys. Rev. Lett.*, vol. 66, pp. 1078–1081, Feb. 1991.

[146] S. Sakr, E. Warde, M. Tchernycheva, and F. H. Julien, "Ballistic transport in GaN/AlGaN resonant tunneling diodes," *J. Appl. Phys.*, vol. 109, no. 2, 023717, 2011.

[147] M. Boucherit, A. Soltani, M. Rousseau, J.-L. Farvacque, and J.-C. DeJaeger, "Effect of heterostructure design on current-voltage characteristics in $Al_xGa_{1-x}N$/GaN double-barriers resonant tunneling diode," *J. Appl. Phys.*, vol. 112, no. 11, 114305, 2012.

[148] A. Yariv, C. Lindsey, and U. Sivan, "Approximate analytic solution for electronic wave functions and energies in coupled quantum wells," *J. Appl. Phys.*, vol. 58, no. 9, pp. 3669–3672, 1985.

[149] C. Sanderson, "Armadillo: An open source C++ linear algebra library for fast prototyping and computationally intensive experiments," tech. rep., NICTA, Australia, Oct. 2010.

[150] A. Fediai and V. Moskaliuk, "Modeling of resonant-tunneling diode with uniform and graded emitter," in *Electronics and Nanotechnology (ELNANO), 2013 IEEE XXXIII International Scientific Conference, Ukraine*, pp. 107–111, Apr. 2013.

[151] I. Abramov, N. Kolomeitseva, and I. Romanova, "Combined two-band models of resonant tunneling diodes," *Russ. Microlectron.*, vol. 41, no. 5, pp. 314–323, 2012.

[152] P. Zhao, H. L. Cui, D. Woolard, K. L. Jensen, and F. A. Buot, "Simulation of resonant tunneling structures: Origin of the I–V hysteresis and plateau-like structure," *J. Appl. Phys.*, vol. 87, no. 3, pp. 1337–1349, 2000.

[153] A. Sakurai and Y. Tanimura, "An Approach to Quantum Transport Based on Reduced Hierarchy Equations of Motion: Application to a Resonant Tunneling Diode," *J. Phys. Soc. Jpn.*, vol. 82, 033707, Mar. 2013.

[154] J. B. Khurgin, Y. Dikmelik, P. Q. Liu, A. J. Hoffman, M. D. Escarra, K. J. Franz, and C. F. Gmachl, "Role of interface roughness in the transport and lasing characteristics of quantum-cascade lasers," *Appl. Phys. Lett.*, vol. 94, no. 9, 091101, 2009.

[155] S. J. Pearton, J. C. Zolper, R. J. Shul, and F. Ren, "GaN: Processing, defects, and devices," *J. Appl. Phys.*, vol. 86, no. 1, pp. 1–78, 1999.

[156] S. Sakr, E. Warde, M. Tchernycheva, L. Rigutti, N. Isac, and F. H. Julien, "Origin of the electrical instabilities in GaN/AlGaN double-barrier structure," *Appl. Phys. Lett.*, vol. 99, no. 14, 142103, 2011.

[157] O. Mitrofanov and M. Manfra, "Poole-Frenkel electron emission from the traps in AlGaN/GaN transistors," *J. Appl. Phys.*, vol. 95, no. 11, pp. 6414–6419, 2004.

[158] A. M. Katzenmeyer, F. Léonard, A. A. Talin, P.-S. Wong, and D. L. Huffaker, "Poole–Frenkel effect and phonon-assisted tunneling in GaAs nanowires," *Nano Lett.*, vol. 10, no. 12, pp. 4935–4938, 2010.

[159] K. Berland, T. G. Andersson, and P. Hyldgaard, "Polarization-balanced design of heterostructures: Application to AlN/GaN double-barrier structures," *Phys. Rev. B*, vol. 84, 245313, Dec. 2011.

[160] V. D. Jovanović, Z. Ikonić, D. Indjin, P. Harrison, V. Milanović, and R. Soref, "Designing strain-balanced GaN/AlGaN quantum well structures: Application to intersubband devices at 1.3 and 1.55 µm wavelengths," *J. Appl. Phys.*, vol. 93, pp. 3194–3197, Mar. 2003.

[161] R. Terazzi, T. Gresch, A. Wittmann, and J. Faist, "Sequential resonant tunneling in quantum cascade lasers," *Phys. Rev. B*, vol. 78, 155328, Oct. 2008.

[162] C. R. Menyuk and M. A. Talukder, "Self-induced transparency modelocking of quantum cascade lasers," *Phys. Rev. Lett.*, vol. 102, p. 023903, Jan. 2009.